# COMPUTATIONAL INVESTIGATION OF NON-ISOTHERMAL LID-DRIVEN FLOW IN ARC-SHAPE CAVITIES

by

Ali Reza Rezaei Adli

B.S., Mechanical Engineering, Boğaziçi University, 2005

Submitted to the Institute for Graduate Studies in
Science and Engineering in partial fulfillment of
the requirements for the degree of
Master of Science

Graduate Program in Mechanical Engineering

Boğaziçi University

2008

# ACKNOWLEDGEMENTS

First of all, I am deeply and forever grateful to my family for their support and encouragement. Particularly, I am most indebted to my mother for her love and support throughout my entire life. Without her sacrifices it would not have been possible for me to write this thesis.

I would like to express my gratitude to Dr. Kunt Atalık. His constant encouragement, support, and suggestions made this work successful. I am indebted to my jury members Dr. Hasan Bedir and Dr. Osman Börekçi for their time and effort in reviewing this work. Sincere thanks also to Dr. Hasan Bedir for providing the computer facilities.

# ABSTRACT


## COMPUTATIONAL INVESTIGATION OF NON-ISOTHERMAL LID-DRIVEN FLOW IN ARC-SHAPE CAVITIES

This thesis is concerned with the numerical analysis of laminar unsteady flow and heat transfer in lid-driven arc-shape cavities with different aspect ratios for which the top lid, maintained at lower temperature, is driven at a uniform speed and the bottom stationary wall is maintained at higher temperature. The buoyancy force resulted by the temperature difference across the wall and the lid of the cavity is controlled by Richardson number, whereas Reynolds number represents the strength of inertia generated by the shear force along the lid. In order to reveal the effects of temperature difference and lid motion on flow pattern and thermal distribution, wide ranges of Reynolds and Richardson numbers are selected and the results are plotted in terms of streamlines and isotherms. Governing equations are discretized based on finite difference technique and these equations are applied to computational grids generated by body fitted coordinate transformation method. Aspect ratio effects on flow and thermal behavior are also investigated. Moreover, heat transfer performance and shear stress are demonstrated in terms of local and average Nusselt numbers and local friction factor, respectively.

# ÖZET

## KAPAK TAHRİKLİ YAY ŞEKİLLİ OYUKLARDA İZOTERMAL OLMAYAN AKIŞIN SAYISAL İNCELEMESİ

Bu tez, kapak tahrikli yay geometrili oyuklarda laminer ve durağan olmayan akış ve ısı transferinin sayısal analiziyle ilgili olup, düşük ısıda tutulan üst kapak sabit bir hızla soldan sağa doğru hareket ettirilmekte ve alt duvar yüksek sıcaklıkta tutulmaktadır. Kapak ve duvar arasındaki ısı farkından kaynaklanan kaldırma kuvveti Richardson sayısıyla kontrol edilmektedir. Reynolds sayısı ise kayma kuvvetinden kaynaklanan eylemsizlik şiddetini ifade etmektedir. Isı farkının ve kapak hareketinin akış yapısı ve ısı dağılımına etkisini göstermek için Reynolds ve Richardson sayıları geniş bir çerçevede seçilmiş ve sonuçlar akış çizgileri ve eşsıcaklık eğrileriyle anlatılmıştır. Sistem denklemleri sonlu farklar tekniğiyle ayrıklaştırılmış ve bu denklemler şekle oturan koordinat transformasyonuyla yaratılan sayısal ağlara uygulanmıştır. Yaya bakan açı oranının akış alanı ve ısı davranışı üzerindeki etkileri araştırılmıştır. Ayrıca, ısı transfer performansı ve kayma gerilmesi, sırasıyla, Nusselt sayısı ve lokal sürtünme faktörü cinsinden gösterilmiş ve hesaplanmıştır.

## TABLE OF CONTENTS

# LIST OF FIGURES

# LIST OF TABLES

# LIST OF SYMBOLS / ABBREVIATIONS

| | |
|---|---|
| $u$ | Velocity of the fluid in horizontal direction |
| $\upsilon$ | Velocity of the fluid in vertical direction |
| $T$ | Temperature |
| $P$ | Pressure |
| $T_H$ | High temperature |
| $T_L$ | Low temperature |
| $L$ | Characteristic length |
| $X$ | Dimensionless horizontal coordinate |
| $Y$ | Dimensionless vertical coordinate |
| $x$ | Horizontal Cartesian coordinate |
| $y$ | Vertical Cartesian coordinate |
| $U$ | Dimensionless horizontal velocity component |
| $V$ | Dimensionless vertical velocity component |
| $U_L$ | Velocity of moving lid |
| $t$ | Time |
| r | Radius |
| $J$ | Jacobian of transformation |
| $g$ | Acceleration due to gravity |
| $\vec{n}$ | Outward normal vector |
| $\vec{s}$ | Tangential vector |
| $k$ | Thermal conductivity |
| $h_x$ | Local convective heat transfer coefficient |
| $f_x$ | Local friction coefficient |
| $w$ | Overrelaxation parameter |
| Re | Reynolds number |
| Pr | Prandtl number |
| $Ri$ | Richardson number |
| $Ra$ | Rayleigh number |

| | |
|---|---|
| $Gr$ | Grashof number |
| $Nu_x$ | Local Nusselt number |
| $Nu$ | Average Nusselt number |
| | |
| $\mu$ | Dynamic viscosity of fluid |
| $\rho$ | Fluid density |
| $\beta$ | Coefficient of thermal expansion |
| $\Phi$ | Viscous dissipation function |
| $\alpha$ | Thermal diffusivity of fluid |
| $\nu$ | Kinematic viscosity of fluid |
| $\varphi$ | Stream function |
| $\omega$ | Vorticity |
| $\tau$ | Dimensionless time |
| $\eta$ | Vertical Curvilinear coordinate |
| $\xi$ | Horizontal Curvilinear coordinate |
| $\alpha, \beta, \gamma$ | Coordinate transformation coefficients |
| $\theta$ | Dimensionless temperature |
| $\Omega$ | Dimensionless vorticity |
| $\psi$ | Dimensionless stream function |
| $\rho_{SOR}$ | Spectral radius of SOR |
| $\rho_{Jacobi}$ | Spectral radius of Jacobi |
| $\Pi$ | Residual |
| $\sigma_x$ | Local shear stress |
| | |
| SOR | Successive over relaxation |
| REN | Relative Error Norm |

# 1. INTRODUCTION

Inertia and buoyancy induced flow inside enclosures have been investigated in the past due to its extensive use in industrial applications and in engineering devices like lubrication systems [1-3], solar collectors [5], evaporators [6] and flow channels [4]. Meanwhile, currents due to mixed convection in lakes are the examples for occurrence of this event in nature. These physical phenomena have been idealized in the past mostly by the square geometry with a driven or stationary lid. Even this idealization was complex enough to numerically investigate the problem, further studies showed that the real cases actually are not pure square cavities and the temperature is not unique through the cavity. That is why researchers realized the necessity of new implementations. Figure (1.1) shows an example of lid-driven cavity flow inside a lubrication device.

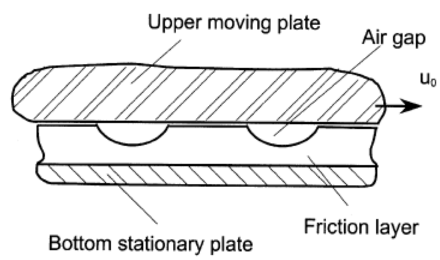


Figure 1.1. Physical model represented by an air-gap lubrication device [19]

First investigations were the experimental studies related with the inertia effects on flow behavior of the fluid in square or rectangular enclosures. In some other investigations researchers have preferred to study the simplest and most classical case of square cavity problem numerically in which the upper wall is moving with a steady velocity and other walls are stationary, for the validation of their computational schemes. The traditional lid-driven cavity flow problem has been the topic of interest since the time in which the fluid and thermal problems have been solved and lead by the computational approach and this goes back to the pioneering work of Ghia et al [8]. Ghia et al have produced one of the benchmark data. They have studied high Reynolds number solution for incompressible flow using the vorticity-stream function formulation of the two-dimensional Navier-Stokes equations and then they have validated their scheme on a lid driven square cavity.

Theodossiou and Sousa [7] have developed an efficient algorithm for an incompressible flow in which they have chosen square lid-driven cavity flow as the test case for the Reynolds numbers ranging from 100 to 1000. The results were in good agreement when compared with the previous works.

The flow in lid driven enclosures keeps its importance as one of the interesting research problems for which many aspects are yet to be explored in more detail. In literature review section (1.1) some of the significant experimental and numerical studies on cavity flow are provided comprehensively.

## 1.1. Literature Survey

### 1.1.1. Experimental Studies

Experimental studies provide the range of data to compare the computational results and to develop the numerical schemes beyond the previously generated classical techniques. Heat transfer due to laminar free convection in vertical slots or vertical walls of an enclosure has been investigated extensively in sixties. For example, the article published by Eckert et al [12] has focused on the measurement of the flow pattern and thermal field for the rectangular cavity with temperature differences across the side walls. For large Grashof numbers and small aspect ratios, thermal boundary layers were observed along the surface of the enclosure where the major part of the heat transfer took place. Temperature at the center was observed to be uniform in the horizontal direction. They have also verified the average heat transfer data. A similar study has been conducted by Elder [13] on laminar free convection in vertical slots with different aspect ratios where the heat transfer took place mostly by conduction. Moreover, the resulting heat transfer has caused the formation of weak circulation. According to Elder, large temperature gradients near walls and uniform vertical temperature gradients in interior parts were generated when $10^3<$ Rayleigh number $<10^5$. In addition, in the interior regions of primary vortex secondary flow was observed when Rayleigh number got closer to $10^5$.

In 1993 Mohammad and Viskanta [15] have performed the experimental investigation to visualize the effects of buoyancy and inertia forces inside the shallow rectangular enclosures. Ethylene Glycol and water have been chosen as the working fluids for the Reynolds number in the range of 170 to 2500. Using liquid crystal technique and aluminum particles the flow and thermal fields have been visualized. They observed that when the Richardson number approached unity the flow field became more complex.

Prasad and Koseff [14] have reported some experimentally obtained data for convection dominated flows. Liquid crystal technique and heat flux measurements have been performed by Prasad and Koseff under different flow and thermal conditions. They found that the buoyancy effect was important when the Richardson number approached unity and it became dominant when the Richardson number was larger than unity. Their report contains the evidence that shows the effect of the Richardson number is not as stronger as the effects of the Reynolds number and the aspect ratio in cavity flow.

Semi-circular, rectangular and square industrial machined or molded cylindrical cavity shapes were studied and compared in the time domain by Migeon and Texier [9], [10]. They gave particular attention to the vorticity propagation and primary and secondary eddy formations. In this unsteady, experimental study they focused mainly on influence of the cavity shape on the initial phase of the flow establishment. They studied the cavity which was translated downward along a vertical lid. It was recorded that during the first time stages the cavity geometry had a significant effect on flow structure development. Meanwhile, it was observed that among three different cases the semi-circular results were more homogenous with no secondary eddies. Also, another investigation was performed by the same researchers three years later which considered three dimensional effects in square and rectangular cavities. Existence of end wall effects resulted in end wall vortices and for the first time in the investigation of lid driven cavities, corner vortices were detected experimentally.

Until the beginning of the last decade only the cavity with a rectangular geometry has been studied thoroughly and a complete understanding of the flow and heat transfer mechanism in a complex-shape cavity was relatively lacking. Between 1999 and 2006 Chen and Cheng [18-22] have focused on numerical and experimental studies of flow and thermal behaviors inside arc-shape enclosures. In some of these studies, experimental investigations along with the numerical methods were performed. Finally, the comparison between the numerical and the experimental data was made for validation. They have investigated flow patterns, thermal effects, shear stresses and heat transfer performances for a wide range of Reynolds and Grashof numbers which are represented in section (1.1.2.2) in detail.

### 1.1.2. Computational Studies

#### 1.1.2.1. Computational Studies in Plane Geometries

The change in flow and heat transfer parameters have been investigated by numerical studies of Vahl Davis et al [23-25] for laminar free convection in rectangular enclosures where vertical side walls were maintained at different temperatures. A thin boundary layer was observed near the walls when Rayleigh number increased and strong vorticity generated near the walls was able to maintain the weak return motion at the outer part of the boundary layer. Reverse motion was also observed near the center of enclosure. They have found that temperature profile was linear at Rayleigh number below $10^3$ and heat transfer within the cavity mainly occurred due to conduction. Their series of studies have provided the benchmark data for future researches on side heated cavity.

Mixed convection in cavities which is the combination of free convection due to the buoyancy force generated by the hot bottom wall and forced convection resulted by the shear force due to the moving top lid has been reported by some researchers during the last decades. In 1992, Moallemi and Jang [26] have numerically investigated the mixed convection phenomenon in a square cavity. Numerical simulations have been performed for two dimensional laminar flow regime in which the Reynolds number ranged from 100 to 2200 and Prandtl numbers varied from 0.01 till 50. Different Grashof numbers also have been used in order to observe the buoyancy effects within the cavity. They have discretized the governing equations by the control volume approach and they have used non-uniform grids near the cavity walls. Moallemi's results have shown that the effects of Prandtl number for the fixed Grashof and Reynolds numbers are more noticeable at higher values.

Luo and Yang [27] have presented a numerical method to calculate flow and thermal fields in a two sided lid-driven cavity with a fixed aspect ratio of 1.96. Both the isothermal and non-isothermal cases were studied. For the non-isothermal study, the hot bottom lid was considered as moving from right to left whereas the colder top lid was assumed moving in the opposite direction, from left to right. Flow patterns were demonstrated by streamlines.

Khanafer and his research group [11] have numerically studied a mechanical sliding lid which was set to oscillate horizontally in a sinusoidal fashion. The natural convective effect was sustained by keeping the bottom and top walls at the higher and lower temperatures, respectively. They have investigated the effects of Reynolds and Grashof numbers along with the lid frequency by fixing two parameters at a time.

#### 1.1.2.2. Computational Studies in Curved Geometries

Most of the previous studies on cavity flow were restricted to the analysis of fluid motion and heat transfer phenomenon in rectangular cavities. For problems concerning the fluid motion and heat transfer inside an enclosure of irregular shape, the cavity was usually simplified to be a rectangular one, which, undoubtedly results in incorrect demonstration and evaluation of the data.

Arc shape cavity flow investigation was carried out for the first time in 1999 by the article published by Chang and Cheng [17]. Following this study, a series of numerical and experimentally supported investigations were published by Cheng and Chen. In all of the studies the main concentration was on the buoyant and inertial effects exerted on the fluid. Fluid properties were assumed to be constant with the exception of the variation of density in the buoyancy term in momentum equation. The first of these studies [17] was concerned with the 1/3 aspect ratio lid driven cavity flow which was heated by the lid and cooled by the stationary arc shape wall. Flow in this study was considered to be steady. In this article, Chang and Cheng have studied various Richardson numbers and Reynolds numbers along with different inclination angles. In the later stages of the same study, they have assumed the flow to be unsteady to determine the periodic cases, if they exist. They have found a periodic pattern when Reynolds and Richardson numbers are both 100 and while the hotter lid was placed at the bottom of the cavity in which the inclination angle $(\delta)$ was equal to $\pi$.

In another study, Chen and Cheng [18] have worked on the same cavity shape with the same aspect ratio. However in this case, they have assumed the lid as stationary and they have changed the cooling and heating directions of the cavity, such that, unlike the investigation of Cheng and Chang [17], the cavity was heated by the wall and cooled by the lid. Inclination angle was analyzed in detail. Also, they developed an experimental system to validate the numerically obtained data. The range of Grashof number considered in their investigation was up to $10^7$ and the inclination angle was varied from 0 to $\pi$. The flow was considered as steady; therefore the periodic flow was not investigated. Various inclination angles were considered and they visualized the effects of Grashof and Reynolds numbers on flow and thermal patterns. Their results revealed that only when Grashof number was higher than $10^5$ the increase in natural convection became appreciable and also the strength of the vortex was found to be strongly dependent on the angle of inclination. Moreover, they have found a close agreement between numerical and experimental results.

In their next study, Chen and Cheng [19] have tried to find the periodic flow patterns generated by the buoyancy force for a cavity oriented horizontally. Therefore, the inclination effect was no longer investigated. Reynolds and Grashof numbers applied in this study were in the range from 100 to 2000 and from 0 to $10^7$, respectively. They found the periodic flow pattern at Reynolds numbers of 100, 200 and 500, for Richardson numbers within the ranges $30 \le Ri \le 100$, $12.5 \le Ri \le 50$ and $20 \le Ri \le 40$, respectively. According to their results, when the Reynolds number and the Richardson number are set within a certain regime, the flow pattern and the thermal field values are repeated continuously at the same frequency, however outside of this periodic regime the flow and thermal fields eventually approach a steady state condition. Once more in 2005, Chen and Cheng [21] have continued their periodic pattern investigation. This time they investigated aspect ratios of 1/2, 1/3 and 1/4 and different geometries, namely triangular, circular and rectangular. For all cases considered, the Reynolds number and the Richardson number were fixed at 100 and 50, respectively. In a rectangular cavity, for the specified Reynolds and Richardson numbers the periodic phenomenon was only obtained at 1/4 aspect ratio while for the circular case periodic patterns were observed at 1/3 and 1/4 aspect ratios and for the triangular one it was noticed at 1/3 aspect ratio. In their next article in 2004, Chen and Cheng [20] have repeated the numerical and experimental investigation of buoyancy and inertia induced flow for various Reynolds and Richardson numbers. This research contained some of the results obtained in previous studies and did not include newer geometries or aspect ratios.

The latest article represented by Cheng and Chen [22] included the cavities of small aspect ratios, but unlike the previous cases, thermal effects were considered without including the buoyant force in the governing flow equations. They have looked for strongest vortex flow among the triangular, circular and rectangular cavities of small aspect ratios. The results revealed that for the fixed Reynolds and Prandtl number, the rectangular cavity produces the strongest vortex flow, while the triangular one generates the weakest.

## 1.2. Statement of the Problem

Flow inside the arc shape cavity is induced mainly by the shear force due to the upper moving lid and it is induced also by the buoyancy force generated by thermal difference across the bottom stationary wall and the top moving lid. The cavity is enclosed at the top by the lid that moves across the enclosure from left to right with a constant speed. The bottom wall is considered as rigid and stationary. The end wall effects are ignored. Therefore, flow and thermal effects are analyzed independent of the orthogonal direction. The bottom stationary wall and the moving lid result in impermeable, no-slip boundary conditions. The top and the bottom surfaces are maintained at constant temperatures $T_L$ and $T_H$, respectively. The fluid is considered to be incompressible and the flow is taken to be laminar and unsteady. Fluid properties are assumed constant except for the change in density in the buoyancy force term of the momentum equation in vertical direction, which is represented with the Boussinesq approximation.

The effects of fluid inertia resulted by the shear force due to lid motion, and the buoyancy generated by the temperature difference between the cold top moving lid and the hot bottom stationary wall is investigated in detail in terms of Reynolds and Richardson numbers, respectively. Aspect ratio is also investigated to include the impact of geometry on fluid flow and temperature distribution within the cavity. Flow and heat transfer are simulated in terms of streamlines and isotherms, respectively. Meanwhile, local Nusselt number and local friction factor along the lid surface are studied for various values of Reynolds and Richardson numbers.

Fluid flow, heat transfer and diffusivity in an arc shape cavity as a result of mixed convection is controlled by the main non-dimensional parameters; Reynolds number (Re), Richardson number (Ri) and Prandtl number (Pr). Inertia effect is directed by the change in Reynolds number and Richardson number introduces the effect of buoyancy force. Aspect ratio is another vital geometrical consideration that together with flow and thermal parameters affects the results. It differentiates the flow regime and thermal field for the same main shape. Large aspect ratio means that flow occurs in a deep cavity, and a small one indicates fluid flow in a shallow cavity.

In this thesis, the effects of aspect ratio together with the inertia and the buoyancy forces are investigated in detail. Different values for each parameter are selected thoroughly. By fixing the parameters one at a time, their contributions to the flow and heat patterns are studied. Reynolds number within the range of 200 to 1500 and Richardson numbers from 0.01 to 100 are examined together with the aspect ratios of 1/2 and 2/3. Prandtl number is assigned to the fixed value, 0.71. Flow pattern is represented in the form of streamlines and heat convection is displayed as isotherms.

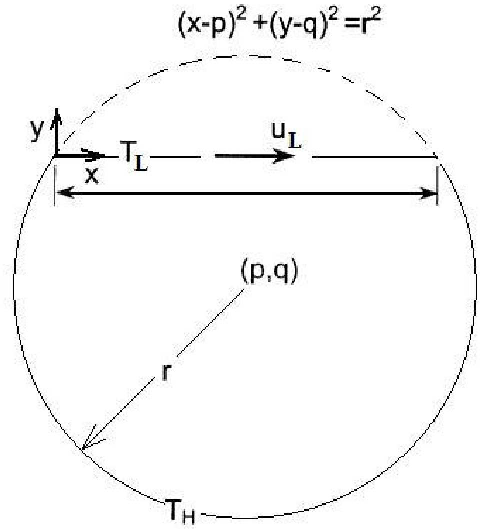


Figure 1.2. Physical configuration of the cavity [19]

The arc profile of the enclosure which is represented in figure (1.2) is expressed by,

$$(x-p)^2 + (y-q)^2 = r^2, \tag{1.1}$$

where the equation (1.1) denotes a circle of radius r with a center located at point $(p,q)$. $x$ and $y$ define the horizontal and vertical directions in Cartesian coordinates and $L$ represents the width of the moving lid. In this thesis two aspect ratios $1/2$ and $2/3$ are considered. For $1/2$ aspect ratio geometry, $p/r$, $q/r$ and $r/L$ are fixed at 1, 1 and $1/2$ and for $2/3$ aspect ratio the fractions are fixed respectively at $\sqrt{3}/2$, $1/2$ and $1/\sqrt{3}$.

It is crucial to mention that throughout the thesis, aspect ratio represents the ratio of arc angle to $2\pi$, not the ratio of height to length.

# 2. FORMULATIONS OF PHYSICAL LAWS IN CARTESIAN COORDINATES

The physical laws governing the fluid motion and heat transfer in Cartesian coordinates $(x, y)$ are expressed in terms of two-dimensional velocity components $\vec{\upsilon} = (u, \upsilon)$ by continuity, momentum and energy equations in figures (2.1)-(2.4). Density, $\rho$, of the fluid inside the cavity is assumed to be constant.

Continuity

$$\frac{\partial u}{\partial x} + \frac{\partial \upsilon}{\partial y} = 0 \tag{2.1}$$

x-Momentum

$$\frac{\partial u}{\partial t} + u\frac{\partial u}{\partial x} + \upsilon\frac{\partial u}{\partial y} = -\frac{1}{\rho}\frac{\partial P}{\partial x} + \nu\left(\frac{\partial^2 u}{\partial x^2} + \frac{\partial^2 u}{\partial y^2}\right) \tag{2.2}$$

y-Momentum

$$\frac{\partial \upsilon}{\partial t} + u\frac{\partial \upsilon}{\partial x} + \upsilon\frac{\partial \upsilon}{\partial y} = -\frac{1}{\rho}\frac{\partial P}{\partial y} + \nu\left(\frac{\partial^2 \upsilon}{\partial x^2} + \frac{\partial^2 \upsilon}{\partial y^2}\right) + g\,\beta\,(T - T_C) \tag{2.3}$$

Energy

$$\begin{aligned}\rho C_p\left(\frac{\partial T}{\partial t} + u\frac{\partial T}{\partial x} + \upsilon\frac{\partial T}{\partial y}\right) &= k\left(\frac{\partial^2 T}{\partial x^2} + \frac{\partial^2 T}{\partial y^2}\right) + \mu\Phi \\ &\quad + \beta T\left(\frac{\partial P}{\partial t} + u\frac{\partial P}{\partial x} + \upsilon\frac{\partial P}{\partial y}\right)\end{aligned} \tag{2.4}$$

$k$ is the thermal conductivity and $\rho C_P$ is defined as the volumetric heat capacity. $\mu$ and $\nu$ denote the absolute and kinematic viscosities, respectively. $T$ is the temperature and $P$ stands for the pressure term. $\beta$ is the coefficient of thermal expansion which is defined as

$$\beta = -\frac{1}{\rho}\frac{\partial \rho}{\partial T}\bigg|_{\rho = cons\tan t} . \tag{2.5}$$

The Boussinesq approximation is used to emphasize the effect of buoyancy force in the y component of momentum equation. It states that density differences are sufficiently small to be neglected, except where they are multiplied by g, the acceleration due to gravity. Meanwhile, viscous dissipation function, $\Phi$, which characterizes the irreversible conversion of energy in mechanical form into a thermal form, is neglected. Therefore, the constant density energy equation without viscous dissipation function is simplified to

$$\frac{\partial T}{\partial t} + u\frac{\partial T}{\partial x} + \upsilon\frac{\partial T}{\partial y} = \alpha \left(\frac{\partial^2 T}{\partial x^2} + \frac{\partial^2 T}{\partial y^2}\right), \tag{2.6}$$

where the thermal diffusivity, $\alpha$ is expressed as

$$\alpha = \frac{k}{\rho C_P} .$$

The coupling between heat transfer and fluid flow takes place through the buoyancy force included as an external source term in the momentum equation (2.3). Temperature boundary conditions are specified such that to generate the buoyancy effect by the temperature gradient across the stationary bottom wall and the moving top lid of the cavity. That is why the stationary arc shape bottom wall is maintained at the higher temperature, $T_H$, while the upper moving lid is maintained at the lower temperature, $T_L$.

For the solid wall boundaries, velocity components are prescribed by impermeable, no slip boundary conditions. Since no fluid passes through the wall, impermeable boundary condition requires that the velocity component normal to the wall must be zero. Thus, if $\vec{n}$ represents outward normal vector at a solid wall, impermeability condition states that

$$\vec{\upsilon}.\vec{n} = 0 .$$

Furthermore, the lid driven cavity is idealized with no slip boundary condition which indicates that tangential velocity component for the stationary bottom wall is zero and it is equal to the specified lid speed at the top. Then, no-slip boundary condition requires that

$$\vec{\upsilon} . \vec{s} = U_{wall} ,$$

where $\vec{s}$ denotes the tangent vector at a solid wall. $U_{wall}$ is zero at the bottom stationary wall and at the top it is specified with a constant speed, $U_L$.

Equations (2.1)-(2.4) are written in primitive variable form where $P$ and $\vec{\upsilon} = (u, \upsilon)$ are the primitive variables. However, the numerical scheme developed to solve the lid driven cavity flow can be simplified by using the new governing equations derived from the classical Navier-Stokes and continuity equations. These simplifications will result in elimination of pressure term which is one of the unknowns together with the velocity term in Navier stokes equations. Therefore, in this investigation instead of primitive velocity-pressure approach, vorticity-stream function formulation is conducted. This formulation is mainly used in two-dimensional applications due to the definition of stream function which exists only for two-dimensional flow. Besides the advantage of vorticity-stream function formulation the difficulty emerges when dealing with vorticity boundary conditions. As a result, the new vorticity boundary conditions for the specified geometry in curvilinear coordinates are presented and the derivations are written thoroughly in section (4).

## 2.1. Vorticity-Stream Function Formulation

Vorticity-stream function formulation as an alternative for the primitive variable form of Navier-Stokes equations presents useful insights into the behavior of the fluid. This formulation has been used frequently in numerical techniques. However, the vorticity-stream function formulation has some disadvantages. For example, boundary data are usually available in terms of primitive variables. The resultant boundary conditions of the vorticity are not readily obtained. On the other hand, its main advantage is the removal of pressure term from the governing equations.

For a two-dimensional flow field, velocity components, $\vec{\upsilon} = (u, \upsilon)$, can be introduced in terms of stream function, $\varphi$, as

$$u = \frac{\partial \varphi}{\partial y} \qquad \upsilon = -\frac{\partial \varphi}{\partial x}, \tag{2.7}$$

while, vorticity, $\omega$, is defined by

$$\omega = \frac{\partial \upsilon}{\partial x} - \frac{\partial u}{\partial y}. \tag{2.8}$$

Insertion of equation (2.7) into equation (2.8) shows that

$$\frac{\partial^2 \varphi}{\partial^2 x} + \frac{\partial^2 \varphi}{\partial^2 y} = -\omega, \tag{2.9}$$

where, equation (2.9) is known as the stream function equation. It is a Poisson type elliptic equation. Cross-differentiation of equation (2.2) with respect to $y$ and equation (2.3) with respect to $x$ and subtracting from each other yields

$$\begin{aligned}
&\frac{\partial}{\partial t}\left(\frac{\partial \upsilon}{\partial x} - \frac{\partial u}{\partial y}\right) + \frac{\partial u}{\partial x}\frac{\partial \upsilon}{\partial x} + u\frac{\partial^2 \upsilon}{\partial x^2} + \frac{\partial \upsilon}{\partial x}\frac{\partial \upsilon}{\partial y} + \upsilon\frac{\partial^2 \upsilon}{\partial x \partial y} - \frac{\partial u}{\partial y}\frac{\partial u}{\partial x} - u\frac{\partial^2 u}{\partial x \partial y} \\
&-\frac{\partial \upsilon}{\partial y}\frac{\partial u}{\partial y} - \upsilon\frac{\partial^2 u}{\partial y^2} = \nu\left(\frac{\partial^3 \upsilon}{\partial x^3} + \frac{\partial^3 \upsilon}{\partial x \partial y^2} - \frac{\partial^3 u}{\partial y \partial x^2} - \frac{\partial^3 u}{\partial y^3}\right) + g\beta\frac{\partial T}{\partial x} \quad ,
\end{aligned} \tag{2.10}$$

and after some re-arrangements equation (2.10) appears as

$$\begin{aligned}
&\frac{\partial}{\partial t}\left(\frac{\partial \upsilon}{\partial x} - \frac{\partial u}{\partial y}\right) + \frac{\partial}{\partial x}\left[u\left(\frac{\partial \upsilon}{\partial x} - \frac{\partial u}{\partial y}\right)\right] + \frac{\partial}{\partial y}\left[u\left(\frac{\partial \upsilon}{\partial x} - \frac{\partial u}{\partial y}\right)\right] \\
&= \nu\left[\frac{\partial^2}{\partial x^2}\left(\frac{\partial \upsilon}{\partial x} - \frac{\partial u}{\partial y}\right) + \frac{\partial^2}{\partial y^2}\left(\frac{\partial \upsilon}{\partial x} - \frac{\partial u}{\partial y}\right)\right] + g\,\beta\frac{\partial T}{\partial x} \quad .
\end{aligned} \tag{2.11}$$

Finally, by replacing equation (2.8) into equation (2.11), vorticity-transport equation emerges as

$$\frac{\partial \omega}{\partial t}+\frac{\partial(u\omega)}{\partial x}+\frac{\partial(\upsilon\omega)}{\partial y}=\nu\left(\frac{\partial^2\omega}{\partial x^2}+\frac{\partial^2\omega}{\partial y^2}\right)+g\,\beta\frac{\partial T}{\partial x}. \tag{2.12}$$

By using the vorticity-stream function formulation, due to the change of variables, the mixed parabolic-elliptic Navier-Stokes equations are separated into one parabolic equation and one elliptic equation.

### 2.2. Non-Dimensionalization of Governing Equations

In this study because of the theoretical advantages and computational benefits, non-dimensional forms of the governing equations are derived and used. The variables in equations (2.9) and (2.12) are non-dimensionalized using following definitions.

$$\begin{aligned}
&\tau=\frac{U_L t}{L} \qquad \Omega=\frac{\omega L}{U_L} \qquad U=\frac{u}{U_L} \qquad V=\frac{\upsilon}{U_L}\\
&Y=\frac{y}{L} \qquad X=\frac{x}{L} \qquad \theta=\frac{T-T_L}{T_H-T_L} \qquad \psi=\frac{\varphi}{U_L L}
\end{aligned} \tag{2.13}$$

The non-dimensional control parameters are defined as

$$\mathrm{Re}=\frac{U_L L}{\nu} \qquad \mathrm{Pr}=\frac{\nu}{\alpha} \qquad Ri=\frac{g\,\beta\,(T_H-T_L)\,L}{U_L}. \tag{2.14}$$

In equation (2.14) Reynolds number, $\mathrm{Re}$, denotes the ratio of inertial forces to viscous forces while Prandtl number, $\mathrm{Pr}$, is the ratio of viscosity to thermal diffusivity and Richardson number, $Ri$, is another parameter that signifies the effect of thermal convection and represents the importance of natural convection relative to forced convection.

Using equations (2.13) and (2.14), vorticity, energy and stream function equations can be represented in non-dimensional configurations. Then, the non-dimensional vorticity-transport equation emerges as

$$\frac{\partial \Omega}{\partial \tau}+\frac{\partial (U\Omega)}{\partial X}+\frac{\partial (V\Omega)}{\partial Y}=\frac{1}{\mathrm{Re}}\left(\frac{\partial^2 \Omega}{\partial X^2}+\frac{\partial^2 \Omega}{\partial Y^2}\right)+Ri\frac{\partial \theta}{\partial X}. \tag{2.15}$$

While energy equation which is simplified in equation (2.6) can be rewritten as

$$\frac{\partial T}{\partial t}+\frac{\partial (uT)}{\partial x}+\frac{\partial (\upsilon T)}{\partial y}-T\left(\frac{\partial u}{\partial x}+\frac{\partial \upsilon}{\partial y}\right)=\alpha\left(\frac{\partial^2 T}{\partial x^2}+\frac{\partial^2 T}{\partial y^2}\right). \tag{2.16}$$

Then, the dimensionless energy equation yields

$$\frac{\partial \theta}{\partial \tau}+\frac{\partial (U\theta)}{\partial X}+\frac{\partial (V\theta)}{\partial Y}=\frac{1}{\mathrm{Re}\,\mathrm{Pr}}\left(\frac{\partial^2 \theta}{\partial X^2}+\frac{\partial^2 \theta}{\partial Y^2}\right). \tag{2.17}$$

Finally, by applying equations (2.13) and (2.14) into the equation (2.9), the non-dimensional stream function equation appears as

$$\frac{\partial^2 \psi}{\partial^2 X}+\frac{\partial^2 \psi}{\partial^2 Y}=-\,\Omega\,. \tag{2.21}$$

# 3. NUMERICAL GRID GENERATION

Grid generation techniques as a result of mapping from the complex physical domain to the rectangular computational domain are mainly introduced to overcome the difficulties emerging by the complexity of geometry. Meanwhile, this mapping has some other advantages. For example, body surface can be selected as a boundary in the computational plane permitting easy application of surface boundary conditions. Moreover, transformation leads to uniformly spaced grids in the computational rectangular plane instead of unequally spaced nodes in the complex physical plane. In order to achieve a suitable mesh, mapping must be one to one and grid lines should be smooth such that continuous transformation derivatives are provided.

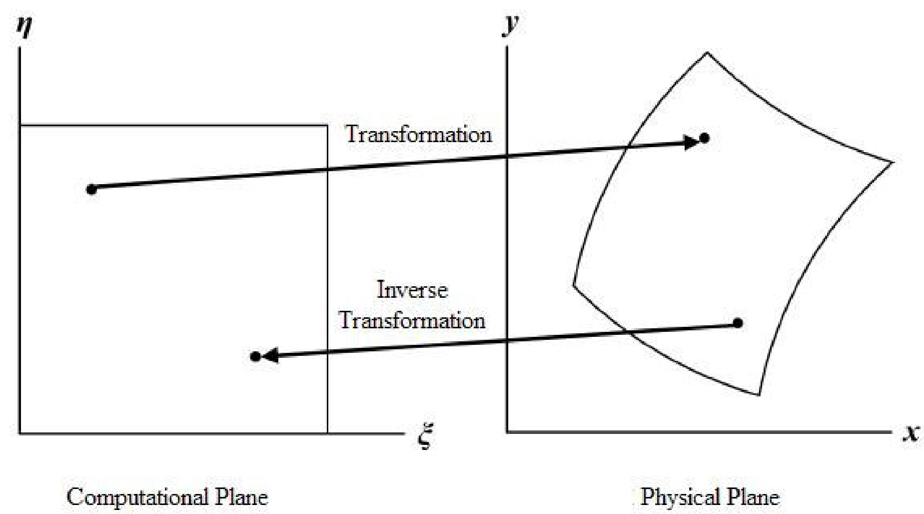


Figure 3.1. Mapping from physical to computational plane and vice versa [16]

## 3.1. Metrics of Transformation

The general transformation [30] from the physical plane $(x\,,\,y)$ to the transformed computational plane $(\xi\,,\eta)$ is defined as

$$\xi = \xi\ (x\,,\,y) \tag{3.1}$$

$$\eta = \eta\ (x\,,\,y)\,. \tag{3.2}$$

Similarly, the inverse transformation yields

$$x = x\ (\xi\ , \eta) \tag{3.3}$$

$$y = y\ (\xi\ , \eta)\,. \tag{3.4}$$

By the chain rule applied for the partial differential equations one can obtain

$$\frac{\partial}{\partial x} = \frac{\partial \xi}{\partial x}\frac{\partial}{\partial \xi} + \frac{\partial \eta}{\partial x}\frac{\partial}{\partial \eta} = \xi_x\ \frac{\partial}{\partial \xi} + \eta_x\ \frac{\partial}{\partial \eta} \tag{3.5}$$

$$\frac{\partial}{\partial y} = \frac{\partial \xi}{\partial y}\frac{\partial}{\partial \xi} + \frac{\partial \eta}{\partial y}\frac{\partial}{\partial \eta} = \xi_y\ \frac{\partial}{\partial \xi} + \eta_y\ \frac{\partial}{\partial \eta}\,, \tag{3.6}$$

where $\xi_x$, $\xi_y$, $\eta_x$ and $\eta_y$ are the transformation derivatives which are defined as the metrics of transformation. The metric symbolizes the ratio of arc length in the computational space to the arc length in the physical space [31]. Then from the relations given in equations (3.1) and (3.2) the following definitions are achieved.

$$d\xi = \xi_x dx + \xi_y dy \tag{3.7}$$

$$d\eta = \eta_x dx + \eta_y dy \tag{3.8}$$

Equations (3.7) and (3.8) can be represented in a matrix form as

$$\begin{bmatrix} d\xi \\ d\eta \end{bmatrix} = \begin{bmatrix} \xi_x & \xi_y \\ \eta_x & \eta_y \end{bmatrix} \begin{bmatrix} dx \\ dy \end{bmatrix}. \tag{3.9}$$

By defining the inverse transformation which is expressed in equations (3.3) and (3.4), we can get

$$dx = x_\xi d\xi + x_\eta d\eta \tag{3.10}$$

$$dy = y_\xi d\xi + y_\eta d\eta\,. \tag{3.11}$$

While, equations (3.10) and (3.11) can be given in a matrix form as

$$\begin{bmatrix} dx \\ dy \end{bmatrix} = \begin{bmatrix} x_\xi & x_\eta \\ y_\xi & y_\eta \end{bmatrix} \begin{bmatrix} d\xi \\ d\eta \end{bmatrix}. \tag{3.12}$$

Using equations (3.9) and (3.12) it can be stated that

$$\begin{bmatrix} \xi_x & \xi_y \\ \eta_x & \eta_y \end{bmatrix} = \begin{bmatrix} x_\xi & x_\eta \\ y_\xi & y_\eta \end{bmatrix}^{-1}. \tag{3.13}$$

Then, the transformation metrics emerge as

$$\xi_x = \frac{y_\eta}{J} \tag{3.14}$$

$$\xi_y = -\frac{x_\eta}{J} \tag{3.15}$$

$$\eta_x = -\frac{y_\xi}{J} \tag{3.16}$$

$$\eta_y = \frac{x_\xi}{J}, \tag{3.17}$$

where, $J$ is the Jacobian of transformation which is the ratio of the areas in the physical space to that of the computational space and it is expressed as

$$J = x_\xi y_\eta - x_\eta y_\xi. \tag{3.18}$$

Derivatives of the metrics of transformation have to be defined to identify the governing equations in curvilinear coordinates and to generate computational grids. Then the derivatives of metrics can be derived from their definitions which are given in equation (3.14)-(3.17). Then the derivatives of transformation metrics are obtained as

$$\frac{\partial}{\partial \xi}(\xi_x) = \frac{\partial}{\partial \xi}\left(\frac{y_\eta}{J}\right) = \frac{\partial}{\partial \xi}\left(\frac{y_\eta}{x_\xi y_\eta - x_\eta y_\xi}\right)$$
$$= \frac{1}{J^2}\left[y_{\xi\eta}(x_\xi y_\eta - x_\eta y_\xi) - y_\eta(x_{\xi\xi} y_\eta + x_\xi y_{\xi\eta} - x_\eta y_{\xi\xi} - x_{\xi\eta} y_\xi)\right] \tag{3.19}$$

$$\frac{\partial}{\partial \xi}(\xi_y) = -\frac{1}{J^2}\left[x_{\xi\eta}(x_\xi y_\eta - x_\eta y_\xi) - x_\eta(x_{\xi\xi} y_\eta + x_\xi y_{\xi\eta} - x_\eta y_{\xi\xi} - x_{\xi\eta} y_\xi)\right] \tag{3.20}$$

$$\frac{\partial}{\partial \xi}(\eta_x) = -\frac{1}{J^2}\left[y_{\xi\xi}(x_\xi y_\eta - x_\eta y_\xi) - y_\xi(x_{\xi\xi} y_\eta + x_\xi y_{\xi\eta} - x_\eta y_{\xi\xi} - x_{\xi\eta} y_\xi)\right] \tag{3.21}$$

$$\frac{\partial}{\partial \xi}(\eta_y) = \frac{1}{J^2}\left[x_{\xi\xi}(x_\xi y_\eta - x_\eta y_\xi) - x_\xi(x_{\xi\xi} y_\eta + x_\xi y_{\xi\eta} - x_\eta y_{\xi\xi} - x_{\xi\eta} y_\xi)\right] \tag{3.22}$$

$$\frac{\partial}{\partial \eta}(\xi_x) = \frac{1}{J^2}\left[y_{\eta\eta}(x_\xi y_\eta - x_\eta y_\xi) - y_\eta(x_{\eta\xi} y_\eta + x_\xi y_{\eta\eta} - x_\eta y_{\eta\xi} - x_{\eta\eta} y_\xi)\right] \tag{3.23}$$

$$\frac{\partial}{\partial \eta}(\xi_y) = -\frac{1}{J^2}\left[x_{\eta\eta}(x_\xi y_\eta - x_\eta y_\xi) - x_\eta(x_{\eta\xi} y_\eta + x_\xi y_{\eta\eta} - x_\eta y_{\eta\xi} - x_{\eta\eta} y_\xi)\right] \tag{3.24}$$

$$\frac{\partial}{\partial \eta}(\eta_x) = -\frac{1}{J^2}\left[y_{\xi\eta}(x_\xi y_\eta - x_\eta y_\xi) - y_\eta(x_{\eta\xi} y_\eta + x_\xi y_{\eta\eta} - x_\eta y_{\eta\xi} - x_{\eta\eta} y_\xi)\right] \tag{3.25}$$

$$\frac{\partial}{\partial \eta}(\eta_y) = \frac{1}{J^2}\left[x_{\xi\eta}(x_\xi y_\eta - x_\eta y_\xi) - x_\eta(x_{\eta\xi} y_\eta + x_\xi y_{\eta\eta} - x_\eta y_{\eta\xi} - x_{\eta\eta} y_\xi)\right]. \tag{3.26}$$

### 3.2. First and Second Derivatives in Computational Domain

By replacing the metrics of transformation into the equations (3.5) and (3.6) for any variable $f$, one can obtain the first derivatives as [31]

$$\frac{\partial f}{\partial x} = J^{-1}\left( y_\eta \frac{\partial f}{\partial \xi} - y_\xi \frac{\partial f}{\partial \eta} \right) = J^{-1}\left( y_\eta \ f_\xi - y_\xi \ f_\eta \right) \tag{3.27}$$

$$\frac{\partial f}{\partial y} = J^{-1}\left( x_\xi \frac{\partial f}{\partial \eta} - x_\eta \frac{\partial f}{\partial \xi} \right) = J^{-1}\left( x_\xi \ f_\eta - x_\eta \ f_\xi \right). \tag{3.28}$$

Now, the second derivatives need to be derived based on the already obtained first ones.

$$\begin{aligned}
\frac{\partial^2 f}{\partial x^2} &= \frac{\partial}{\partial x}\left(\frac{\partial f}{\partial x}\right) = \frac{\partial}{\partial x}\left(\xi_x \ f_\xi + \eta_x \ f_\eta\right) \\
&= \left(\xi_x \frac{\partial}{\partial \xi} + \eta_x \frac{\partial}{\partial \eta}\right)\left(\xi_x \ f_\xi + \eta_x \ f_\eta\right) \\
&= \xi_x \frac{\partial}{\partial \xi}\left(\xi_x \ f_\xi + \eta_x \ f_\eta\right) + \eta_x \frac{\partial}{\partial \eta}\left(\xi_x \ f_\xi + \eta_x \ f_\eta\right) \\
&= \xi_x^2 f_{\xi\xi} + \xi_x f_\xi \frac{\partial}{\partial \xi}(\xi_x) + \xi_x \eta_x f_{\xi\eta} + \xi_x f_\eta \frac{\partial}{\partial \xi}(\eta_x) \\
&\quad + \eta_x \xi_x f_{\xi\eta} + \eta_x f_\xi \frac{\partial}{\partial \eta}(\xi_x) + \eta_x^2 f_{\eta\eta} + \eta_x f_\eta \frac{\partial}{\partial \eta}(\eta_x)
\end{aligned} \tag{3.29}$$

By replacing the metrics of transformation, equation (3.29) emerges as

$$\begin{aligned}
\frac{\partial^2 f}{\partial x^2} &= \frac{1}{J^2}\left(y_\eta^2 f_{\xi\xi} - 2 y_\xi y_\eta f_{\xi\eta} + y_\xi^2 f_{\eta\eta}\right) \\
&\quad + \frac{1}{J} y_\eta \left( f_\xi \frac{\partial}{\partial \xi}(\xi_x) + f_\eta \frac{\partial}{\partial \xi}(\eta_x) \right) \\
&\quad - \frac{1}{J} y_\xi \left( f_\xi \frac{\partial}{\partial \eta}(\xi_x) + f_\eta \frac{\partial}{\partial \eta}(\eta_x) \right).
\end{aligned} \tag{3.30}$$

Replacement of the derivatives of metrics obtained in equations (3.19), (3.21), (3.23) and (3.25), into the equation (3.30) yields

$$\frac{\partial^2 f}{\partial x^2} = \frac{1}{J^2}\left(y_\eta^2 f_{\xi\xi} - 2y_\xi y_\eta f_{\xi\eta} + y_\xi^2 f_{\eta\eta}\right)$$
$$+\frac{1}{J^3}\left(y_\eta^2 y_{\xi\xi} - 2y_\eta y_\xi y_{\xi\eta} + y_\xi^2 y_{\eta\eta}\right)\left(x_\eta f_\xi - x_\xi f_\eta\right) \tag{3.31}$$
$$+\frac{1}{J^3}\left(y_\eta^2 x_{\xi\xi} - 2y_\eta y_\xi x_{\xi\eta} + y_\xi^2 x_{\eta\eta}\right)\left(y_\xi f_\eta - y_\eta f_\xi\right).$$

While the same procedure is applied for $\frac{\partial^2 f}{\partial y^2}$ and it emerges as

$$\frac{\partial^2 f}{\partial y^2} = \frac{1}{J^2}\left(x_\eta^2 f_{\xi\xi} - 2x_\xi x_\eta f_{\xi\eta} + y_\xi^2 f_{\eta\eta}\right)$$
$$+\frac{1}{J^3}\left(x_\eta^2 y_{\xi\xi} - 2x_\eta x_\xi y_{\xi\eta} + x_\xi^2 y_{\eta\eta}\right)\left(x_\eta f_\xi - x_\xi f_\eta\right) \tag{3.32}$$
$$+\frac{1}{J^3}\left(y_\eta^2 x_{\xi\xi} - 2y_\eta y_\xi x_{\xi\eta} + y_\xi^2 x_{\eta\eta}\right)\left(y_\xi f_\eta - y_\eta f_\xi\right).$$

### 3.3. Elliptic Grid Generation

Solution of partial differential equations without selection and application of proper grid system for the specified geometry is undoubtedly impractical. It may results in lack of convergence and numerical instabilities during the iterations and the character of the solution definitely will change. On the other hand in the partial differential systems the defined boundary conditions are significantly dominant on the solution character. That is why the grid points not coincident with the boundaries results in inaccurate representation in the region of greatest sensitivity.

Elliptic grid generation method is conducted where the mapping is controlled by Laplace's equation and it is constructed by the desired grid points on the boundary of physical domain [29]. Then the curvilinear coordinates are generated by solving

$$\xi_{xx} + \xi_{yy} = 0 \tag{3.33}$$

$$\eta_{xx} + \eta_{yy} = 0\,. \tag{3.34}$$

Replacement of $\xi$ and $\eta$ in equations (3.31) and (3.32) in place of $f$ yields the following set of equations.

$$\xi_{xx} = \frac{1}{J^3}\Big[\left(y_\eta^2 y_{\xi\xi} - 2y_\eta y_\xi y_{\xi\eta} + y_\xi^2 y_{\eta\eta}\right)x_\eta - \left(y_\eta^2 x_{\xi\xi} - 2y_\eta y_\xi x_{\xi\eta} + y_\xi^2 x_{\eta\eta}\right)y_\eta\Big] \tag{3.35}$$

$$\eta_{xx} = \frac{1}{J^3}\Big[\left(y_\eta^2 x_{\xi\xi} - 2y_\eta y_\xi x_{\xi\eta} + y_\xi^2 x_{\eta\eta}\right)y_\xi - \left(y_\eta^2 y_{\xi\xi} - 2y_\eta y_\xi y_{\xi\eta} + y_\xi^2 y_{\eta\eta}\right)x_\xi\Big] \tag{3.36}$$

$$\xi_{yy} = \frac{1}{J^3}\Big[\left(x_\eta^2 y_{\xi\xi} - 2x_\xi x_\eta y_{\xi\eta} + x_\xi^2 y_{\eta\eta}\right)x_\eta - \left(x_\eta^2 x_{\xi\xi} - 2x_\eta x_\xi x_{\xi\eta} + x_\xi^2 x_{\eta\eta}\right)y_\eta\Big] \tag{3.37}$$

$$\eta_{yy} = \frac{1}{J^3}\Big[\left(x_\eta^2 x_{\xi\xi} - 2x_\eta x_\xi x_{\xi\eta} + x_\xi^2 x_{\eta\eta}\right)y_\xi - \left(x_\eta^2 y_{\xi\xi} - 2x_\eta x_\xi y_{\xi\eta} + x_\xi^2 y_{\eta\eta}\right)x_\xi\Big] \tag{3.38}$$

Insertion of equations (3.35) and (3.37) into equation (3.33) shows that

$$\left(x_\eta^2 + y_\eta^2\right)x_{\xi\xi} - 2\left(x_\xi x_\eta + y_\xi y_\eta\right)x_{\xi\eta} + \left(x_\xi^2 + y_\xi^2\right)x_{\eta\eta} = 0 \ . \tag{3.39}$$

While, placing of equations (3.36) and (3.38) into equation (3.34) yields

$$\left(x_\eta^2 + y_\eta^2\right)y_{\xi\xi} - 2\left(x_\xi x_\eta + y_\xi y_\eta\right)y_{\xi\eta} + \left(x_\xi^2 + y_\xi^2\right)y_{\eta\eta} = 0 \, . \tag{3.40}$$

Finally, the resulted transformed equations are

$$\alpha\, x_{\xi\xi} - 2\beta\, x_{\xi\eta} + \gamma\, x_{\eta\eta} = 0 \tag{3.41}$$

$$\alpha\, y_{\xi\xi} - 2\beta\, y_{\xi\eta} + \gamma\, y_{\eta\eta} = 0 \, , \tag{3.42}$$

where, $\alpha, \beta, \gamma$ are the coordinate transformations coefficients represented by the following equations.

$$\begin{aligned}
\alpha &= x_\eta^2 + y_\eta^2 \\
\beta &= x_\xi x_\eta + y_\xi y_\eta \\
\gamma &= x_\xi^2 + y_\xi^2
\end{aligned} \tag{3.43}$$

The differential equations of (3.41) and (3.42) are more complicated than equations (3.33) and (3.34). However, the boundary conditions of equations (3.41) and (3.42) are specified on straight boundaries with the rectangular computational domain. Therefore, the problem of simple equations with complex boundaries turns into the problem with complex equations but simple boundaries [29].

# 4. FORMULATIONS OF PHYSICAL LAWS IN CURVILINEAR COORDINATES

Based on the derivatives obtained in previous section and regarding specified dimensionless forms of the governing equations, a new set of governing equations for the curvilinear computational domain have to be obtained. Therefore, substitution of equations (3.31) and (3.32) into equation (2.21) and some simplifications yield

$$\frac{1}{J^2}\left(\alpha\psi_{\xi\xi}-2\beta\psi_{\xi\eta}+\gamma\psi_{\eta\eta}\right)=-\Omega. \tag{4.1}$$

Equation (4.1) is the stream function equation in curvilinear coordinates. Furthermore, energy and vorticity-transport equations are provided according to the derivatives obtained in section (3.2) and they are represented by the following equations.

$$\begin{aligned}&\frac{\partial\theta}{\partial\tau}+\frac{1}{J}\left(Y_\eta(U\theta)_\xi-Y_\xi(U\theta)_\eta+X_\xi(V\theta)_\xi-X_\eta(V\theta)_\xi\right)\\&=\frac{1}{\mathrm{Re}\,\mathrm{Pr}}\frac{1}{J^2}\left(\alpha\theta_{\xi\xi}-2\beta\theta_{\xi\eta}+\gamma\theta_{\eta\eta}\right)\end{aligned} \tag{4.2}$$

$$\begin{aligned}&\frac{\partial\Omega}{\partial\tau}+\frac{1}{J}\left(Y_\eta(U\Omega)_\xi-Y_\xi(U\Omega)_\eta+X_\xi(V\Omega)_\xi-X_\eta(V\Omega)_\xi\right)\\&=\frac{1}{\mathrm{Re}}\frac{1}{J^2}\left(\alpha\Omega_{\xi\xi}-2\beta\Omega_{\xi\eta}+\gamma\Omega_{\eta\eta}\right)+\frac{Ri}{J}\left(Y_\eta\theta_\xi-Y_\xi\theta_\eta\right)\end{aligned} \tag{4.3}$$

Since there are no specifically defined boundary conditions for the vorticity, the boundary conditions for the computational plane must be created. The vorticity-transport and stream function equations can be summarized on a simply connected domain with no slip and no penetration boundary conditions as

$$\frac{\partial\psi}{\partial s}=0 \tag{4.4}$$

$$\frac{\partial\psi}{\partial n}=U_{Wall}\,, \tag{4.5}$$

where, $s$ symbolizes the tangential direction and $n$ represents the normal direction. $U_{Wall}$ denotes the tangential velocity which is prescribed as $U_L$ along the moving lid and it is zero elsewhere. For the stationary wall the prescribed velocity components are

$$U = \frac{\partial \psi}{\partial Y} = 0 \tag{4.6}$$

$$V = -\frac{\partial \psi}{\partial X} = 0\,. \tag{4.7}$$

While, for the moving lid equations (4.6) and (4.7) can be stated as

$$\begin{aligned} U &= \frac{\partial \psi}{\partial Y} \\ &= \frac{1}{J}\left[ X_\xi \frac{\partial \psi}{\partial \eta} - X_\eta \frac{\partial \psi}{\partial \xi} \right] \\ &= U_L \end{aligned} \tag{4.8}$$

$$\begin{aligned} V &= -\frac{\partial \psi}{\partial X} \\ &= -\frac{1}{J}\left[ Y_\eta \frac{\partial \psi}{\partial \xi} - Y_\xi \frac{\partial \psi}{\partial \eta} \right] \\ &= 0\,. \end{aligned} \tag{4.9}$$

Then, equation (4.9) yields

$$\frac{\partial \psi}{\partial \xi} = \frac{Y_\xi}{Y_\eta} \frac{\partial \psi}{\partial \eta}\,. \tag{4.10}$$

Insertion of equation (4.10) into equation (4.8) shows that

$$\begin{aligned} U_L &= \frac{X_\xi}{J}\left[ \frac{\partial \psi}{\partial \eta} - \frac{X_\eta Y_\xi}{X_\xi Y_\eta} \frac{\partial \psi}{\partial \eta} \right] \\ &= \frac{X_\xi}{J} \frac{\partial \psi}{\partial \eta} \left[ \frac{J}{X_\xi Y_\eta} \right]. \end{aligned} \tag{4.11}$$

Therefore, for the moving lid $\frac{\partial \psi}{\partial \eta}$ emerges as

$$\frac{\partial \psi}{\partial \eta} = Y_{\eta} U_{L} . \tag{4.12}$$

Now, the Taylor series expansion of stream function values for the horizontal boundaries in computational domain is represented as

$$\psi_{i,2} = \psi_{i,1} + \left.\frac{\partial \psi}{\partial \eta}\right|_{i,1} (\Delta \eta) + \left.\frac{\partial^2 \psi}{\partial \eta^2}\right|_{i,1} \frac{(\Delta \eta)^2}{2} . \tag{4.13}$$

While the Taylor series expansion of stream function values for the vertical boundaries in computational domain can be written as

$$\psi_{2,j} = \psi_{1,j} + \left.\frac{\partial \psi}{\partial \xi}\right|_{1,j} (\Delta \xi) + \left.\frac{\partial^2 \psi}{\partial \xi^2}\right|_{1,j} \frac{(\Delta \xi)^2}{2} . \tag{4.14}$$

Along the bottom and top surfaces of the cavity the stream function values are constant. Then for these surfaces it can be given that

$$\frac{\partial^2 \psi}{\partial \xi^2} = 0 . \tag{4.15}$$

Therefore, considering the bottom stationary wall, the stream function equation of (4.1) is reduced to

$$\Omega_{i,1} = -\frac{\gamma}{J^2} \left.\psi_{\eta\eta}\right|_{i,1} . \tag{4.16}$$

Rearranging equation (4.13) yields

$$\left.\frac{\partial^2\psi}{\partial\eta^2}\right|_{i,1} = \frac{2}{(\Delta\eta)^2}\left(\psi_{i,2} - \psi_{i,1}\right). \tag{4.17}$$

Substitution of equation (4.17) into equation (4.16) gives the vorticity boundary condition for the bottom stationary wall.

$$\Omega_{i,1} = \frac{2\,\gamma}{(\Delta\eta)^2\;J^2}\left(\psi_{i,1} - \psi_{i,2}\right). \tag{4.18}$$

Taylor series expansion for the lid can be expressed as

$$\psi_{i,\max j-1} = \psi_{i,\max j} - \left.\frac{\partial\psi}{\partial\eta}\right|_{i,\max j}(\Delta\eta) + \left.\frac{\partial^2\psi}{\partial\eta^2}\right|_{i,\max j}\frac{(\Delta\eta)^2}{2}. \tag{4.19}$$

Insertion of equation (4.12) into equation (4.19) yields

$$\left.\frac{\partial^2\psi}{\partial\eta^2}\right|_{i,\max j} = \frac{2}{(\Delta\eta)^2}\left(\psi_{i,\max j-1} - \psi_{i,\max j}\right) + \frac{2}{(\Delta\eta)}Y_\eta U_L. \tag{4.20}$$

By considering equation (4.15), substitution of equation (4.20) into equation (4.1) results in formation of the vorticity boundary condition for the top moving lid as

$$\Omega_{i,\max j} = \frac{2\,\gamma}{(\Delta\eta)^2 J^2}\left(\psi_{i,\max j} - \psi_{i,\max j-1}\right) - \frac{2}{(\Delta\eta)}Y_\eta U_L. \tag{4.21}$$

# 5. NUMERICAL METHOD

## 5.1. Discretization of Governing Equations

Governing partial differential equations of fluid flow and heat convection need to be discretized and it is performed by replacing the derivatives of differential equations by numerically solvable finite difference approximations. This method provides a large algebraic set of equations instead of differential equations. Then, the dependent variables are assumed to exist only at discrete points and transformed governing equations can be solved by specific iteration techniques applied for every grid points. In this thesis forward time-centered space finite difference scheme is used for the discretization of the vorticity-transport, stream function and energy equations and the resulted formulations are represented below, respectively.

$$
\begin{aligned}
&\frac{\Omega^{n+1}_{i,j}-\Omega^{n}_{i,j}}{\Delta t}+\frac{1}{2\,J_{i,j}}\left(\frac{Y_{i,j+1}-Y_{i,j-1}}{\Delta\eta}\,\frac{\Omega^{n}_{i+1,j}U^{n}_{i+1,j}-\Omega^{n}_{i-1,j}U^{n}_{i-1,j}}{\Delta\xi}\right.\\
&-\frac{Y_{i+1,j}-Y_{i-1,j}}{\Delta\xi}\,\frac{\Omega^{n}_{i,j+1}U^{n}_{i,j+1}-\Omega^{n}_{i,j-1}U^{n}_{i,j-1}}{\Delta\eta}+\frac{X_{i+1,j}-X_{i-1,j}}{\Delta\xi}\\
&\left.\frac{\Omega^{n}_{i,j+1}V^{n}_{i,j+1}-\Omega^{n}_{i,j-1}V^{n}_{i,j-1}}{\Delta\eta}-\frac{X_{i,j+1}-X_{i,j-1}}{\Delta\eta}\,\frac{\Omega^{n}_{i+1,j}V^{n}_{i+1,j}-\Omega^{n}_{i-1,j}V^{n}_{i-1,j}}{\Delta\xi}\right)\\
&=\frac{1}{J^{2}_{i,j}\,\mathrm{Re}}\left(\alpha_{i,j}\,\frac{\Omega^{n}_{i+1,j}-2\,\Omega^{n}_{i,j}+\Omega^{n}_{i-1,j}}{\Delta\xi^{2}}\right.\\
&\left.-\beta_{i,j}\,\frac{\Omega^{n}_{i+1,j+1}-\Omega^{n}_{i+1,j-1}+\Omega^{n}_{i-1,j-1}-\Omega^{n}_{i-1,j+1}}{2\,\Delta\xi\,\Delta\eta}+\gamma_{i,j}\,\frac{\Omega^{n}_{i,j+1}-2\,\Omega^{n}_{i,j}+\Omega^{n}_{i,j-1}}{\Delta\eta^{2}}\right)\\
&+\frac{Ri}{2\,J_{i,j}}\left(\frac{Y_{i,j+1}-Y_{i,j-1}}{\Delta\eta}\,\frac{\theta^{n}_{i+1,j}-\theta^{n}_{i-1,j}}{\Delta\xi}-\frac{Y_{i+1,j}-Y_{i-1,j}}{\Delta\xi}\,\frac{\theta^{n}_{i,j+1}-\theta^{n}_{i,j-1}}{\Delta\eta}\right)
\end{aligned}
\tag{5.1}
$$

$$
\begin{aligned}
&\left(\alpha_{i,j}\,\frac{\psi^{n}_{i+1,j}-2\psi^{n}_{i,j}+\psi^{n}_{i-1,j}}{\Delta\xi^{2}}-\beta_{i,j}\,\frac{\psi^{n}_{i+1,j+1}-\psi^{n}_{i+1,j-1}+\psi^{n}_{i-1,j-1}-\psi^{n}_{i-1,j+1}}{2\,\Delta\xi\,\Delta\eta}\right.\\
&\left.+\gamma_{i,j}\,\frac{\psi^{n}_{i,j+1}-2\psi^{n}_{i,j}+\psi^{n}_{i,j-1}}{\Delta\eta^{2}}\right)=-\,J^{2}\,\Omega
\end{aligned}
\tag{5.2}
$$

$$\frac{\Omega_{i,j}^{n+1}-\Omega_{i,j}^{n}}{\Delta t}+\frac{1}{2\,J_{i,j}}\left(\frac{Y_{i,j+1}-Y_{i,j-1}}{\Delta\eta}\frac{\theta_{i+1,j}^{n}U_{i+1,j}^{n}-\theta_{i-1,j}^{n}U_{i-1,j}^{n}}{\Delta\xi}\right.$$
$$-\frac{Y_{i+1,j}-Y_{i-1,j}}{\Delta\xi}\frac{\theta_{i,j+1}^{n}U_{i,j+1}^{n}-\theta_{i,j-1}^{n}U_{i,j-1}^{n}}{\Delta\eta}+\frac{X_{i+1,j}-X_{i-1,j}}{\Delta\xi}$$
$$\left.\frac{\theta_{i,j+1}^{n}V_{i,j+1}^{n}-\theta_{i,j-1}^{n}V_{i,j-1}^{n}}{\Delta\eta}-\frac{X_{i,j+1}-X_{i,j-1}}{\Delta\eta}\frac{\theta_{i+1,j}^{n}V_{i+1,j}^{n}-\theta_{i-1,j}^{n}V_{i-1,j}^{n}}{\Delta\xi}\right) \tag{5.3}$$
$$=\frac{1}{J_{i,j}^{2}\ \mathrm{Re}}\left(\alpha_{i,j}\frac{\theta_{i+1,j}^{n}-2\theta_{i,j}^{n}+\theta_{i-1,j}^{n}}{\Delta\xi^{2}}\right.$$
$$\left.-\beta_{i,j}\frac{\theta_{i+1,j+1}^{n}-\theta_{i+1,j-1}^{n}+\theta_{i-1,j-1}^{n}-\theta_{i-1,j+1}^{n}}{2\,\Delta\xi\,\Delta\eta}+\gamma_{i,j}\frac{\theta_{i,j+1}^{n}-2\theta_{i,j}^{n}+\theta_{i,j-1}^{n}}{\Delta\eta^{2}}\right)$$

These three equations of fluid flow and heat transfer have to be solved by appropriate numerical techniques. Parabolic energy and vorticity equations are solved via the Adams-Bashforth third order method. On the other hand, the stream function equation is an elliptic Poisson equation which is iterated by the successive over relaxation (SOR) method. Furthermore, Chebyshev acceleration is adopted within the SOR algorithm for faster convergence of stream function values.

### 5.1.1. Time Integration Algorithm

The explicit Adams-Bashforth third order discretization, which is a predictor method, applied for the governing parabolic unsteady energy and vorticity-transport equations. It provides an efficient way for time stepping. The Buoyancy term in the vorticity equation results in smooth coupling between the temperature and the vorticity equations. To demonstrate this scheme, consider the N$^{th}$ order Adams-Bashforth approximation to the ordinary differential equation

$$\frac{d\phi}{dt}=f(\phi), \tag{5.4}$$

which, has the form

$$\frac{\lambda^{n+1} - \lambda^{n}}{\Delta t} = \sum_{i=0}^{N-1} c_i \ f\left(\lambda^{n-i}\right). \tag{5.5}$$

In this equation $c_i$ is a constant that can be obtained by substituting the Taylor series expansion for $\phi$ and $f(\phi)$ into the equation (5.5) and choosing the $c_i$ such that all the terms less than $(\Delta t)^N$ are cancelled. $\lambda^n$ is the numerical approximation to $\phi(n\,\Delta t)$. Equation (5.4) can be represented as an equivalent integral equation as

$$\phi^{n+1} - \phi^{n} = \int_{n}^{(n+1)} f(\phi(t))\, dt\ . \tag{5.6}$$

Equation (5.6) would be approximated by Adams-Bashforth scheme as

$$\int_{n\,\Delta t}^{(n+1)\Delta t} f(\phi(t))\, dt = \Delta t \sum_{i=0}^{N-1} c_i \ f\left(\lambda^{n-i}\right). \tag{5.7}$$

For the first order Adams-Bashforth scheme the constant is $c_0 = 1$ and for the second order it is given as $c_0 = \frac{3}{2}$ and $c_1 = -\frac{1}{2}$. Finally, the third order Adams-Bashforth scheme yields

$$\lambda^{n+1} - \lambda^{n} = \frac{\Delta t}{12}\left\{ 23\ f\left(\lambda^{n}\right) - 16\ f\left(\lambda^{n-1}\right) + 5\ f\left(\lambda^{n-2}\right)\right\}. \tag{5.8}$$

### 5.1.2. Space Integration Algorithm

The Successive Over Relaxation (SOR) is a relaxation method which is mostly used for the solution of elliptic partial differential equations and it is applied to solve the Poisson stream function equation. Recall stream function equation (2.21) which is derived for Cartesian coordinates as

$$\frac{\partial^2\psi}{\partial^2 X}+\frac{\partial^2\psi}{\partial^2 Y}=-\,\Omega\,, \tag{2.21}$$

where, centered space discretization yields

$$\frac{\psi_{i+1,j}-2\,\psi_{i,j}+\psi_{i-1,j}}{(\Delta x)^2}+\frac{\psi_{i,j+1}-2\,\psi_{i,j}+\psi_{i,j-1}}{(\Delta y)^2}=-\Omega\,. \tag{5.9}$$

Assume, $\Delta x=\Delta y=\Delta$. Then equation (5.9) yields

$$\frac{1}{\Delta^2}\left(\psi_{i+1,j}+\psi_{i-1,j}+\psi_{i,j+1}+\psi_{i,j-1}-4\,\psi_{i,j}\right)=-\,\Omega\,. \tag{5.10}$$

Therefore, the iterative procedure is defined by solving equation (5.10) for $\psi_{i,j}$ as

$$\psi_{i,j}=\frac{\left(\psi_{i+1,j}+\psi_{i-1,j}+\psi_{i,j+1}+\psi_{i,j-1}\right)}{4}+\frac{\Delta^2}{4}\Omega\,. \tag{5.11}$$

Using the residual value at any stage which is obtained by

$$\Pi=\frac{1}{\Delta^2}\left(\psi_{i+1,j}+\psi_{i-1,j}+\psi_{i,j+1}+\psi_{i,j-1}-4\,\psi_{i,j}\right)+\Omega\,, \tag{5.12}$$

the new stream function, $\psi_{i,j}^{new}$ can be solved by iteration represented as

$$\psi_{i,j}^{new}=\psi_{i,j}^{old}+w\,\frac{\Pi}{4}\,, \tag{5.13}$$

where $w$ is called the over-relaxation parameter and the successive over relaxation method is convergent only for $0<w<2$ [28], while the optimal value can be achieved by

$$w=\frac{2}{1+\sqrt{1-\rho_{Jacobi}^2}}\,. \tag{5.14}$$

For this optimal choice the spectral radius for SOR is,

$$\rho_{SOR} = \left( \frac{\rho_{Jacobi}}{1+\sqrt{1-\rho_{Jacobi}^2}} \right)^2 , \tag{5.15}$$

where, for our problem on a rectangular grid of $J \times L$, $\rho_{Jacobi}$ is represented as

$$\rho_{Jacobi} = \frac{\cos\left(\frac{\pi}{J}\right) + \left(\frac{\Delta x}{\Delta y}\right)^2 \cos\left(\frac{\pi}{L}\right)}{1+\left(\frac{\Delta x}{\Delta y}\right)^2} . \tag{5.16}$$

Equation (5.11) shows that the odd points only depend on the even meshes and vice versa. Hence, we can divide the meshes into even and odd ordering and iteration continues by performing half-sweep to update the even points and then performing the other half-sweep to update the odd ones with the new even values. In this thesis the SOR method is used along with the Chebyshev acceleration which changes $w$ at each half-sweep consistent with the following formulation.

$$\begin{aligned} w^0 &= 1 \\ w^{1/2} &= \frac{1}{1-\frac{\rho_{Jacobi}^2}{2}} \\ w^{n+1/2} &= \frac{1}{1-\frac{\rho_{Jacobi}^2 \, w^n}{4}} \\ w^\infty &\to w_{optimal} \end{aligned} \tag{5.17}$$

Where, $n = 1/2 , 1 , \ldots , \infty$.

## 5.2. Code Validation

Validation of the algorithm written for the investigation of inertia and buoyancy induced flow for lid-driven arc shape cavity is performed by comparing the results obtained by the numerical procedure used in this study and the results of most recent investigations of Chen and Cheng [19], [20]. Based on these comparisons it can be stated that the results obtained via the algorithm written for this thesis is in close agreement with the previous works' results for the same geometry, flow and thermal conditions.

In their studies Chen and Cheng mainly have worked on small aspect ratio cavities. Therefore their 1/3 aspect ratio cavity is selected and adapted to the algorithm to validate the results. The computational domain is discretized as described in previous chapters by 61x61 grids which is demonstrated in figure (5.1).

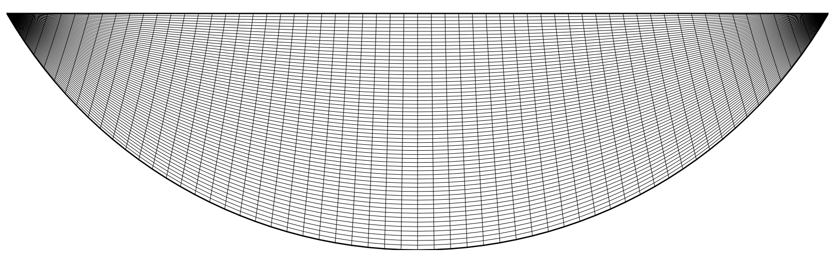

Figure 5.1. 61x61 elliptic grid generated for 1/3 aspect ratio

The test cases are selected such that to provide the diversity among the results. Therefore, one of the test cases is chosen as Re =1000 and Ri =10 which represents moderate Richardson number along with high Reynolds number, while Re =2000 and Ri =2.5 is selected as another test case to investigate high Reynolds number with small Richardson number and the third condition is chosen as an inverse condition of second one, namely it is selected such that to characterize the buoyancy dominated flow regime with small Reynolds number and large Richardson number, Re =400 and Ri =62.5. Stream function patterns and temperature fields for each flow condition are given in proceeding figures in terms of streamlines and isotherms, respectively. In order to have a quantitative comparison the minima and maxima of stream functions and temperature values are provided for each compared case.

**Streamlines** **Isotherms**

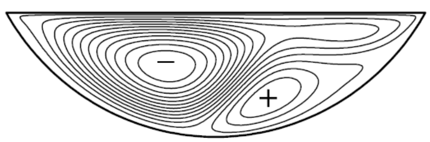


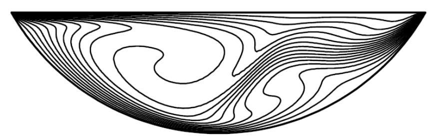

$\psi_{Min} = -\ 0.080612$ $T_{Min} = 0$

$\psi_{\max} = 0.0209513$ $T_{Max} = 1$

**(a)**

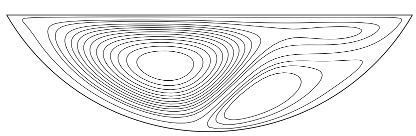

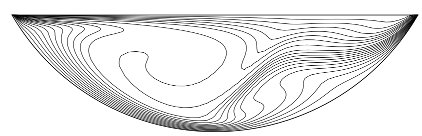

$\psi_{Min} = -\ 0.0814965$ $T_{Min} = 0$

$\psi_{\max} = 0.0190141$ $T_{Max} = 1$

**(b)**

Figure 5.2. Comparison of the streamline and isotherm values at Re = 1000 and Ri = 10 obtained by (a) present numerical method (b) previous study [20]

**Streamlines** **Isotherms**

$\psi_{Min}$ = - 0.0656013 $T_{Min}$ =0

$\psi_{\max} = 0$ $T_{Max}$ =1

**(a)**

$\psi_{Min}$ = - 0.0651572 $T_{Min}$ =0

$\psi_{\max} = 0$ $T_{Max}$ =1

**(b)**

Figure 5.3. Comparison of the streamline and isotherm values at Re = 2000 and Ri = 2.5 obtained by (a) present numerical method (b) previous study [19]

**Streamlines** **Isotherms**

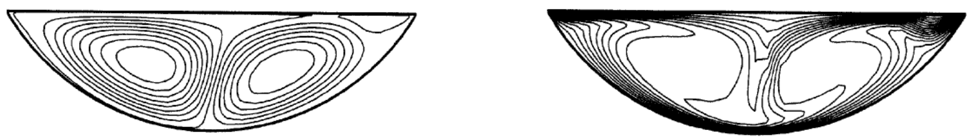

$\psi_{Min}$ = - 0.163595 $T_{Min}$ =0

$\psi_{\max}$ = 0.122976 $T_{Max}$ =1

**(a)**

$\psi_{Min}$ = - 0.16955 $T_{Min}$ =0

$\psi_{\max}$ = 0.122861 $T_{Max}$ =1

**(b)**

Figure 5.4. Comparison of the streamline and isotherm values at Re = 400 and Ri = 62.5 obtained by (a) present numerical method (b) previous study [19]

# 6. RESULTS AND DISCUSSION

Numerical investigations have been conducted to study the combined effects of buoyancy and inertia on heat transfer and flow characteristic for mixed convection flow inside the lid driven arc shape cavities of $1/2$ and $2/3$ aspect ratios. The computational domain is discretized by 81x81 equi-spaced grids for flow regimes with small to moderate values of Reynolds and Richardson numbers and it is discretized by 101x101 equi-spaced grids for flows which are induced by higher values of Reynolds and Richardson numbers. Beyond a grid size of 81x81 grid independent results are achieved. However for large Reynolds number values numerical instabilities are observed for grid size 81x81 and to overcome this instability higher resolution is adapted for these flows.

Reynolds and Richardson numbers are the controlling parameters for fluid flow and convection. Reynolds numbers 200, 400, 800 and 1500 are considered along with Richardson numbers 0.01, 0.1, 1, 2.5, 5, 10, 25 and 100. In order to concentrate on buoyancy and inertia effects Prandtl number is fixed and assigned to be 0.71.

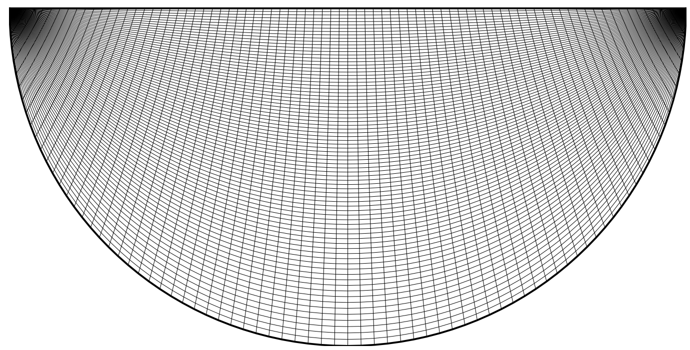

**(a)**

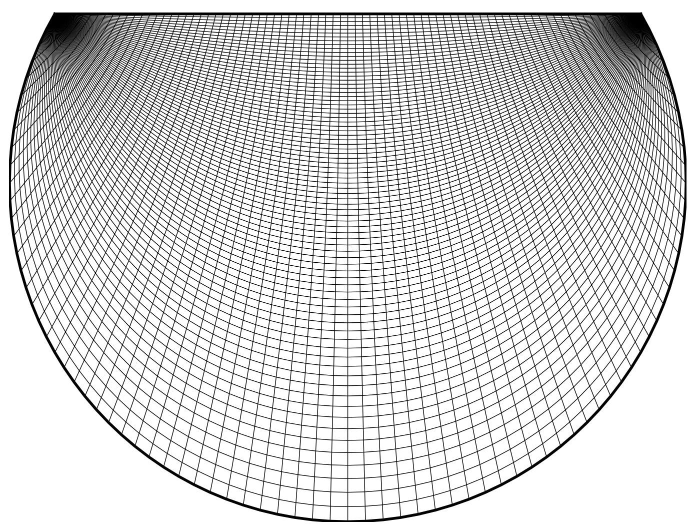

**(b)**

Figure 6.1. 81x81 Elliptic grid generated for (a) $1/2$ aspect ratio, (b) $2/3$ aspect ratio

### 6.1. Streamlines and Isotherms

In figures (6.2), (6.4) and (6.6) the effects of inertia and buoyancy forces on flow patterns and thermal fields for $2/3$ aspect ratio cavity are investigated. Reynolds numbers 200, 400 and 800 are demonstrated in these figures for several Richardson numbers in the range of 0.01< Ri <100. Isotherm values are given at the left and streamlines are represented at the right part of the pages. For negligible Richardson numbers only a shear driven clockwise vortex is observed where the vortex core is located toward the right side of the cavity center and it gets closer to the center when Richardson number reaches unity. On the other hand, increasing the Richardson number which is the measure for the buoyancy effect, results in the formation of another vortex at the lower part of the main clockwise vortex and it is driven in counter-clockwise direction. After the formation of buoyancy induced vortex at the lower part, the shear driven vortex core moves to the upper left region of the cavity and it gets smaller as the buoyant force achieves the higher values.

Again in figures (6.2), (6.4) and (6.6) at small Richardson numbers, shear driven vortex motion produces an extended convection region near the top right corner and it is obviously seen that this region gets smaller and vanishes as Richardson number gets closer to moderate values. Formation of buoyancy induced vortex at the bottom leads to the growth of new convection regions that emerge at the center of the lid and near the bottom right corner. The extensions of these regions are elongated by increasing the Richardson number. Indeed, isotherm lines reveal these buoyancy and inertia related formations. Particularly when Richardson number reaches close to the value of 2.5 the isotherm lines starts to separate in two parts of almost equal strength but different flow directions. Especially in figure (6.2) where Reynolds number is at relatively low value, the formation of two eddies of almost equal sizes at Richardson number of 2.5 demonstrates the balance between inertia and buoyancy forces. When Richardson number is around 5 the buoyancy induced vortex pushes the inertia induced vortex to the top left region and due to the shear force of the lid the prolongation is formed on the region adjacent the lid. Furthermore, in buoyancy dominated flows where Richardson number is above 5 the counter clockwise vortex starts getting bigger and finally the main shear driven vortex occupies just a small region near the top left corner of the cavity. However, a small secondary shear driven vortex appears at the top right region which is formed within the prolongation of the main shear driven vortex and it vanishes as Richardson number attains larger quantities.

Another crucial observation that can be made by isotherm lines is the heat transfer performance and it can be clarified by observing the temperature gradients adjacent the lid and the stationary wall. For small Richardson values this temperature gradient occurs near the bottom right corner and the top left corner at 2/3 aspect ratio cavities. However as Richardson number becomes larger, temperature gradient near the left corner of the stationary wall together with the temperature gradients at the two corners of the moving lid become denser which indicates higher heat transfer rate in these regions.

The similar effects can be summarized based on the results obtained for 1/2 aspect ratio cavities in figures (6.3), (6.5) and (6.7), and the comparison can be stated by considering aspect ratio effects on isotherms and streamlines. Again for small Richardson numbers the center of the shear driven eddy is observed at the right side of the cavity center and gradually by increasing the Richardson number it moves to the left, until it reaches almost to the center of the enclosure when the Richardson number reaches 2.5. It is crucial to mention that, in 2/3 aspect ratio cavity flow the vortex core set near the centerline when Richardson number is around 1. There is no doubt that the delay in vortex core placement at the center of the cavity from Richardson number of 1 to 2.5 is only due to the aspect ratio effect. Inertia and buoyancy forces' strengths on flow and thermal fields are primarily affected by changing the aspect ratio. For this reason reducing the aspect ratio from 2/3 to 1/2 causes less buoyant force effects and higher inertia force effects. Inertia induced vortex produces an extended convection region on the right side of the lid and it gets larger till Richardson number attains the value of 2.5. After Richardson number of 2.5 the convection region generated by the shear vortex motion gets smaller and gradually this region turns into the high dense heat transfer area. On the other hand, at larger Richardson numbers the extended convection regions develop at right and left sides of the wall and almost at center of the moving lid. Moreover, for buoyancy dominated flows the high dense temperature areas are found to be placed nearby the corners at the top and almost at the center of the stationary wall.

In 1/2 aspect ratio cavity when the Richardson number attains values higher than 5 the buoyancy effects start dominating the flow regimes and thermal fields. Unlike the vortex formation of 2/3 aspect ratio cavity where the buoyancy induced eddy pushes the inertia induced eddy toward the left corner, in 1/2 aspect ratio, by increasing the Richardson number, buoyancy induced eddy pulls the inertia induced eddy toward the centerline of the cavity and finally when the Richardson number reaches its largest value, two vortices are placed at the left and right regions symmetrically and their strengths are almost equalized. Shear driven clockwise vortex flows at the left and the buoyancy induced counterclockwise vortex circulates at the right region.

In figures (6.7) and (6.9) negligible Richardson number 0.01 in first lines, represent inertia dominant flows in 1/2 aspect ratio cavity where Reynolds numbers are 800 and 1500, respectively. Different than the previous cases, in 1/2 aspect ratio cavity, beside the primary eddy generated due to the shear force exerted by the lid, a second inertia induced vortex formation is observed near the left corner in small Richardson number values. Moreover, the size and strength of this secondary inertial eddy strongly depends on the value of Reynolds number. As the flow becomes inertial dominant a second vortex occupies more space within the cavity. This can be observed when Reynolds number increases from 800 to 1500. The second inertial eddy which is formed in Richardson number 0.01 in figure (6.9) is bigger than that in figure (6.7) and even it does not disappear when Richardson number reaches 0.1, yet only gets smaller. However, for the same Richardson number, in figure (6.7) second inertial vortex is not noticed any longer.

Figure (6.8) demonstrates the streamlines and isotherms for 2/3 aspect ratio cavity where Reynolds number is 1500. Unlike the 1/2 aspect ratio case, secondary shear induced eddy is not observed in small Richardson numbers for the same Reynolds number. Nonetheless, another interesting future in 2/3 aspect ratio is observed which is the structure of streamline and isotherm patterns formed in Richardson number 1. It can be observed that, unlike the other cases buoyancy induced eddy is already developed and even it attained strong streamline values that pushes the shear induced vortex to the right corner. Furthermore, it is noticeable that, unlike the other streamline patterns, the shear driven vortex is pushed toward the right corner by the buoyancy induced eddy instead of the left corner. By increasing the Richardson number further than 1 almost the same patterns are observed in comparison with the smaller Reynolds number flows.

Figure (6.10) is given to emphasize the consequences of variation of Reynolds number for the fixed Richardson number and aspect ratio when both inertia and buoyancy induced eddies are formed together. Richardson number is fixed to 2.5 and Reynolds number varies from 200 till 1500. This figure is important due to the change in vortex structures within the cavity. The isotherms and streamlines are plotted in the same order as previously specified. As mentioned before, at Richardson number 2.5 and Reynolds number 200 the inertial vortex driven by the moving lid is deformed due to the opposing action of buoyancy induced vortex generated by the stationary wall. Based on the streamline figures it can be stated that, increasing the Reynolds number from 200 to 400 causes a smaller shear driven vortex and a larger buoyancy induced vortex. Although the ratio of inertia over the buoyancy gets larger, the vortex structure behaves on opposite way, such that the inertial vortex gets smaller while the buoyant related vortex gets larger. It may be attributed to horizontal application of the shear force generated by the motion of the lid. Further increasing of Reynolds number from 400 to 800 results in formation of two secondary eddies of almost equal strength inside the upper primary eddy driven by the moving lid and when Reynolds number reaches 1500 the downstream eddy within the shear driven vortex vanishes and the upstream eddy becomes larger. For the fixed Richardson number 2.5, the strongest inertial vortex motion is observed at Reynolds number of 200 and the weakest inertial vortex is found at Reynolds number of 800, whereas the strongest buoyancy induced vortex motion is obtained at Reynolds number of 1500 and the weakest buoyancy induced vortex is found at Reynolds number of 200.

Tables (6.1) and (6.2) provide minimum and maximum values of streamlines for a quantitative comparison of 2/3 and 1/2 aspect ratio cases, respectively. At inertial dominated flows the strength of inertia induced eddy is larger in 2/3 aspect ratio cavity when compared with 1/2 aspect ratio cases. On the other hand, at buoyancy dominated flows the strength of inertia induced eddy is larger while the strength of buoyancy induced eddy is smaller in 1/2 aspect ratio cavity when compared with 2/3 aspect ratio cavity results. For all of the flow and thermal conditions the isotherm values ranges within 0 and

1. That is why minimum and maximum values of isotherms for each case are not mentioned in tables separately.

In figures (6.12)-(6.19) the transient variations of stream functions and temperature values at a specific point for various Richardson numbers are demonstrated to clarify the required time steps to reach the steady solution. Another reason of providing these figures is to observe periodic patterns, if they exist. When periodic flow pattern occurs the transient variation of stream function and temperature exhibit different nature compared to a steady case. According to Chen and Cheng [19] the periodicity is detected in 1/3 aspect ratio cavity when Reynolds number is 200 and Richardson number is within the range of 12.5 and 50. Nevertheless, in this research for the specified range of Richardson number and at Reynolds number of 200 all of the obtained results are steady. Indeed, in this study no periodicity is observed for the investigated parameters. Chen and Cheng claim that when buoyancy and inertia forces are of approximately equal strength can the periodic flow pattern be observed. However based on the examined conditions and results it can be concluded that this assumption is not applicable for 2/3 and 1/2 aspect ratio cavities.

The convergence of the results to steady state is checked by calculating the relative error norm at every $10^3$ time steps. The required time steps for convergence is strongly dependent upon values of Richardson and Reynolds numbers and the convergence can be monitored in figures (6.12)-(6.19). Relative error norm is expressed as

$$REN = \sqrt{\frac{\sum_{i,j} \left(f_{i,j}^{k+1} - f_{i,j}^{k}\right)^2}{\left(f_{i,j}^{k+1}\right)^2}} \,. \qquad (6.1)$$

Effects of aspect ratio on fluid flow and heat transfer is demonstrated in figure (6.11). In shallow cavity with small aspect ratio of 1/6, vortex core is located toward the right corner. Isotherms are almost smooth and the convection region is not generated yet. By increasing the aspect ratio, center of the inertia induced vortex moves toward the center of the cavity and convection region develops at the right side of the lid. When aspect ratio becomes 1/2, fluid circulates almost symmetrically inside the cavity and this symmetry feature is also observed in temperature distribution. Further increase in aspect ratio reveals buoyancy effects more than smaller aspect ratio cavities. Thermal boundary layers are separated due to the convection region which is generated by the buoyancy force and the buoyancy induced eddy is already formed as a result of thermal boundary layer separation and even it is stronger than the shear driven top eddy. Then it can be concluded that the buoyancy effects are stronger and apparent in large aspect ratio flows when compared with smaller aspect ratio ones.

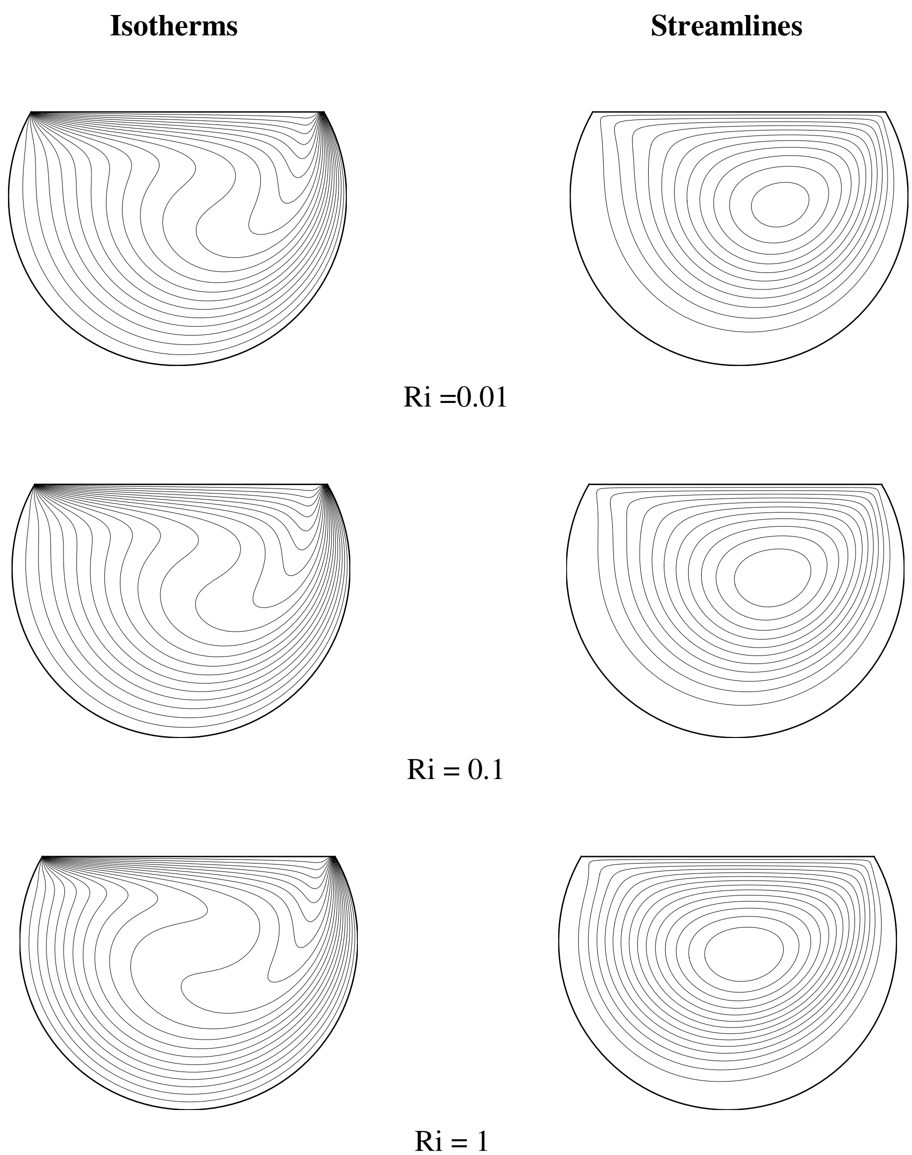


Figure 6.2. Flow patterns and thermal fields for 2/3 aspect ratio cavity at Re=200

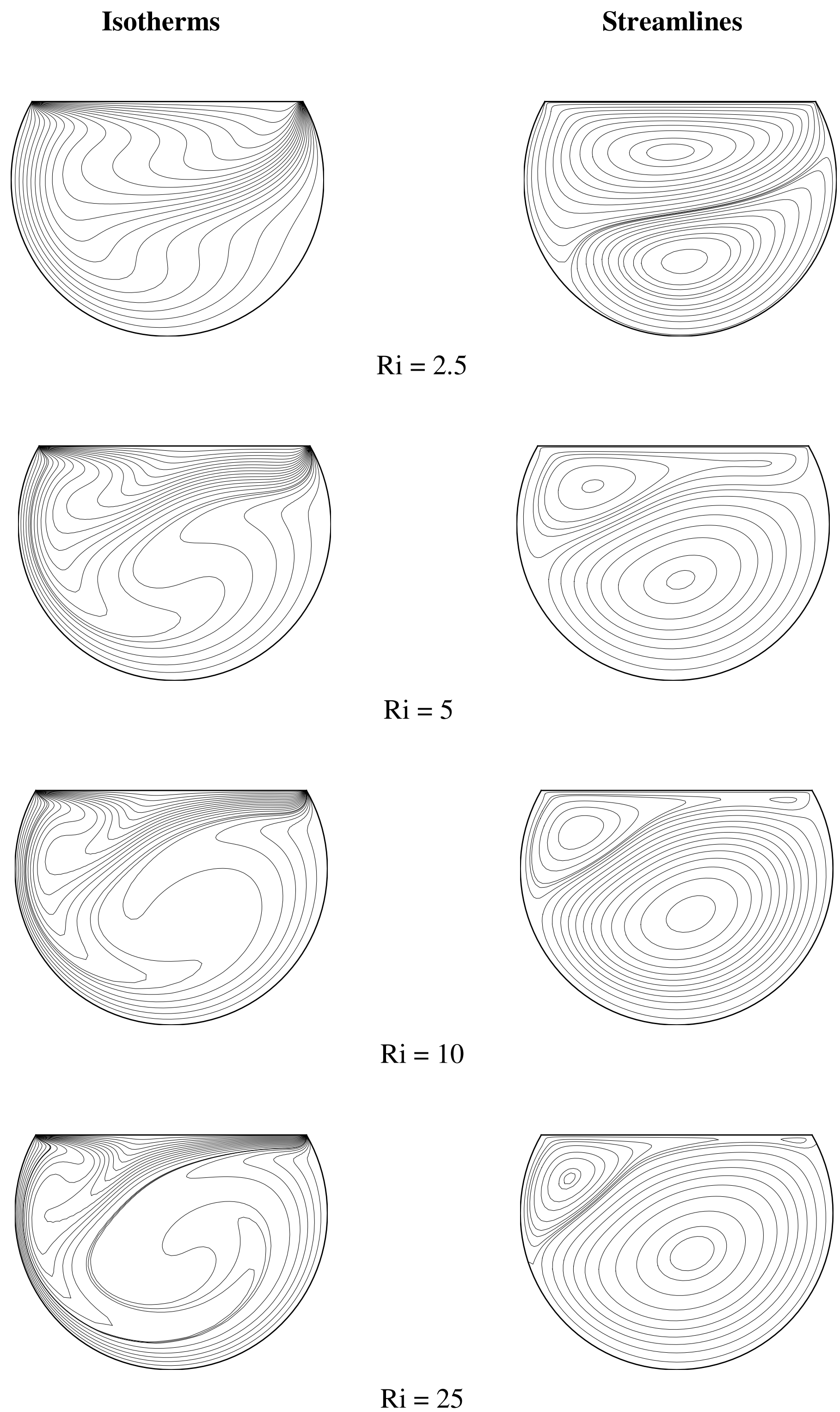


Figure 6.2. (Continued)

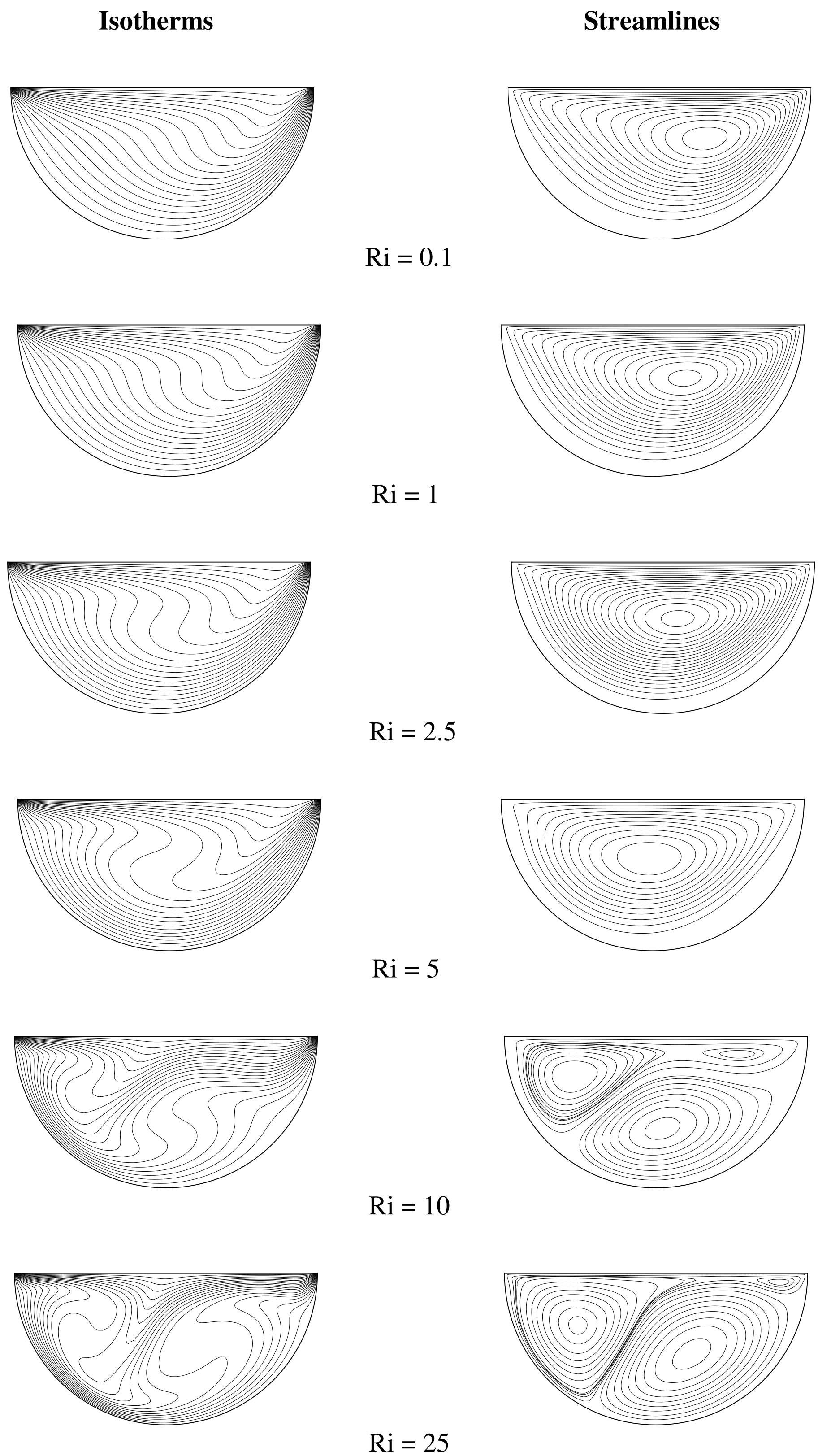


Figure 6.3. Flow patterns and thermal fields for 1/2 aspect ratio cavity at Re=200

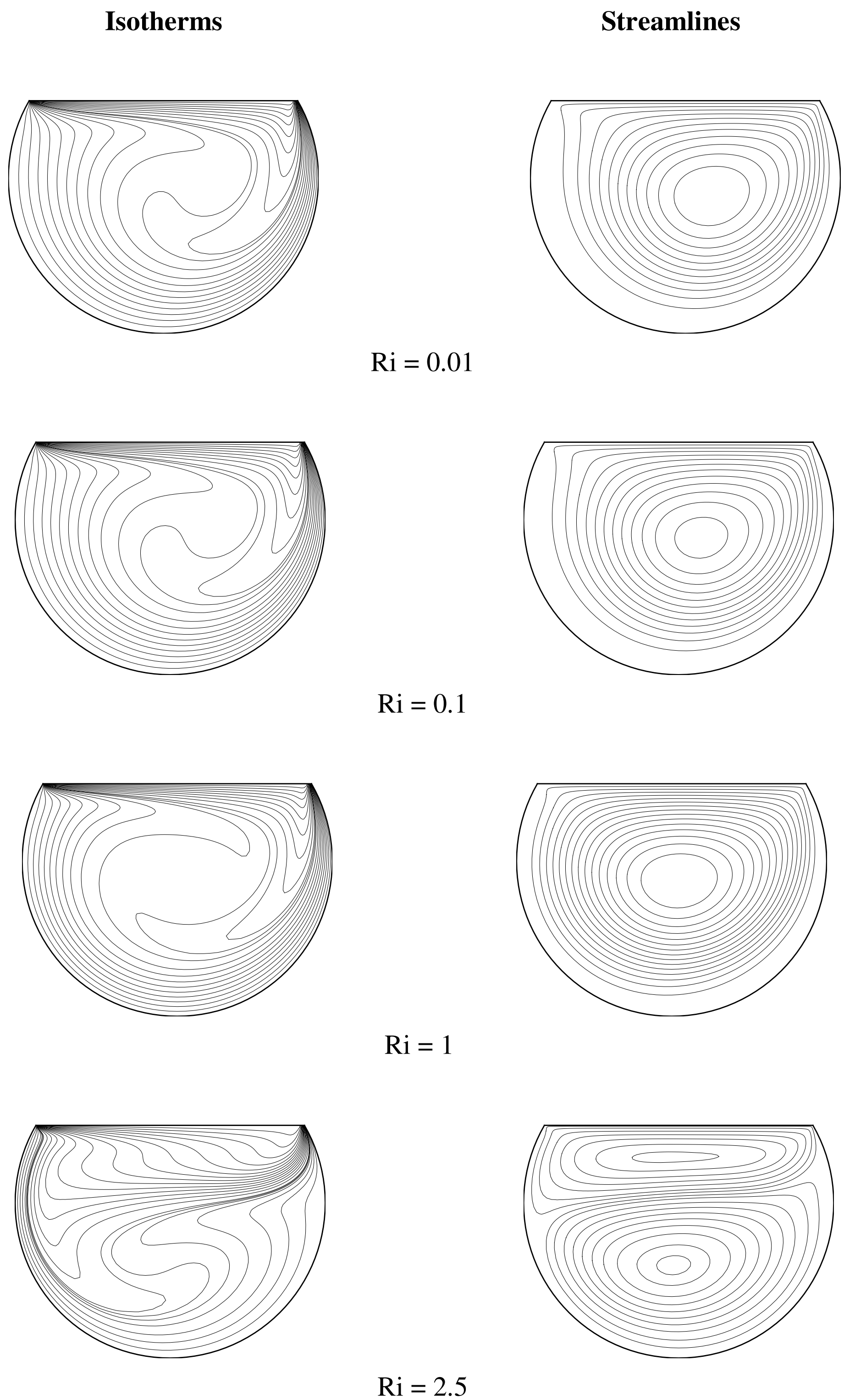


Figure 6.4. Flow patterns and thermal fields for 2/3 aspect ratio cavity at Re=400

**Isotherms** **Streamlines**

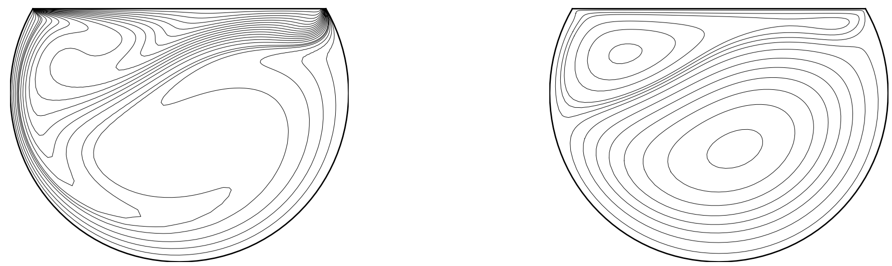

Ri = 5

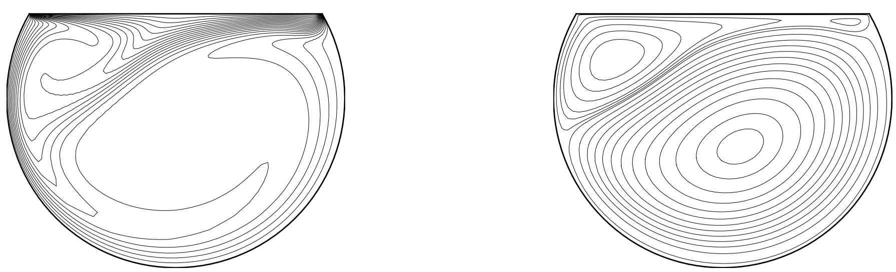

Ri = 10

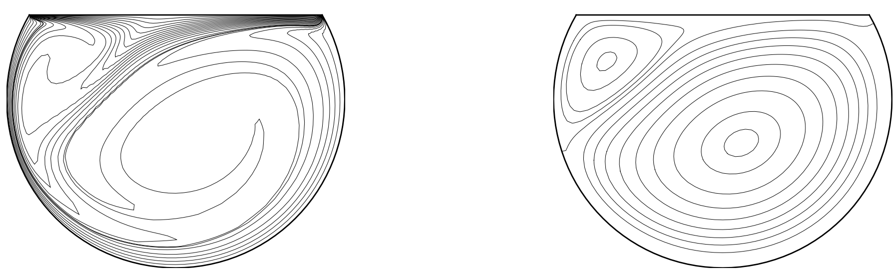

Ri = 25

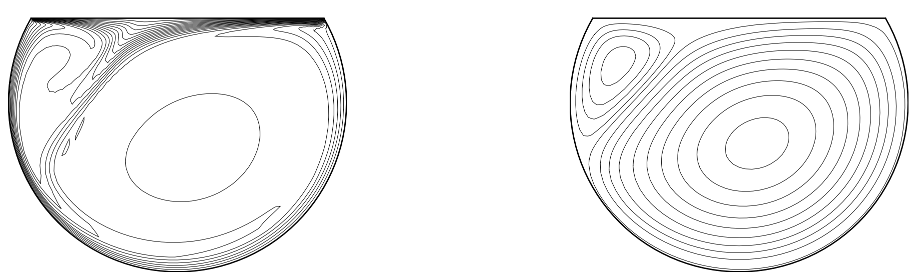

Ri = 100

Figure 6.4. (Continued)

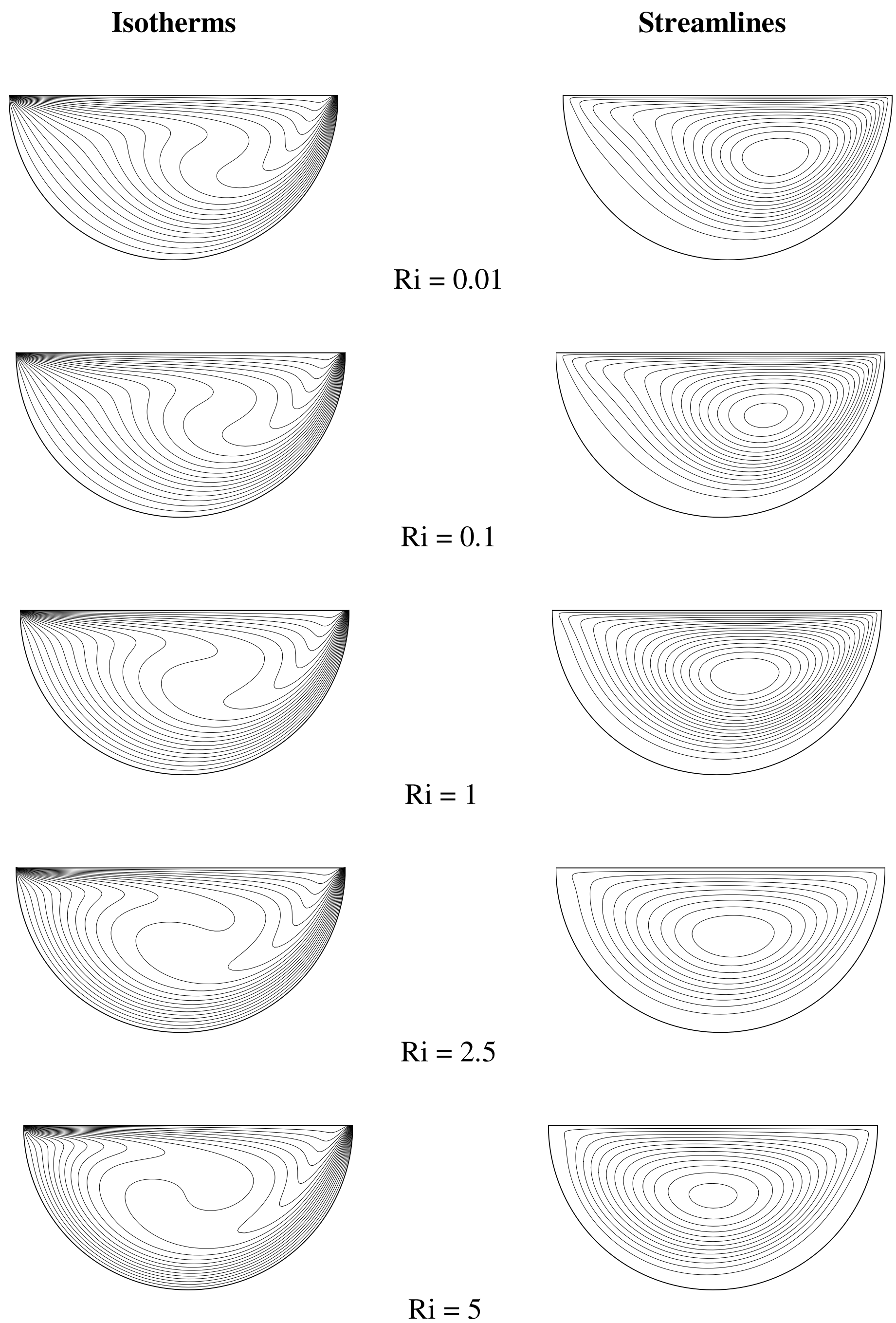


Figure 6.5. Flow patterns and thermal fields for 1/2 aspect ratio cavity at Re=400

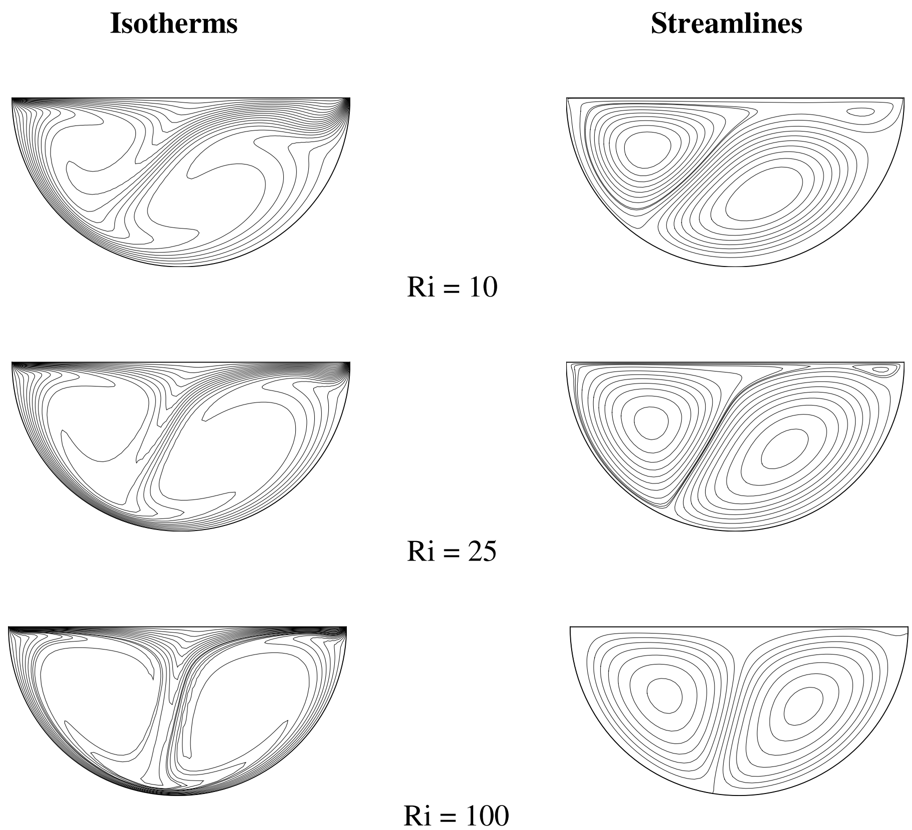


Figure 6.5. (Continued)

**Isotherms** **Streamlines**

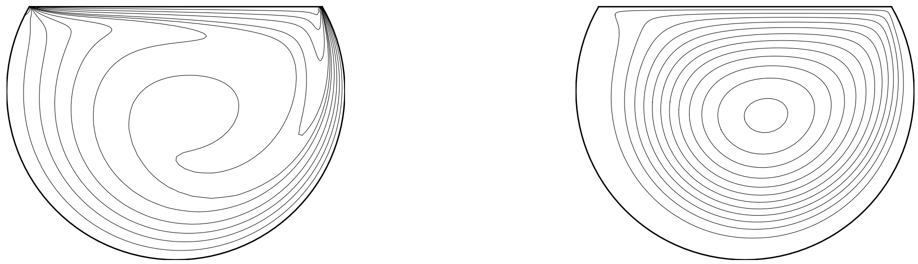

Ri = 0.01

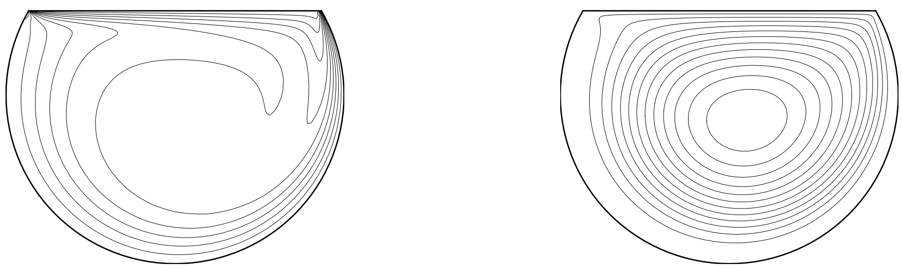

Ri = 0.1

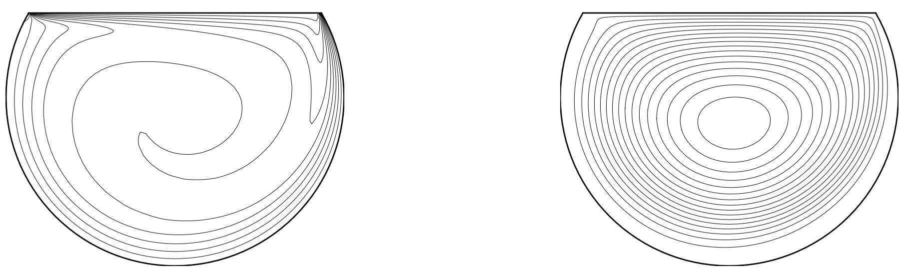

Ri = 1

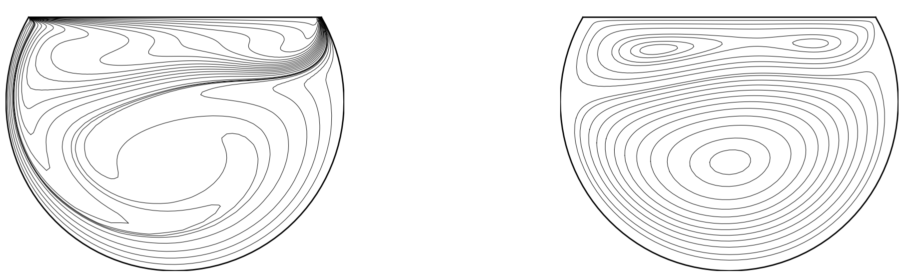

Ri = 2.5

Figure 6.6. Flow patterns and thermal fields for 2/3 aspect ratio cavity at Re=800

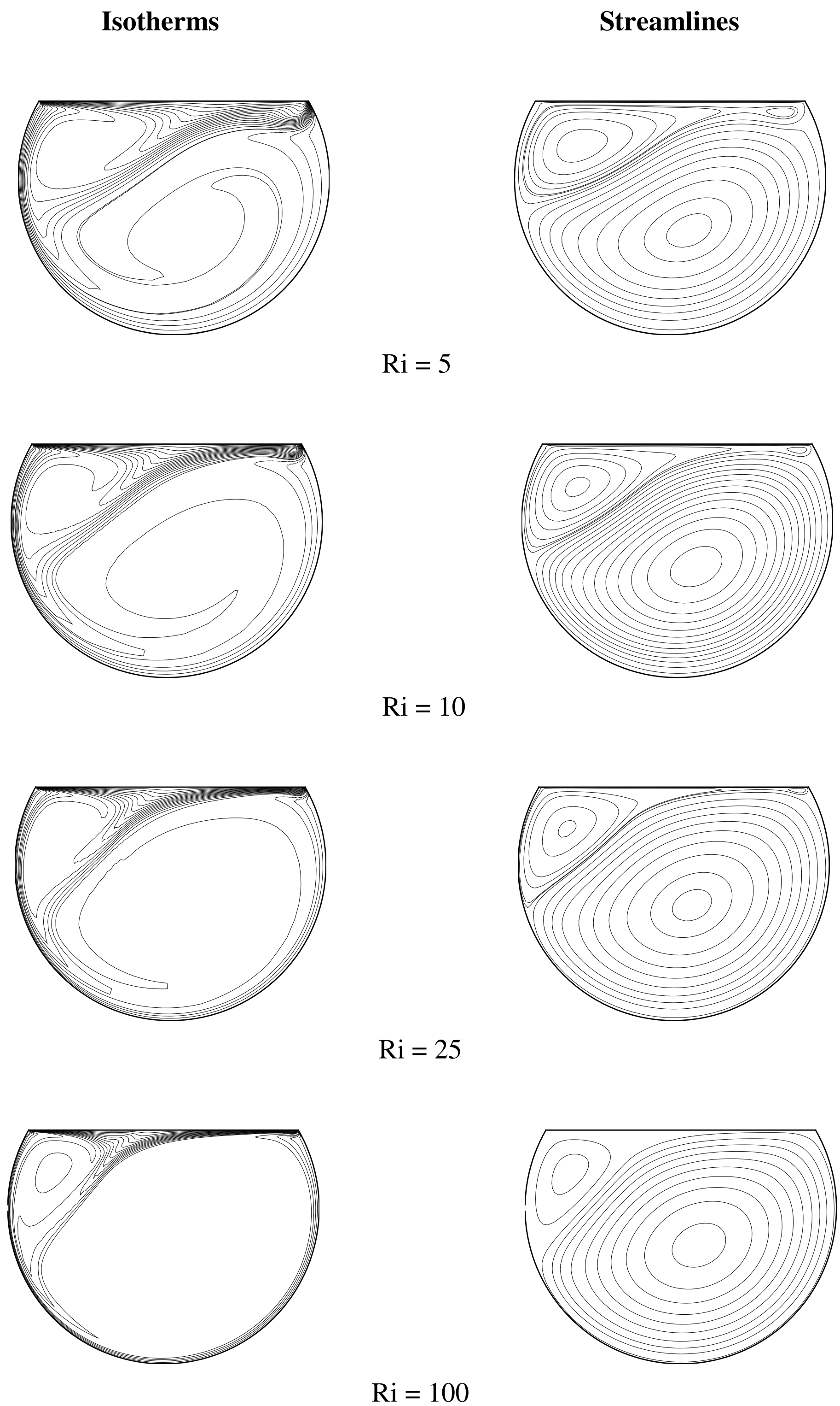


Figure 6.6. (Continued)

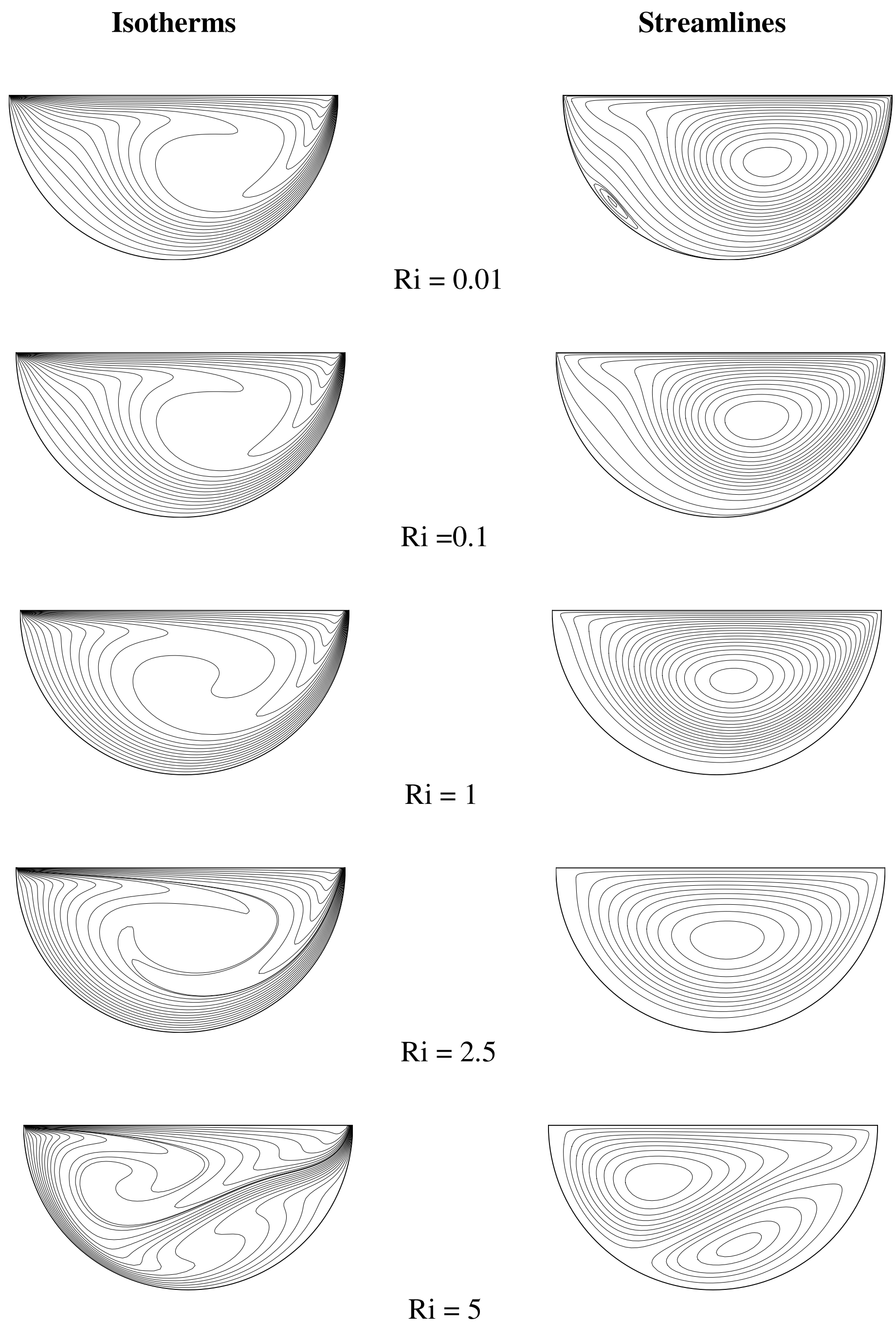


Figure 6.7. Flow patterns and thermal fields for 1/2 aspect ratio cavity at Re=800

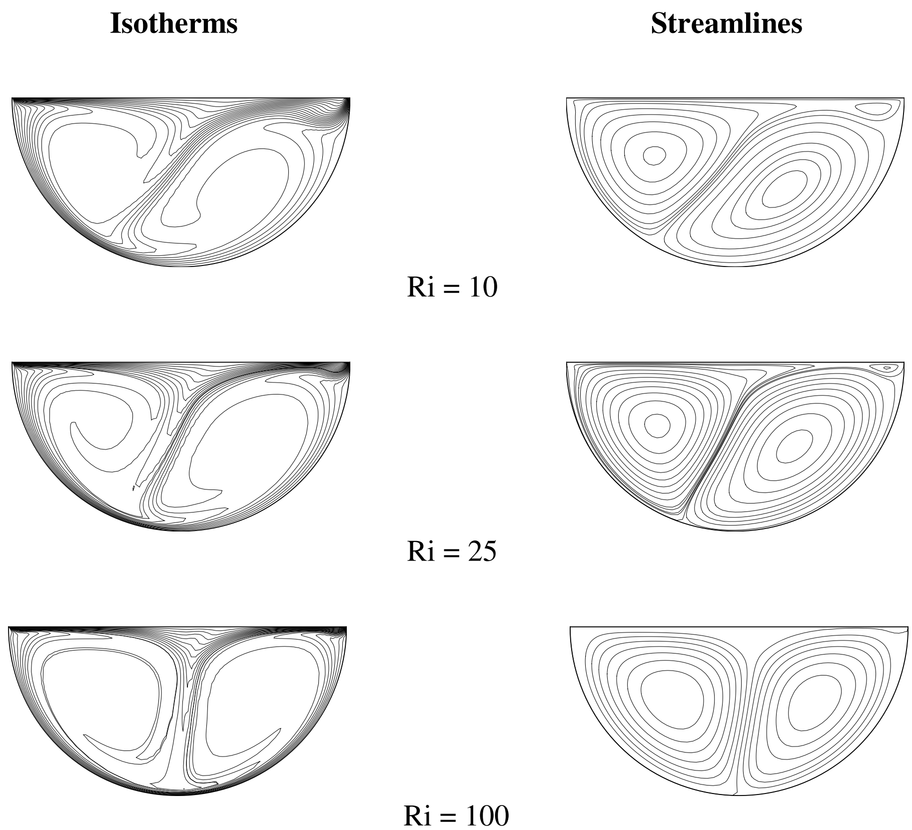


Figure 6.7. (Continued)

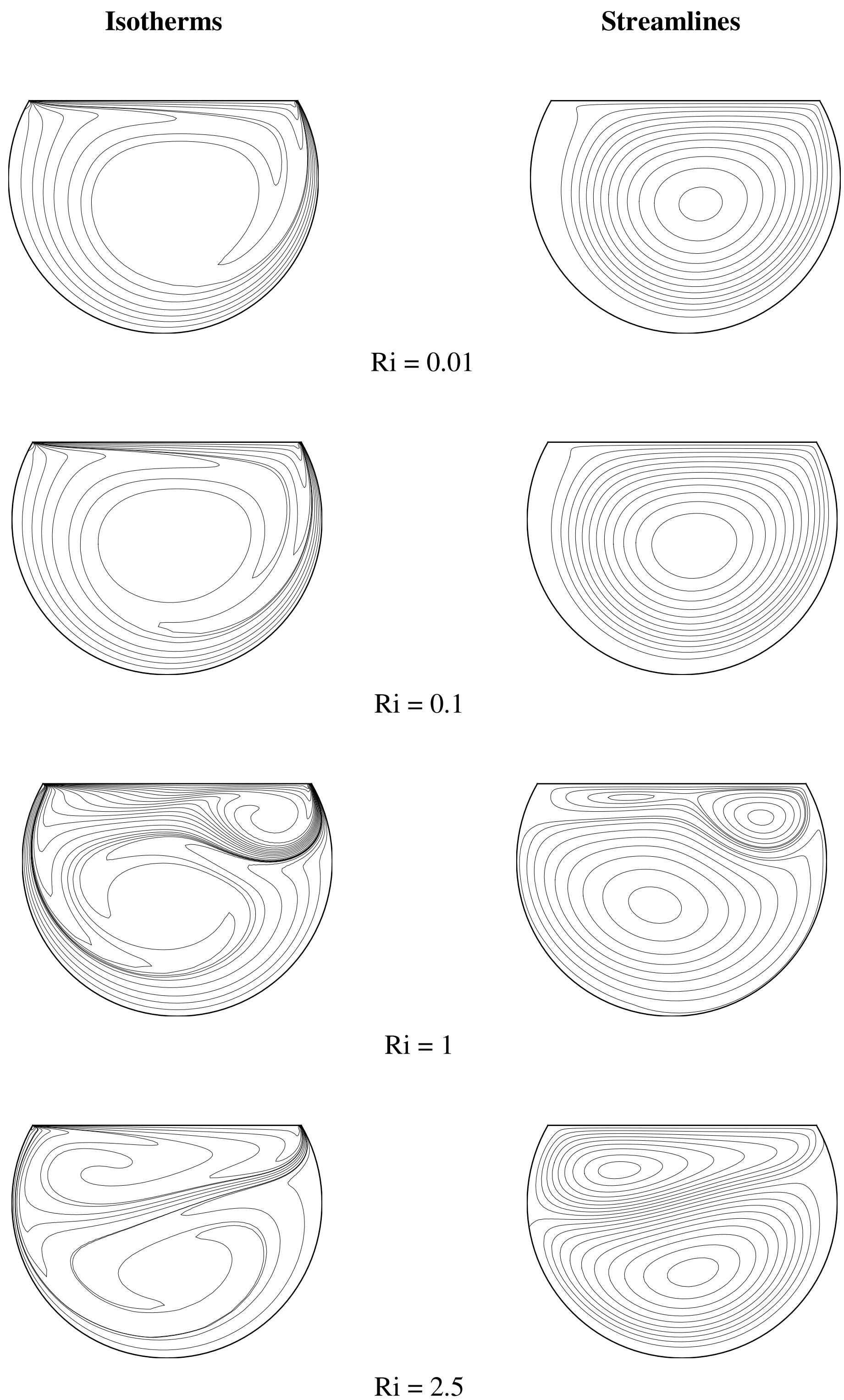


Figure 6.8. Flow patterns and thermal fields for 2/3 aspect ratio cavity at Re=1500

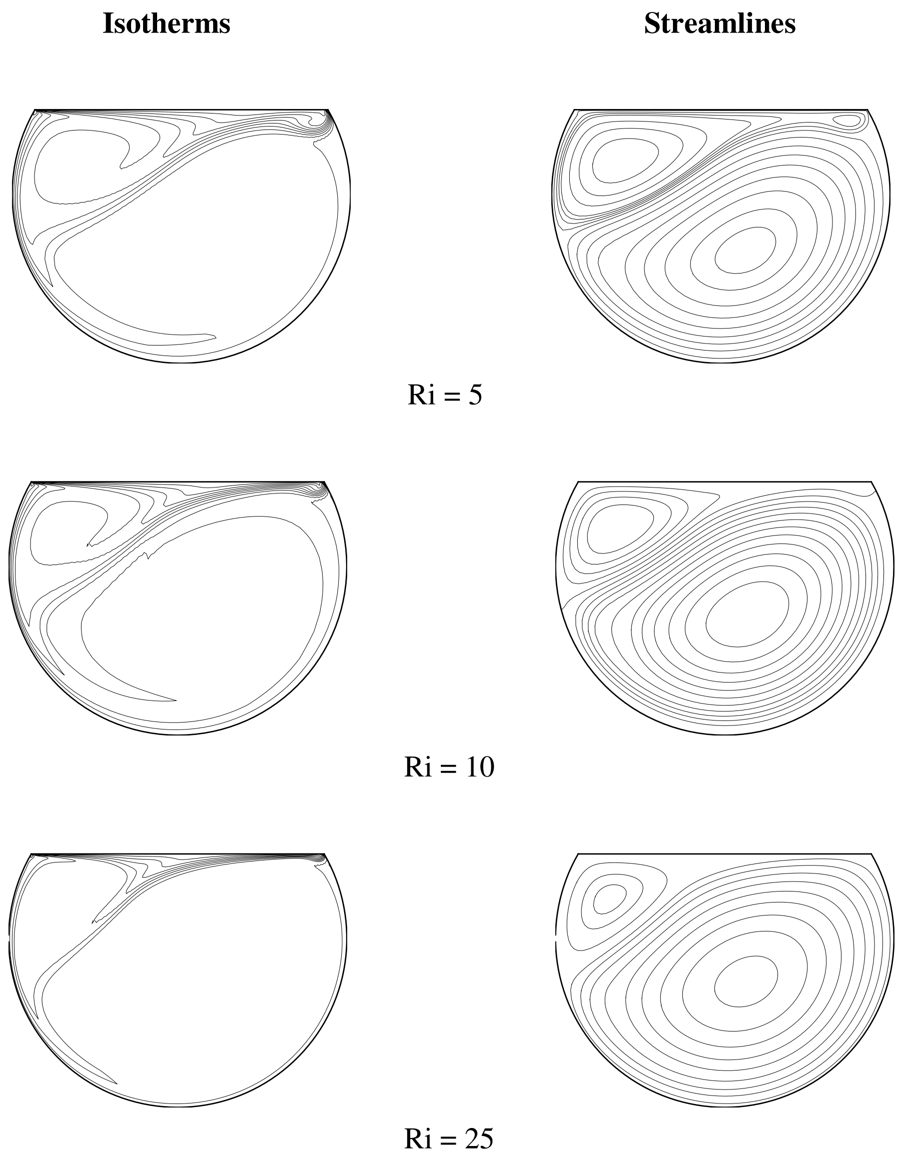


Figure 6.8. (Continued)

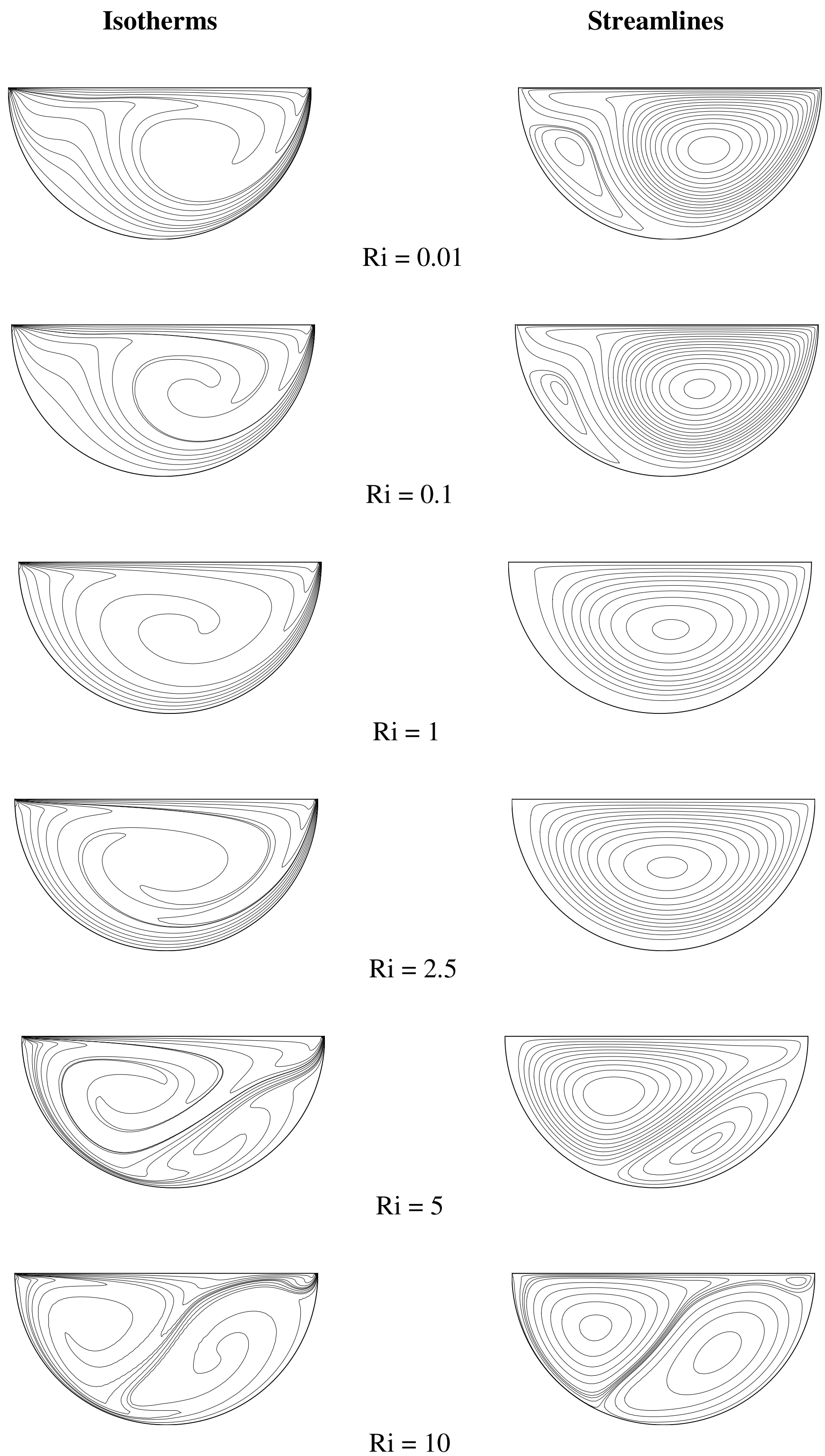


Figure 6.9. Flow patterns and thermal fields for 1/2 aspect ratio cavity at Re=1500

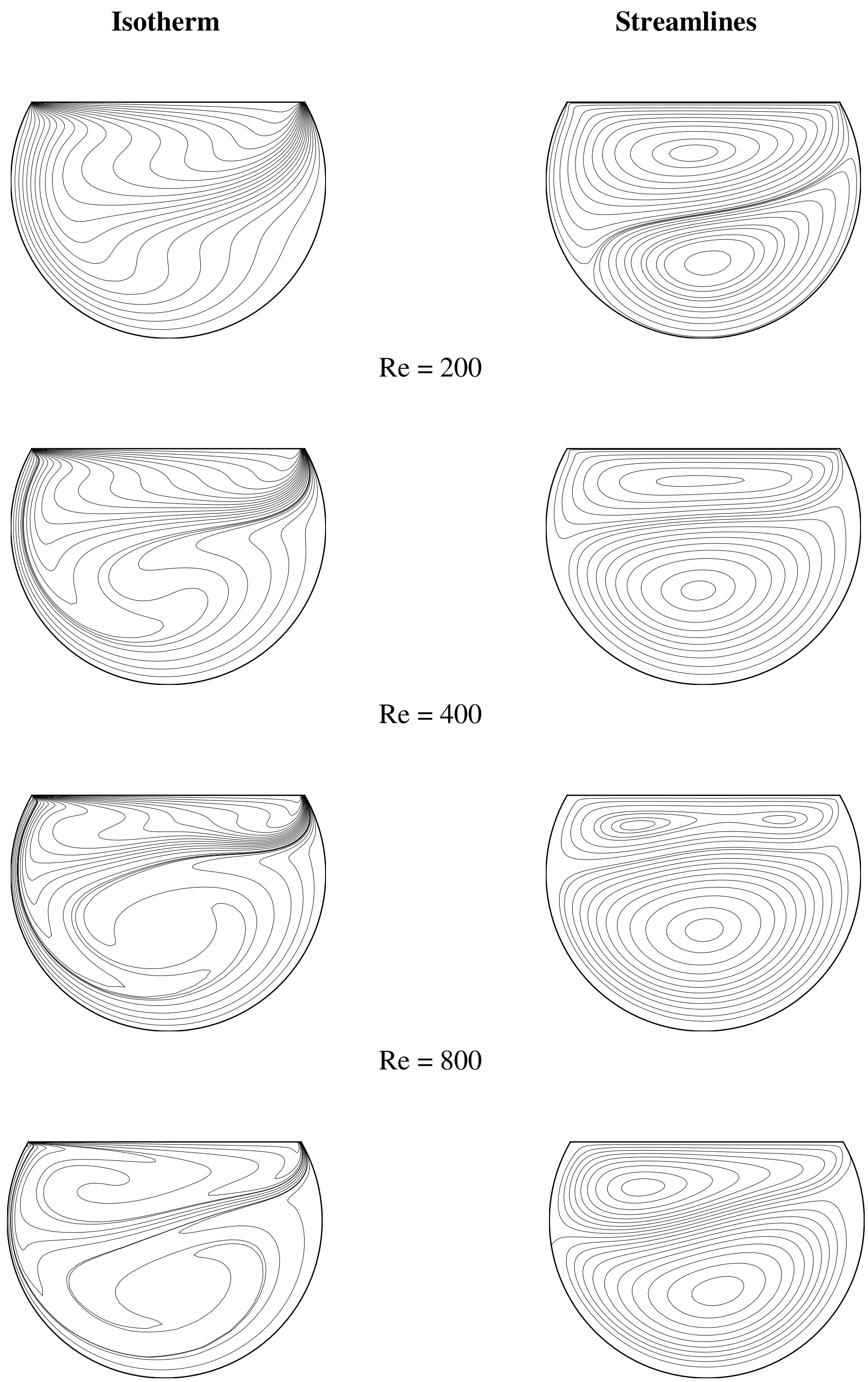


Figure 6.10. Flow patterns and thermal fields for 2/3 aspect ratio cavity at Ri = 2.5

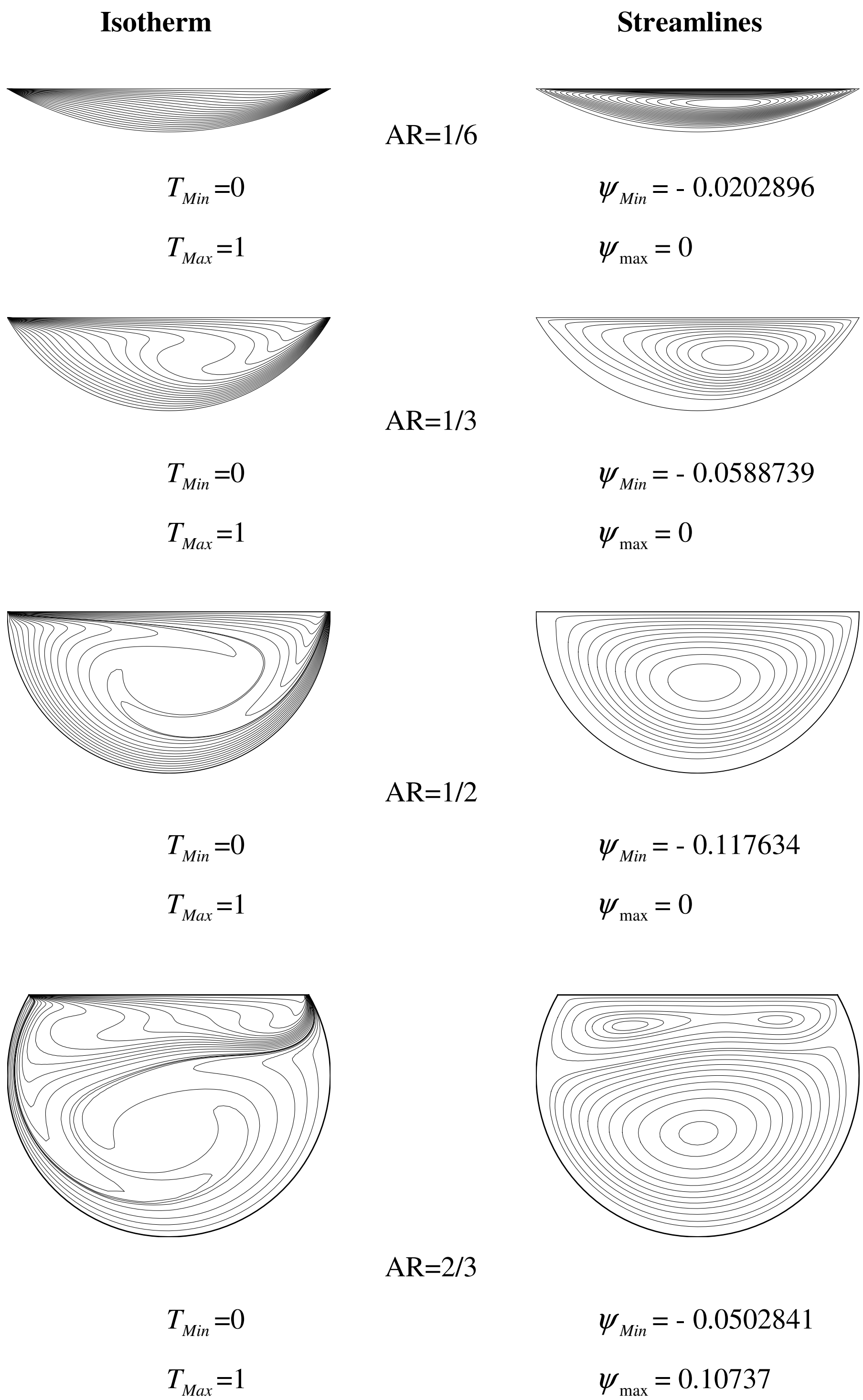


Figure 6.11. Flow patterns and thermal fields for Ri = 2.5 and Re = 800 at different aspect ratios

Table 6.1. Minimum and maximum Streamline values for 2/3 aspect ratio cavity

| Re | *Ri* | $\psi_{\min}$ | $\psi_{\max}$ |
|---|---|---|---|
| 200 | 0.01 | -0.0115164 | 0 |
| | 0.1 | -0.119042 | 0 |
| | 1 | -0.150475 | 0 |
| | 2.5 | -0.0973186 | 0.0501829 |
| | 5 | -0.0803557 | 0.130784 |
| | 10 | -0.0945955 | 0.226915 |
| | 25 | -0.128888 | 0.409977 |
| | | | |
| 400 | 0.01 | -0.119713 | 0 |
| | 0.1 | -0.124799 | 0 |
| | 1 | -0.160928 | 0 |
| | 2.5 | -0.059355 | 0.0870982 |
| | 5 | -0.0837559 | 0.144814 |
| | 10 | -0.0971211 | 0.239022 |
| | 25 | -0.132069 | 0.429054 |
| | 100 | -0.225231 | 0.940456 |
| | | | |
| 800 | 0.01 | -0.122538 | 0 |
| | 0.1 | -0.128772 | 0 |
| | 1 | -0.168277 | 0 |
| | 2.5 | -0.0502841 | 0.10737 |
| | 5 | -0.0907617 | 0.15533 |
| | 10 | -0.102711 | 0.248506 |
| | 25 | -0.132453 | 0.436107 |
| | 100 | -0.234749 | 0.933673 |
| | | | |
| 1500 | 0.01 | -0.122788 | 0 |
| | 0.1 | -0.131093 | 0 |
| | 1 | -0.0614548 | 0.0712648 |
| | 2.5 | -0.0901788 | 0.101854 |
| | 5 | -0.0954714 | 0.160093 |
| | 10 | -0.102727 | 0.237343 |
| | 25 | -0.135307 | 0.417475 |

Table 6.2. Minimum and maximum Streamline values for 1/2 aspect ratio cavity

| Re | $Ri$ | $\psi_{min}$ | $\psi_{max}$ |
|---|---|---|---|
| 200 | 0.1 | -0.0728814 | 0 |
| | 1 | -0.0816241 | 0 |
| | 2.5 | -0.0968641 | 0 |
| | 5 | -0.119081 | 0 |
| | 10 | -0.082022 | 0.0739569 |
| | 25 | -0.15694 | 0.167777 |
| | | | |
| 400 | 0.01 | -0.0760284 | 0 |
| | 0.1 | -0.0775592 | 0 |
| | 1 | -0.0913537 | 0 |
| | 2.5 | -0.109816 | 0 |
| | 5 | -0.133973 | 0 |
| | 10 | -0.100833 | 0.0923461 |
| | 25 | -0.169767 | 0.168955 |
| | 100 | -0.369456 | 0.35819 |
| | | | |
| 800 | 0.01 | -0.0783889 | 0 |
| | 0.1 | -0.0807151 | 0 |
| | 1 | -0.097896 | 0 |
| | 2.5 | -0.117634 | 0 |
| | 5 | -0.0996522 | 0.0387173 |
| | 10 | -0.11819 | 0.0921667 |
| | 25 | -0.1849772 | 0.166587 |
| | 100 | -0.404006 | 0.340149 |
| | | | |
| 1500 | 0.01 | -0.0782496 | 0.00218801 |
| | 0.1 | -0.0817088 | 0.0005701 |
| | 1 | -0.102065 | 0 |
| | 2.5 | -0.122717 | 0 |
| | 5 | -0.121308 | 0.0351329 |
| | 10 | -0.125954 | 0.0870923 |
| | 25 | -0.21268 | 0.172194 |

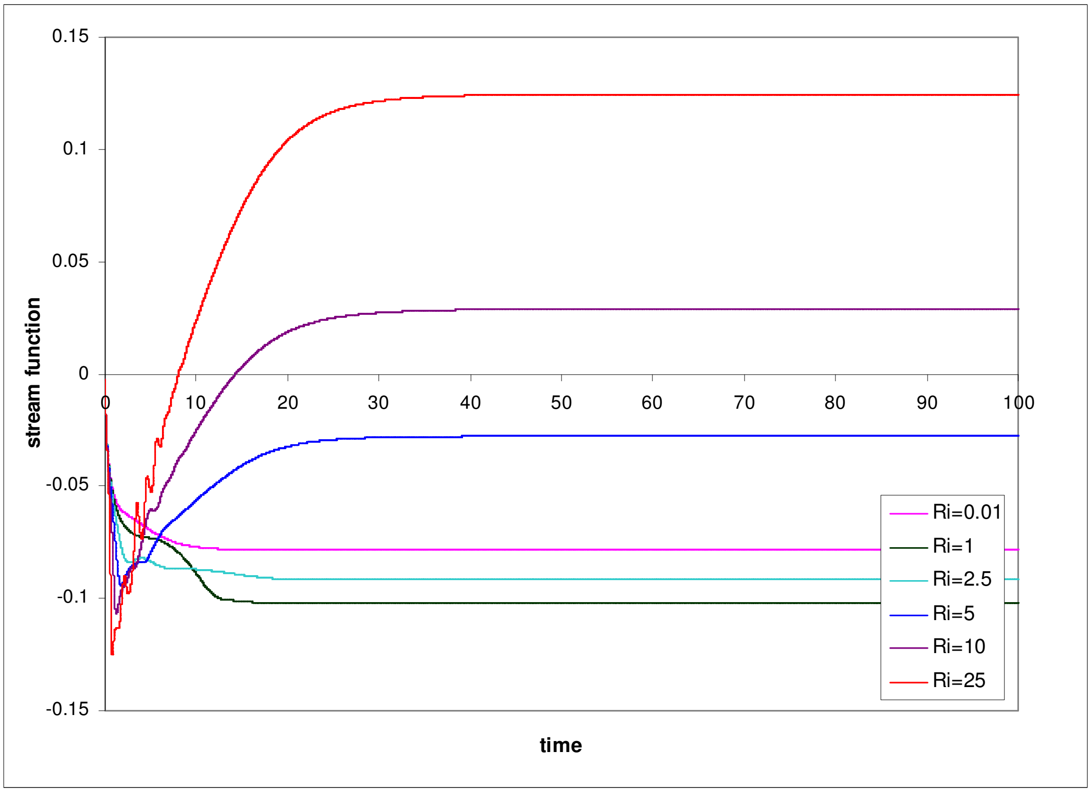


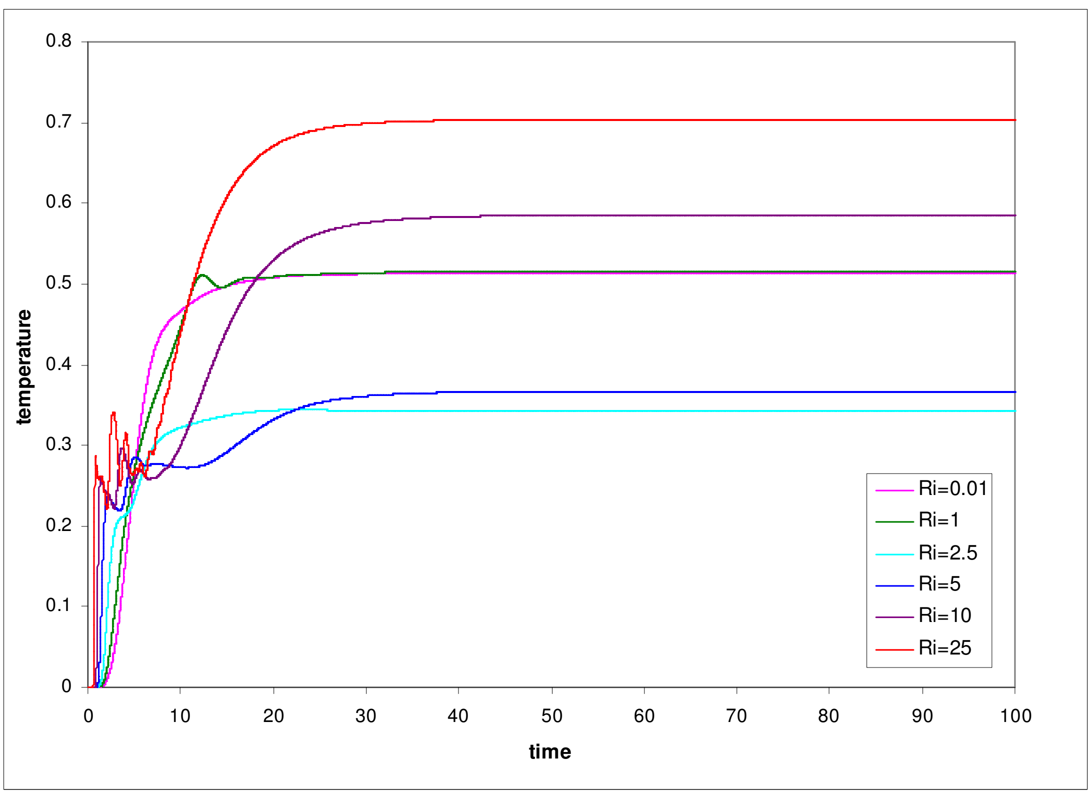


Figure 6.12. Transient variation in stream function and temperature values for various Ri numbers at a point which is located in (0.5,0.65), for Re = 200 and 2/3 aspect ratio

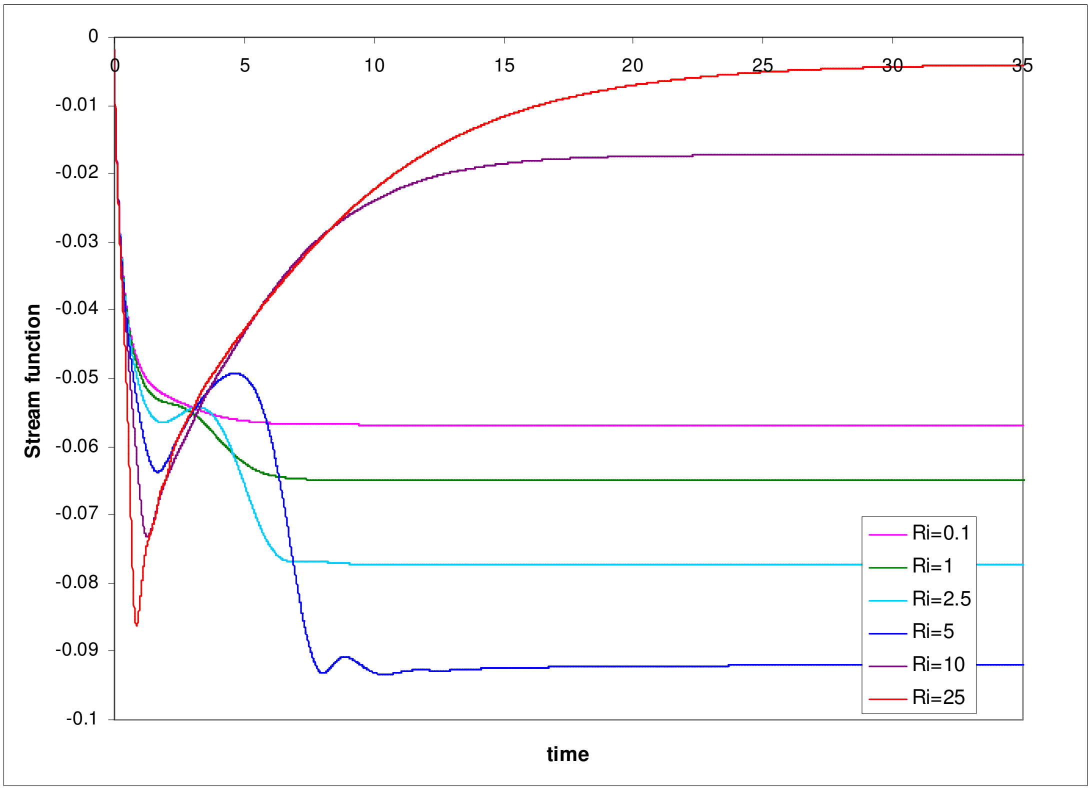


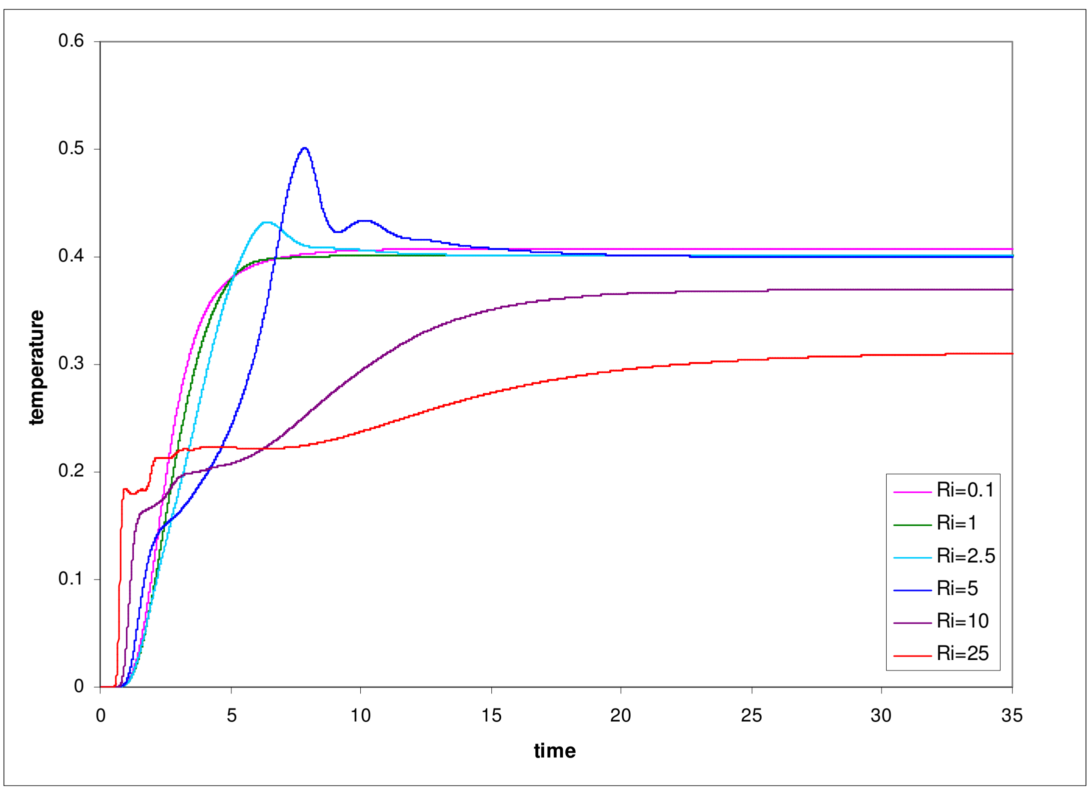


Figure 6.13. Transient variation in stream function and temperature values for various Ri numbers at a point which is located in (0.5,0.375), for Re =200 and 1/2 aspect ratio

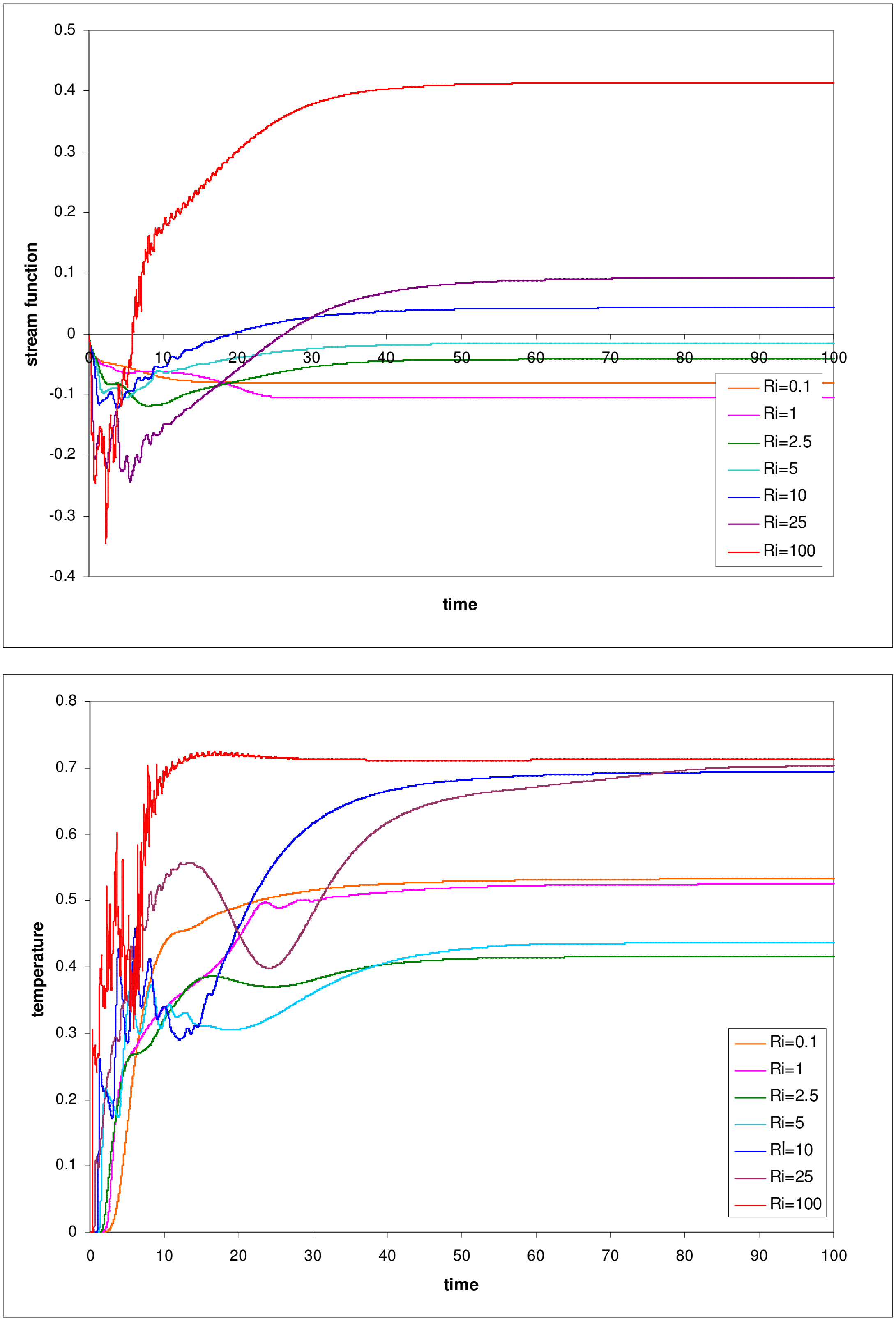


Figure 6.14. Transient variation in stream function and temperature values for various Ri numbers at a point which is located in (0.5,0.65), for Re = 400 and 2/3 aspect ratio

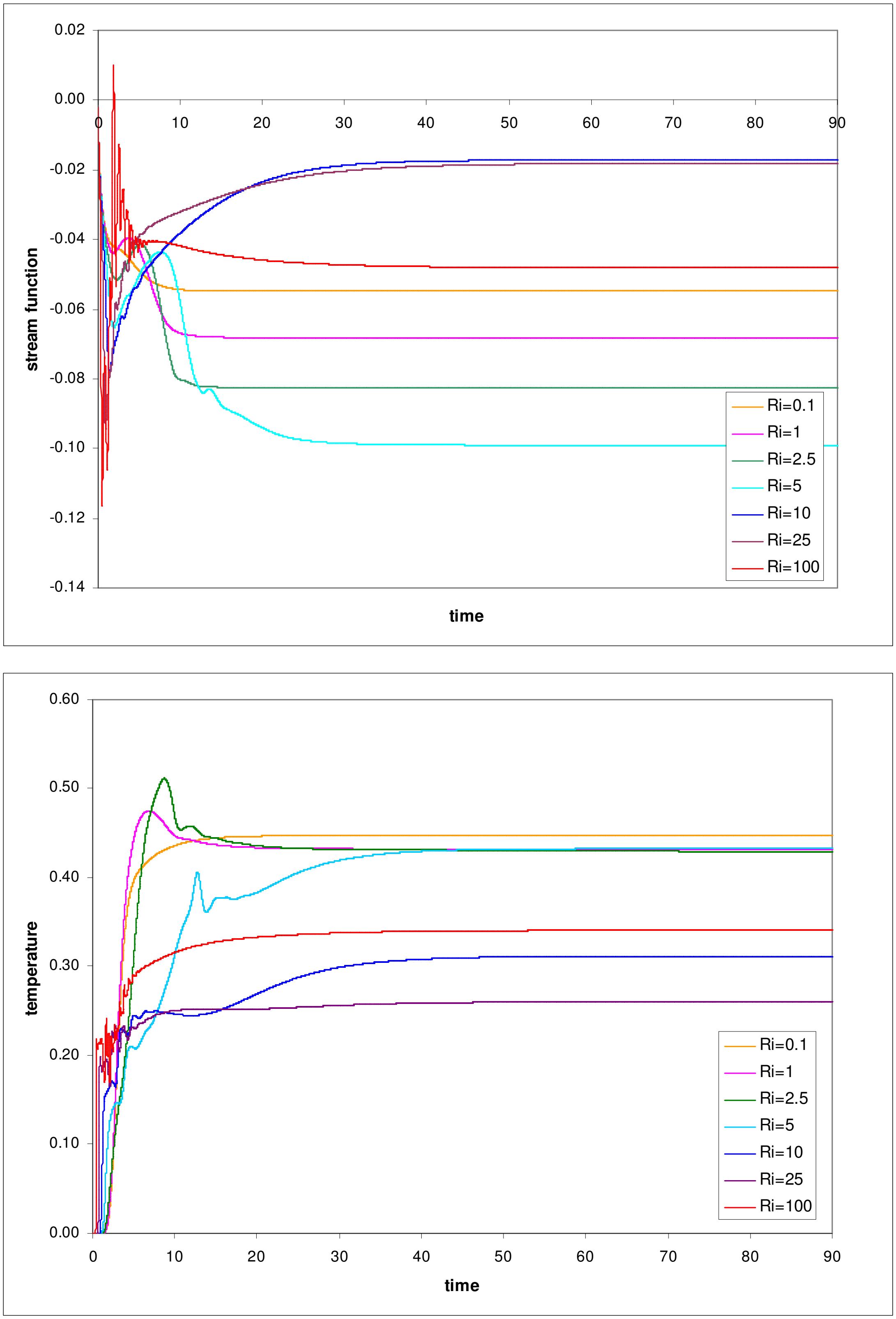


Figure 6.15. Transient variation in stream function and temperature values for various Ri numbers at a point which is located in (0.5,0.375), for Re =400 and 1/2 aspect ratio

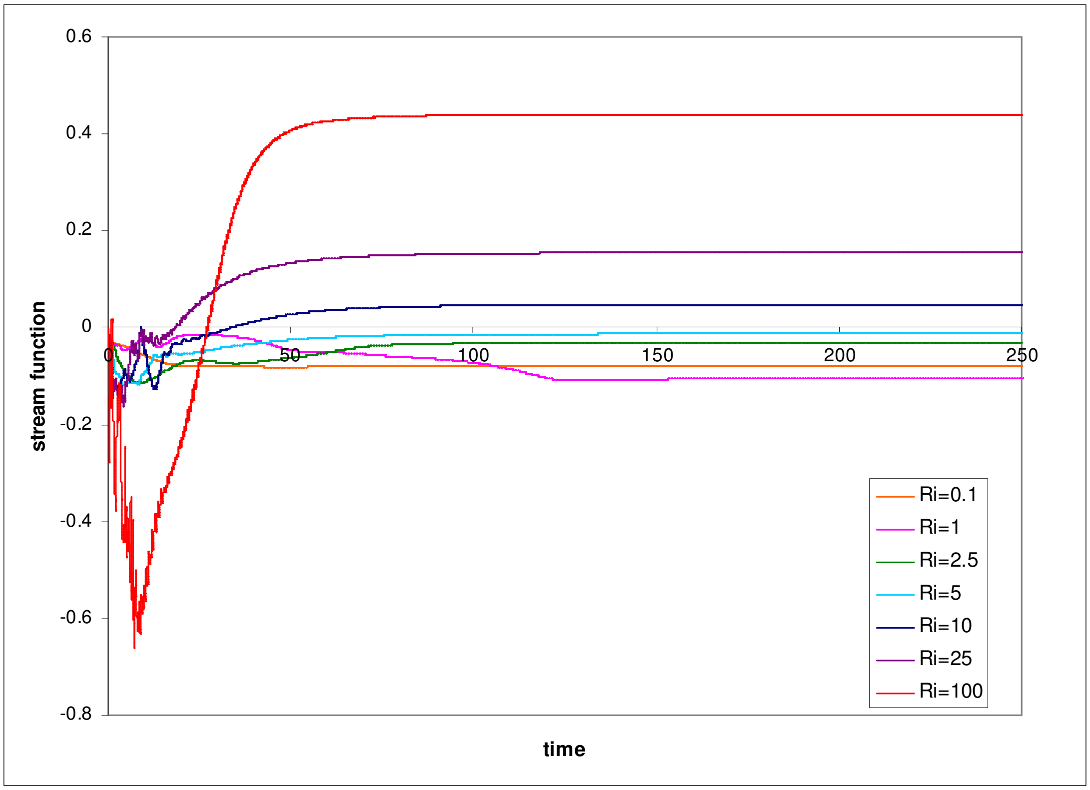


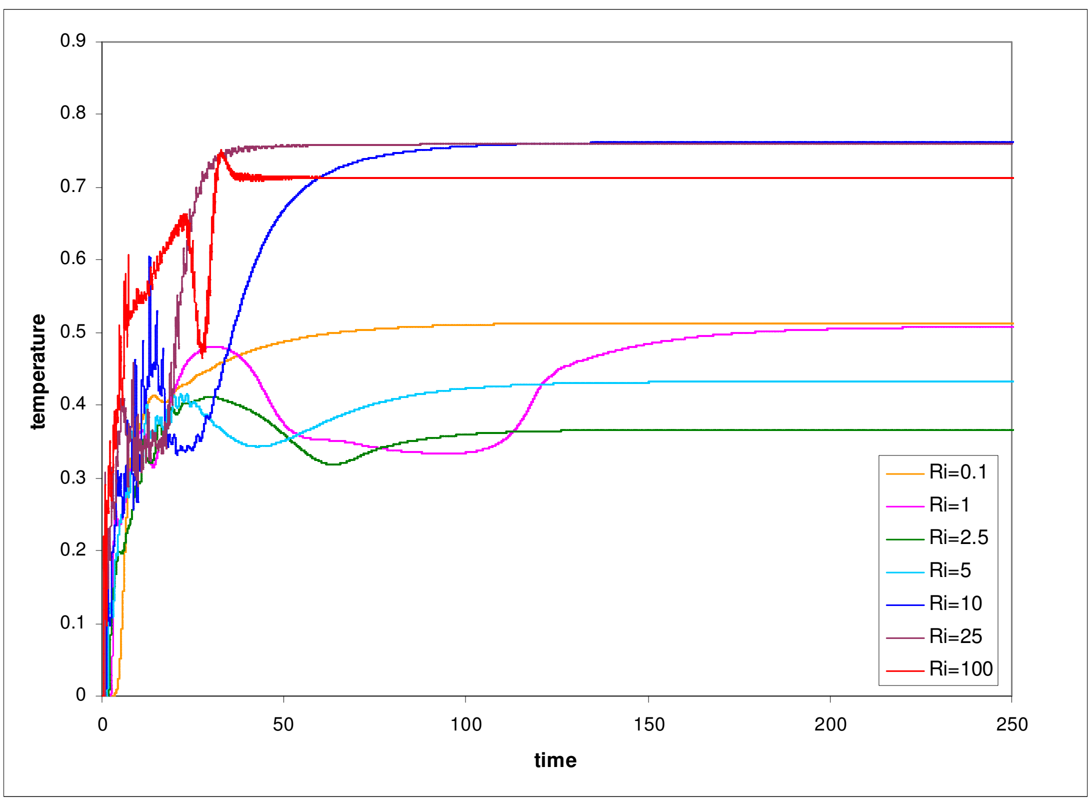


Figure 6.16. Transient variation in stream function and temperature values for various Ri numbers at a point which is located in (0.5,0.65), for Re = 800 and 2/3 aspect ratio

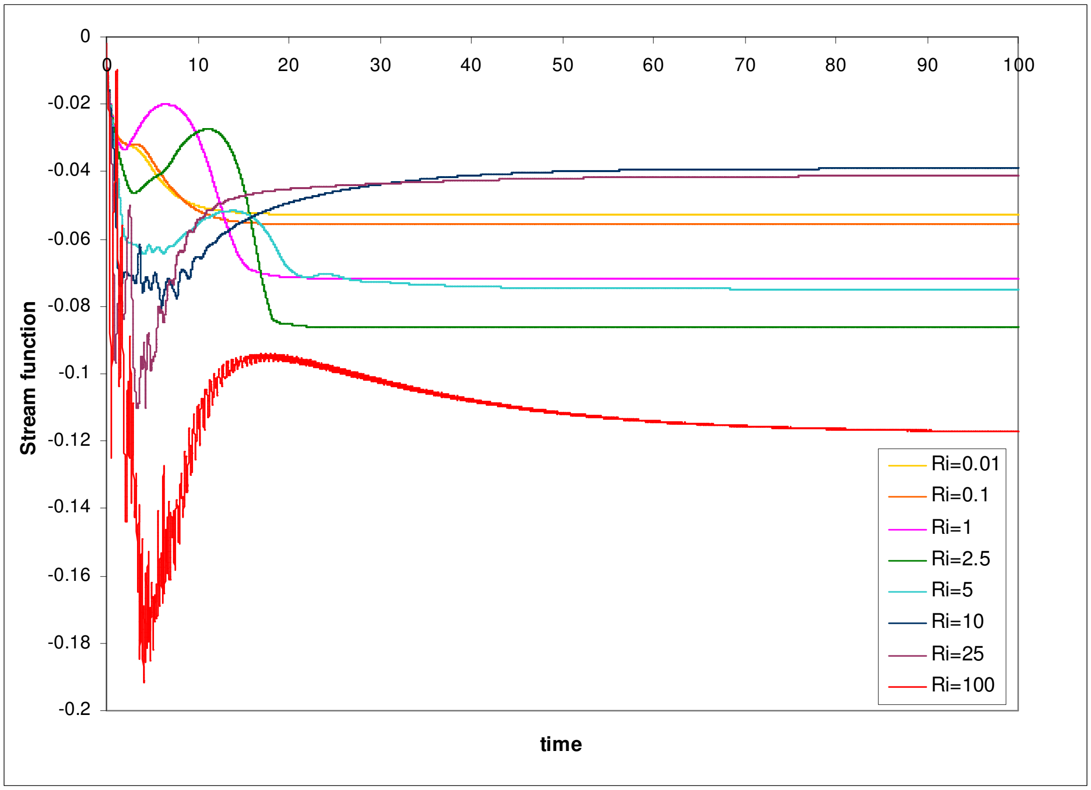


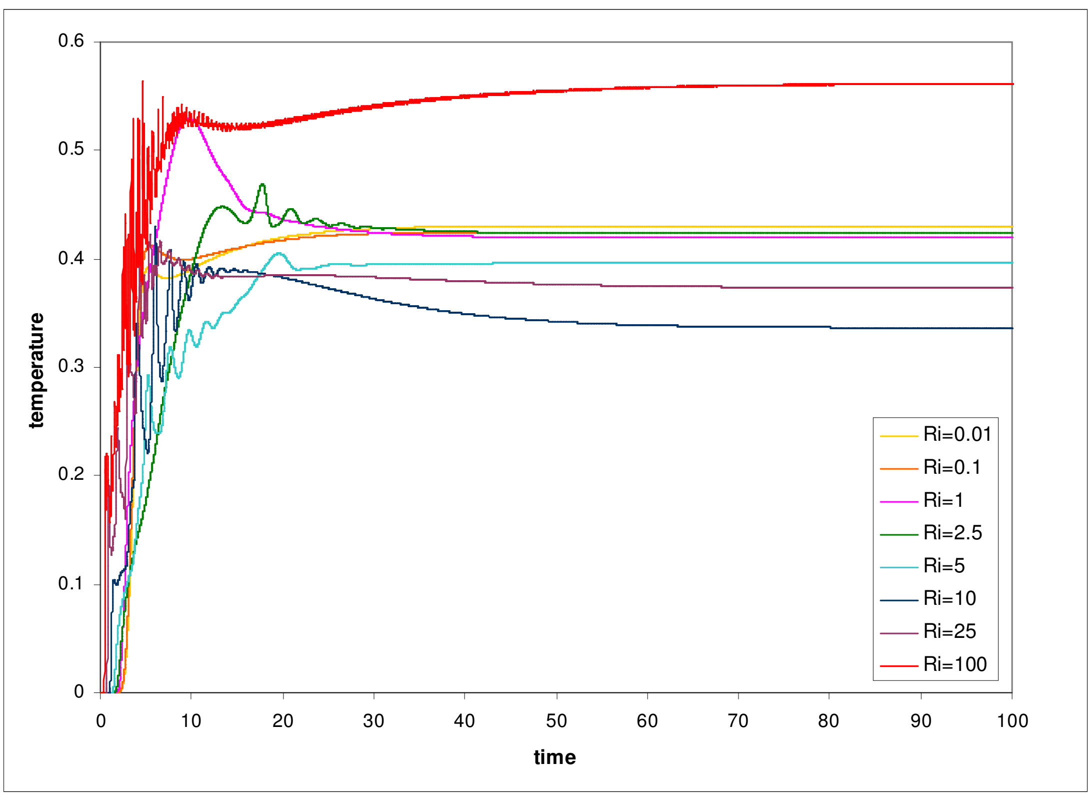


Figure 6.17. Transient variation in stream function and temperature values for various Ri numbers at a point which is located in (0.5,0.375), for Re =800 and 1/2 aspect ratio

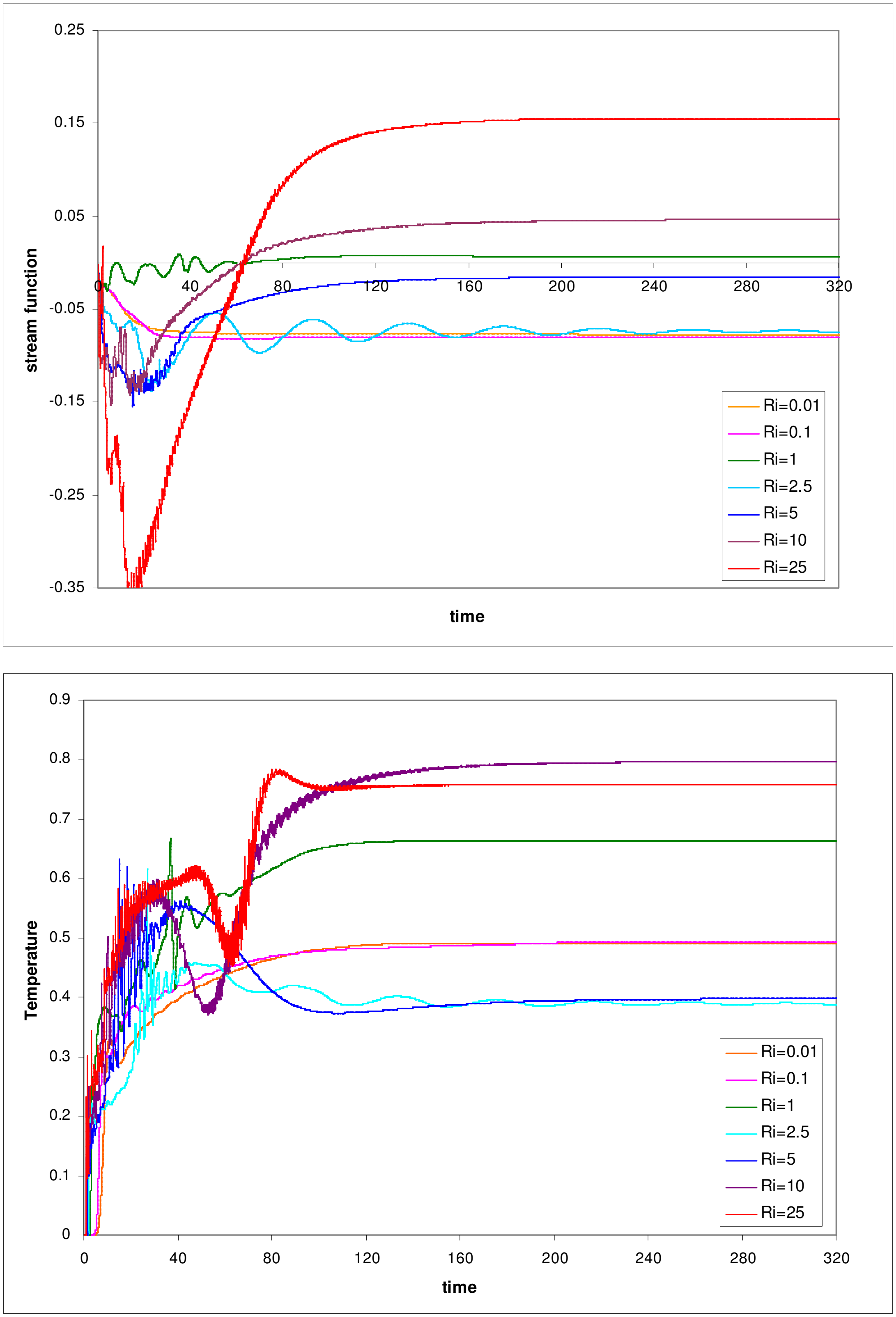


Figure 6.18. Transient variation in stream function and temperature values for various Ri numbers at a point which is located in ( 0.5,0.65), for Re=1500 and 2/3 aspect ratio

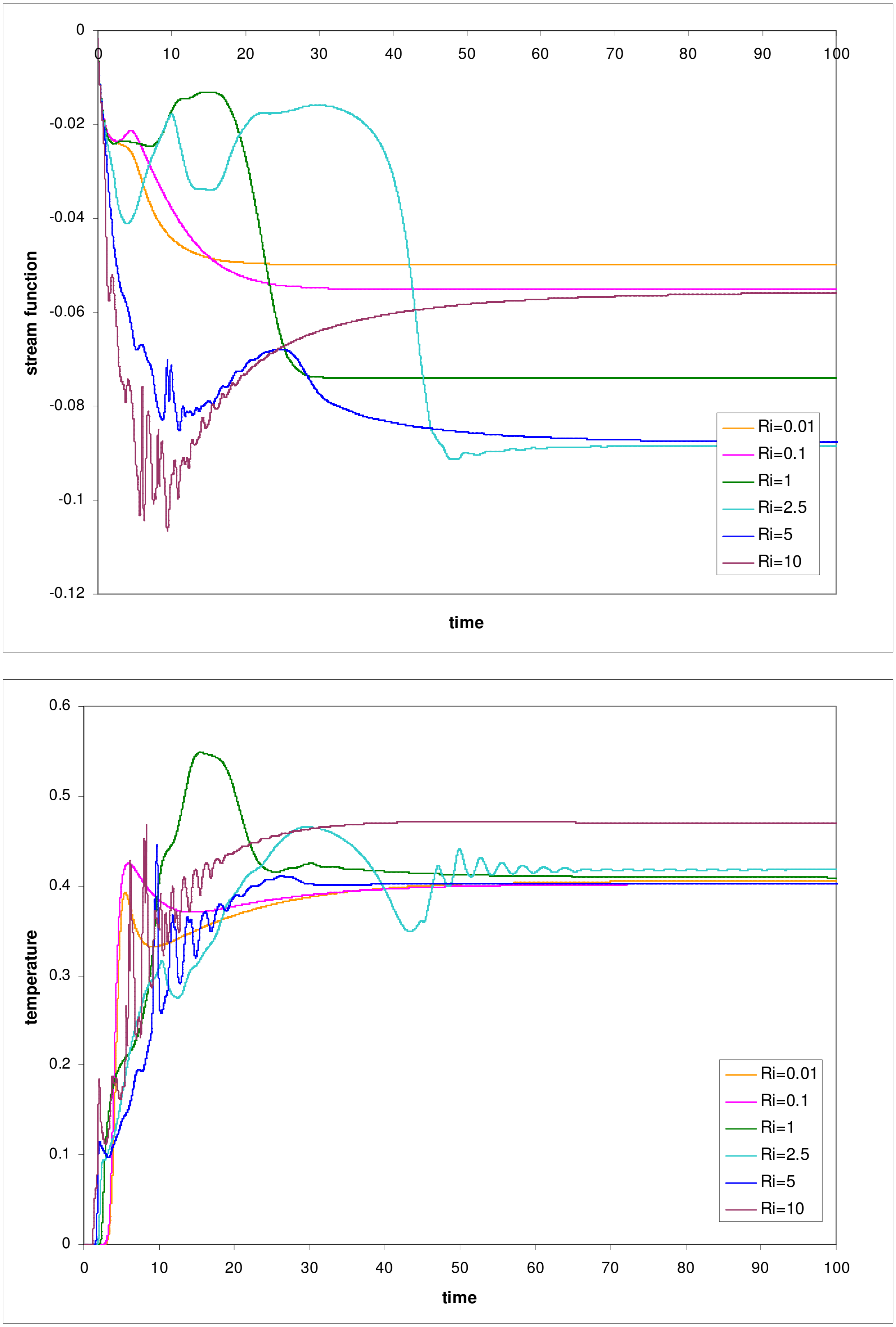


Figure 6.19. Transient variation in stream function and temperature values for various Ri numbers at a point which is located in (0.5,0.375) for Re=1500 and 1/2 aspect ratio

### 6.2. Nusselt Number Variation along the Lid Surface

As mentioned in section (6.1), heat transfer performance can be evaluated based on the temperature gradients along the surface of the cavity. Thickness of thermal boundary layers over the surface is the measure for the heat transfer performance and moreover this condition may be further assessed by the numerically obtained temperature data for the lid. Then, Nusselt number which quantifies convective heat transfer from the surface is investigated to determine the heat transfer characteristic for the range of Richardson and Reynolds numbers along the lid surface. Local Nusselt number along the moving lid surface is defined by

$$Nu_x = \frac{h_x L}{k} = \frac{L}{T_H - T_L} \left. \frac{\partial T}{\partial y} \right|_{lid} \tag{6.2}$$

where, $h_x$ is the local convective heat transfer coefficient and $k$ is the thermal conductivity of the fluid and L represents the characteristic length.

In curvilinear coordinates equation (6.2) is expressed as

$$Nu_x = -\frac{1}{J}\left( x_\xi \frac{\partial T}{\partial \eta} - x_\eta \frac{\partial T}{\partial \xi} \right). \tag{6.3}$$

Besides, average Nusselt number on the lid surface would be obtained by integration of local Nusselt numbers along the lid.

$$Nu = \int_0^1 Nu_x \, dX \tag{6.4}$$

The distribution of local Nusselt number along the moving lid surface is demonstrated for different values of Richardson numbers in figures (6.20)-(6.27). According to these results, the values of Nusselt number increase in magnitude with the increase of Richardson number. As mentioned previously small Richardson numbers indicate inertia dominated flows, whereas, small Reynolds numbers along with large Richardson numbers lead to buoyancy dominated flows. In inertia dominated flows, high heat transfer areas only emerge at the left side of the lid and in buoyancy dominated flows where the heat transfer separates the thermal boundary layers from the right side of the wall, the peak points can be detected in the vicinity of right corner and as the Richardson number and Reynolds number increase these peak points at two corners attain higher values. Therefore the heat transfer performance along the moving lid surface is affected not only by magnitude of buoyancy force but also by the magnitude to inertial force. Based on the comparison of the local and the average Nusselt number data between two aspect ratios any obvious relation can not be stated for the effect of aspect ratio on heat transfer performance.

Transient variations in average Nusselt numbers along the lid surface for various Richardson numbers at Reynolds numbers 200, 400, 800 and 1500 are demonstrated in figures (6.36)-(6.39). These figures show the behavior of Nusselt number in time domain. Furthermore, it can be observed that like the temperature and stream function transient variations demonstrated in figures (6.12)-(6.19), no periodicity observed within the range of studied parameters.

## 6.3. Shear Stress Distribution along the Lid Surface

Fluid flow inside the cavity is mainly induced by the shear force which is generated due to the motion of the lid. Therefore, the shear stress over the viscous fluid is investigated in term of the local friction factor distribution along the lid surface as

$$f_x = \frac{\sigma_x}{\rho U_L^2} = \frac{\mu}{\rho U_L^2} \left. \frac{\partial u}{\partial y} \right|_{Lid} . \tag{6.5}$$

Where $\sigma_x$ is the local shear stress along the moving lid and $U_L$ is the lid velocity. Transformation of equation (6.5) from cartesian to curvilinear coordinates yields

$$f_x = \frac{1}{\mathrm{Re}} \frac{X_\xi}{J} \frac{\partial U}{\partial \eta}\bigg|_{Lid} \tag{6.6}$$

Local friction factor over the lid surface for Reynolds numbers of 200, 400, 800 and 1500 with the range of various Richardson numbers are shown in figures (6.28)-(6.35). In 2/3 aspect ratio cases it is noticed that an increase in Richardson number results in a decrease in local friction factor in the left side of the lid yet a larger and more extended increase in the right side. Moreover in 1/2 aspect ratio cavities with higher Richardson number values anti-symmetric behaviors for local friction factor are observed. Especially, for Reynolds number of 400 the anti-symmetric characteristic occurs almost at the center of the lid. This feature may be attributed to the cavity shape and the formation of two eddies of almost equal strength at elevated Richardson numbers.

From tables (6.1) and (6.2) it can be concluded that for a fixed Reynolds number and aspect ratio the strength of both inertial and buoyant induced vortices gets larger as Richardson number increases, except an interval in which the buoyant induced eddy forms and develops to some extent. Therefore, the fluid traveling along the lid surface with inertial vortex would be accelerated not only by the inertia but also by the buoyancy. Since the fluid velocity near the lid can get faster than that of the lid, then this feature can be attributed to the negative values obtained for friction factor at the left side of the lid where the shear driven vortex circulates at high Richardson number.

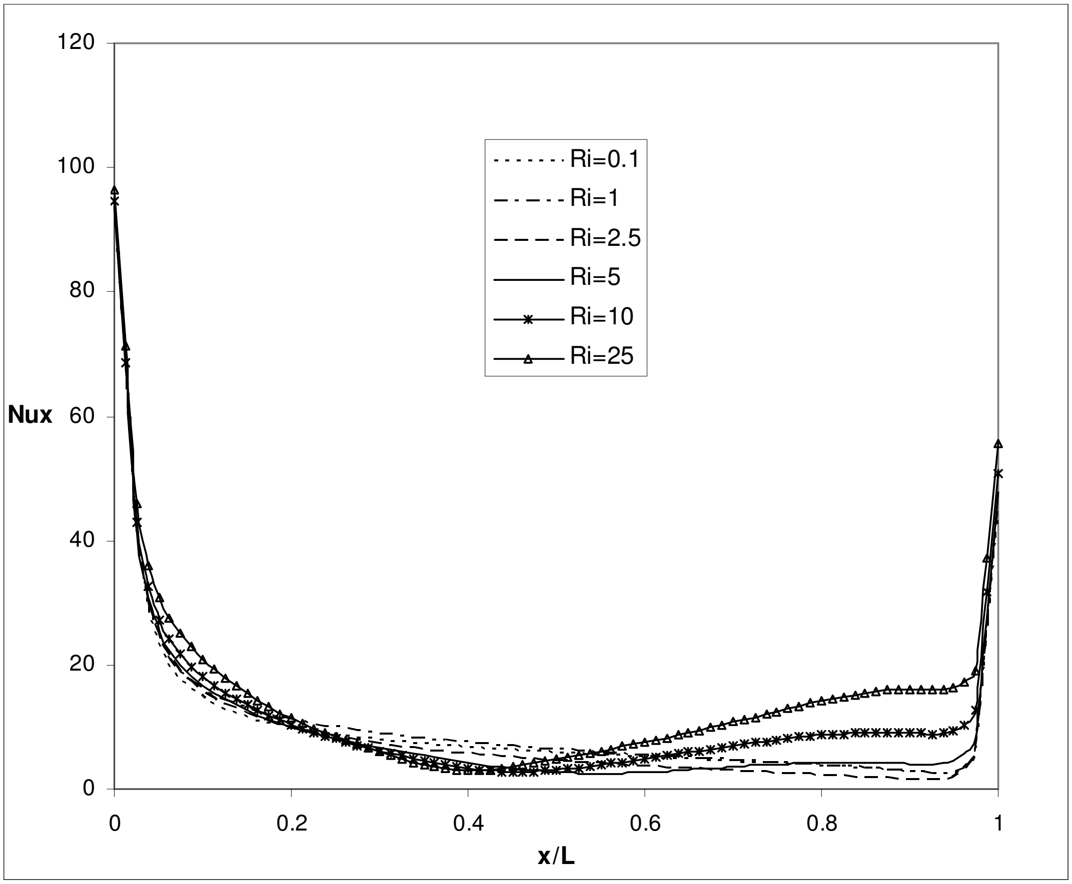


Figure 6.20. Local Nusselt number distribution along the moving lid at 2/3 aspect ratio cavity and Re = 200

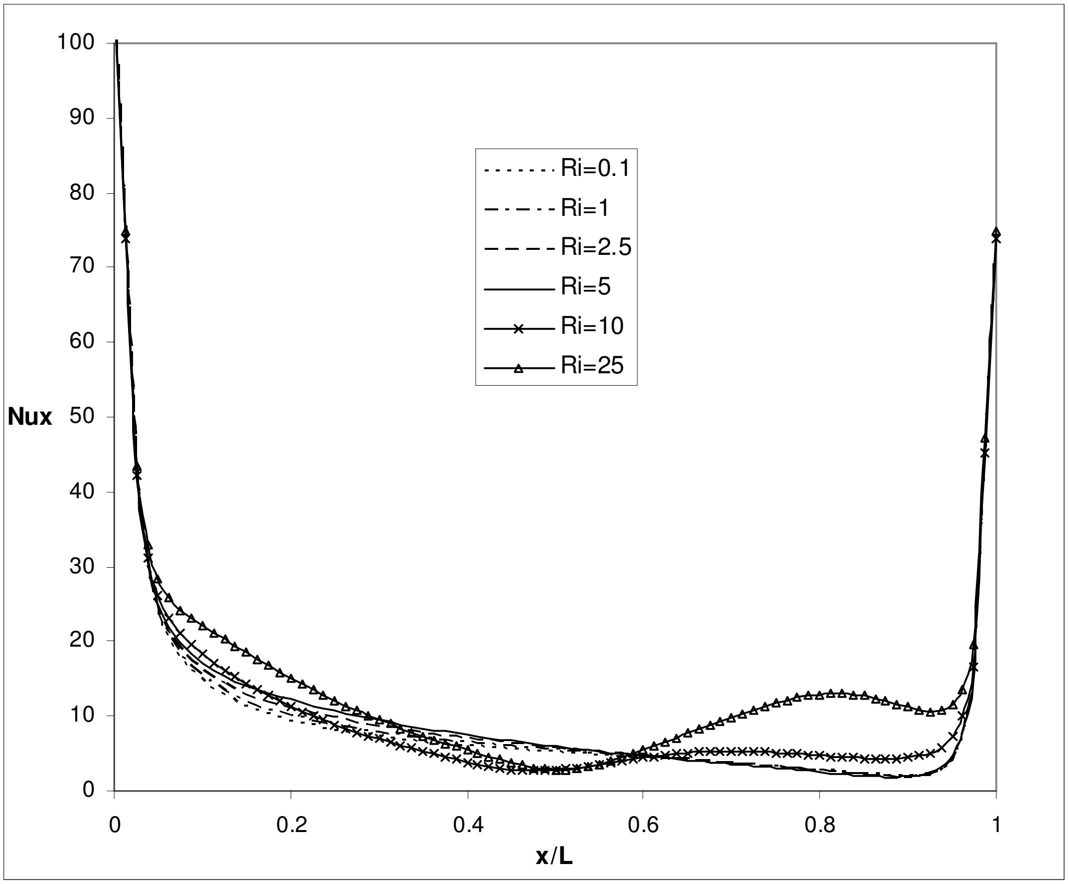


Figure 6.21. Local Nusselt number distribution along the moving lid at 1/2 aspect ratio cavity and Re = 200

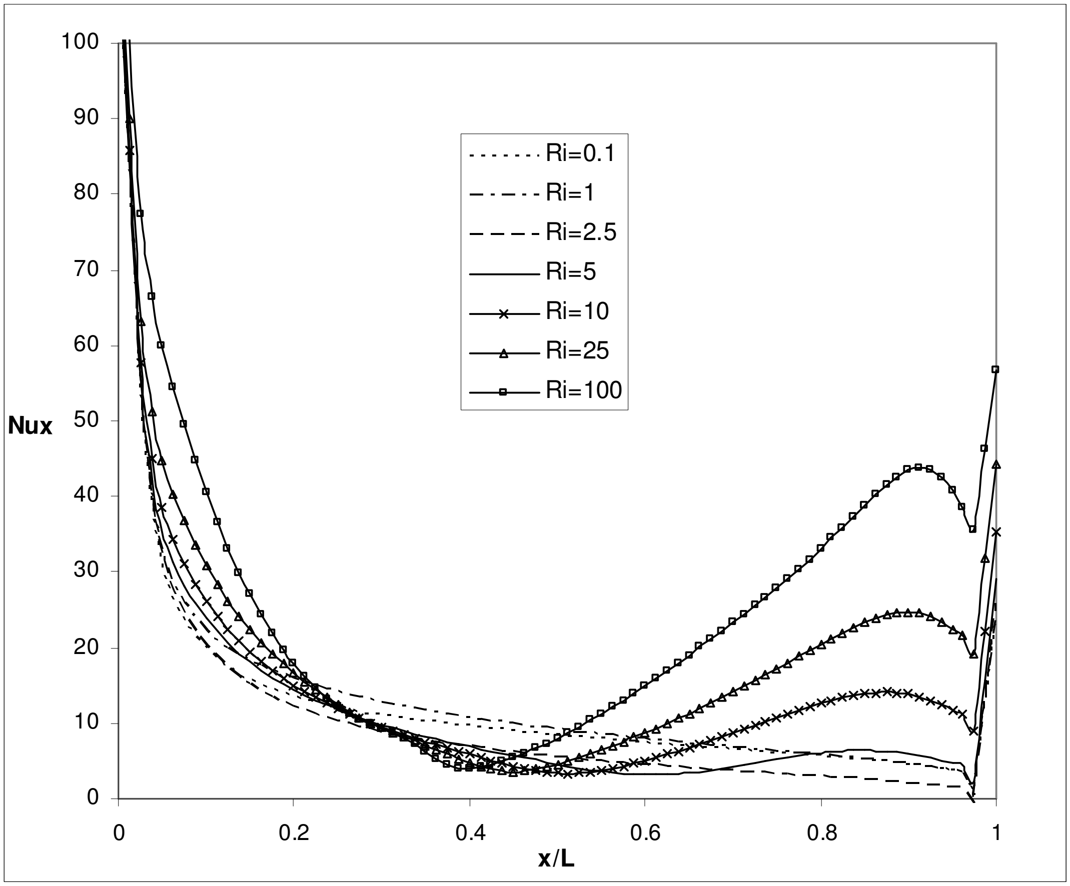


Figure 6.22. Local Nusselt number distribution along the moving lid at 2/3 aspect ratio cavity and Re = 400

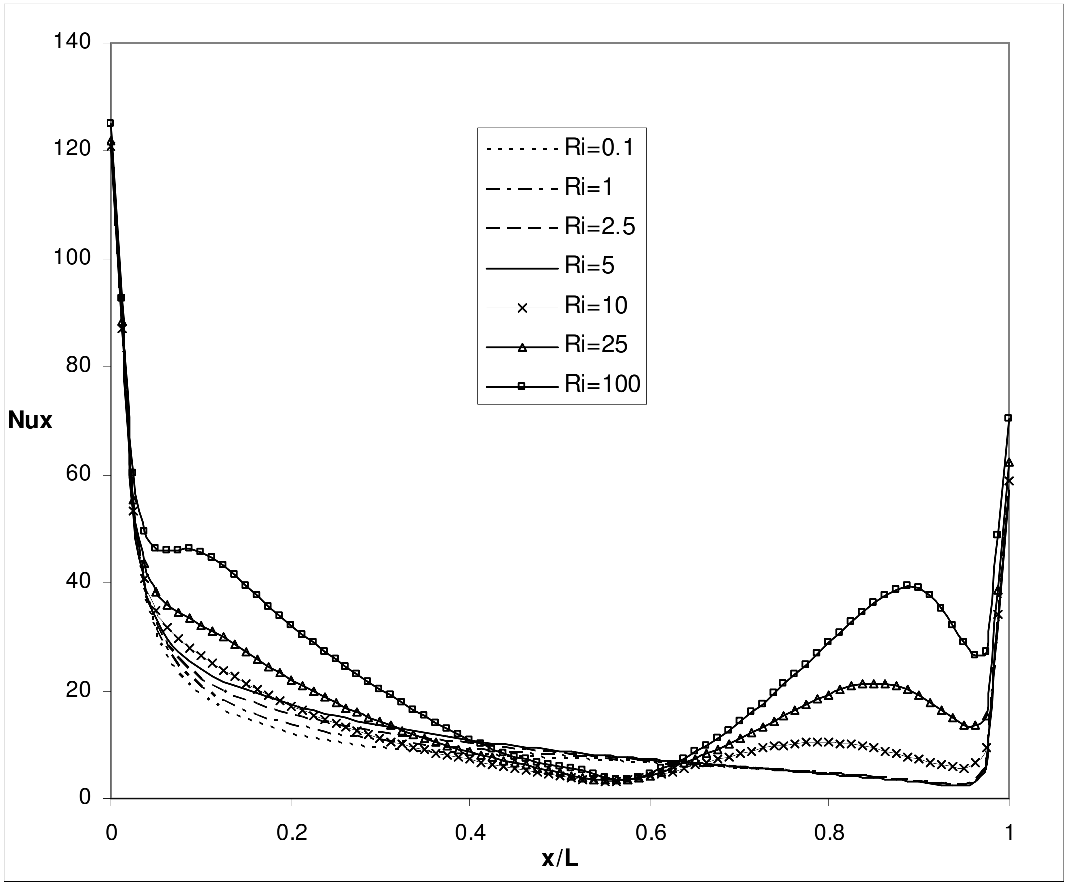


Figure 6.23. Local Nusselt number distribution along the moving lid at 1/2 aspect ratio cavity and Re = 400

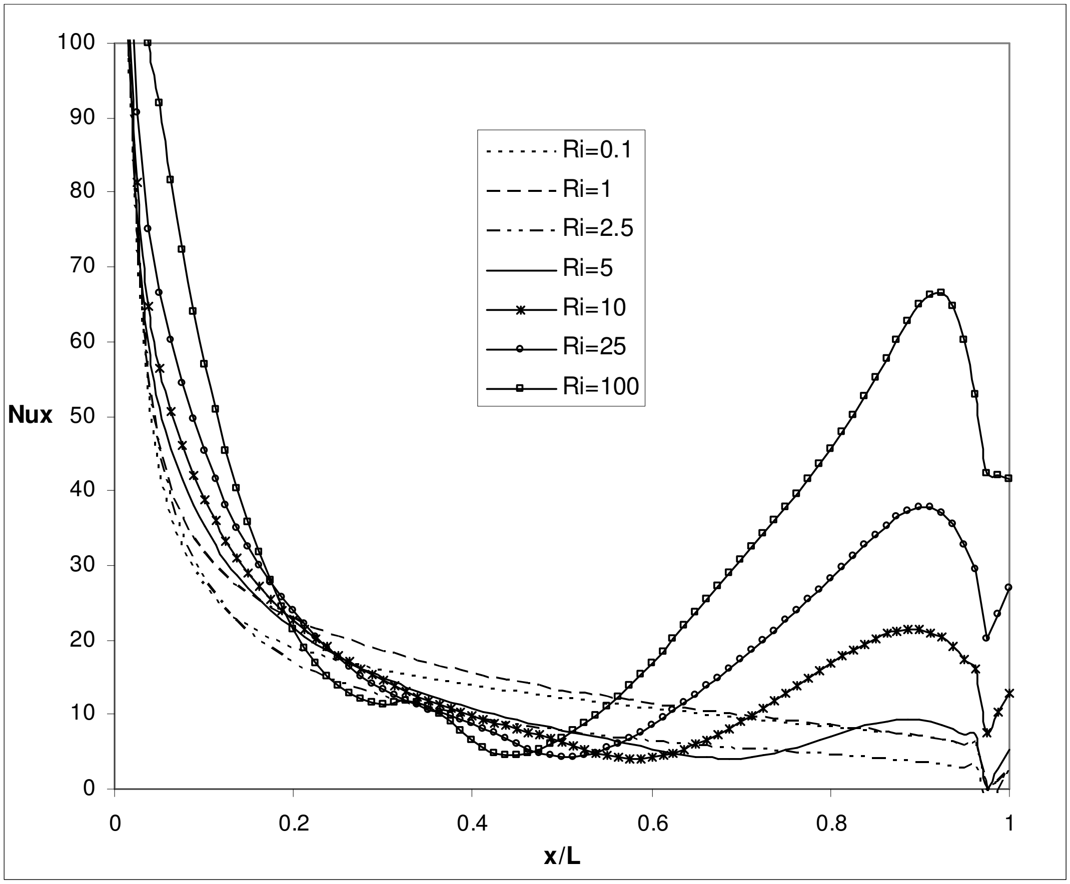


Figure 6.24. Local Nusselt number distribution along the moving lid at 2/3 aspect ratio cavity and Re = 800

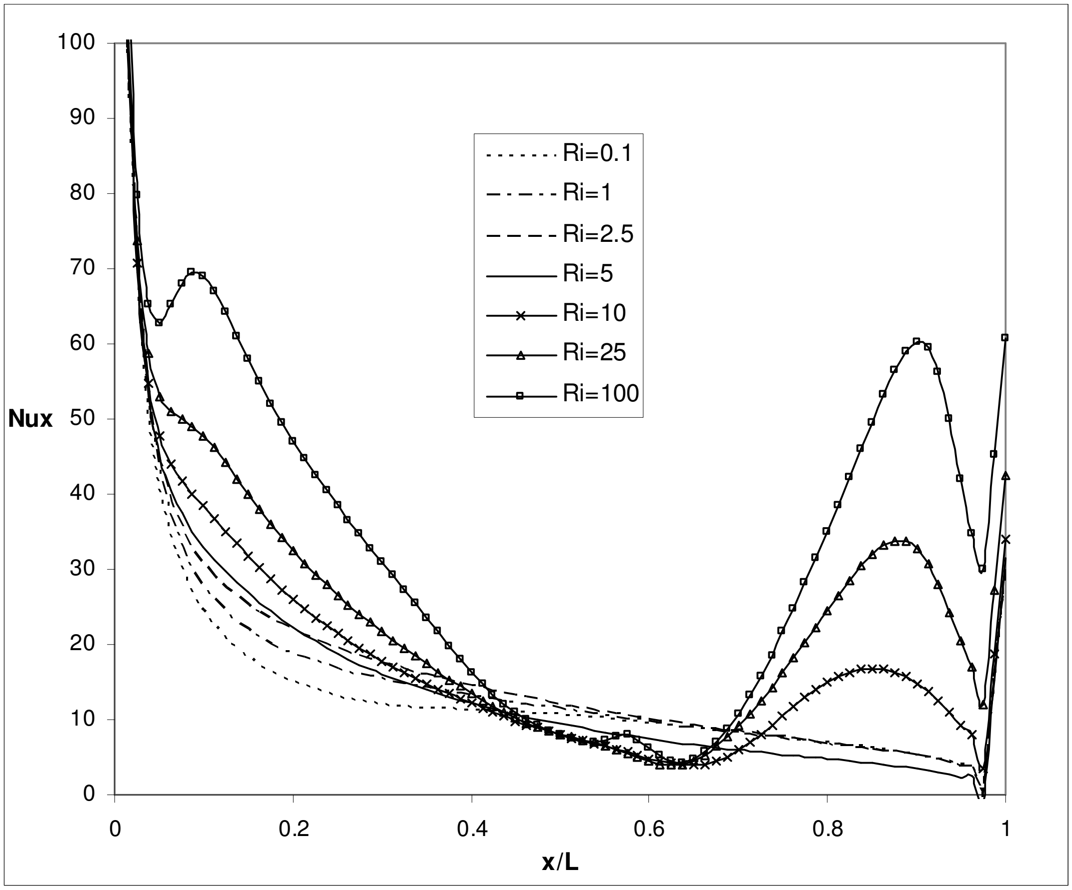


Figure 6.25. Local Nusselt number distribution along the moving lid at 1/2 aspect ratio cavity and Re = 800

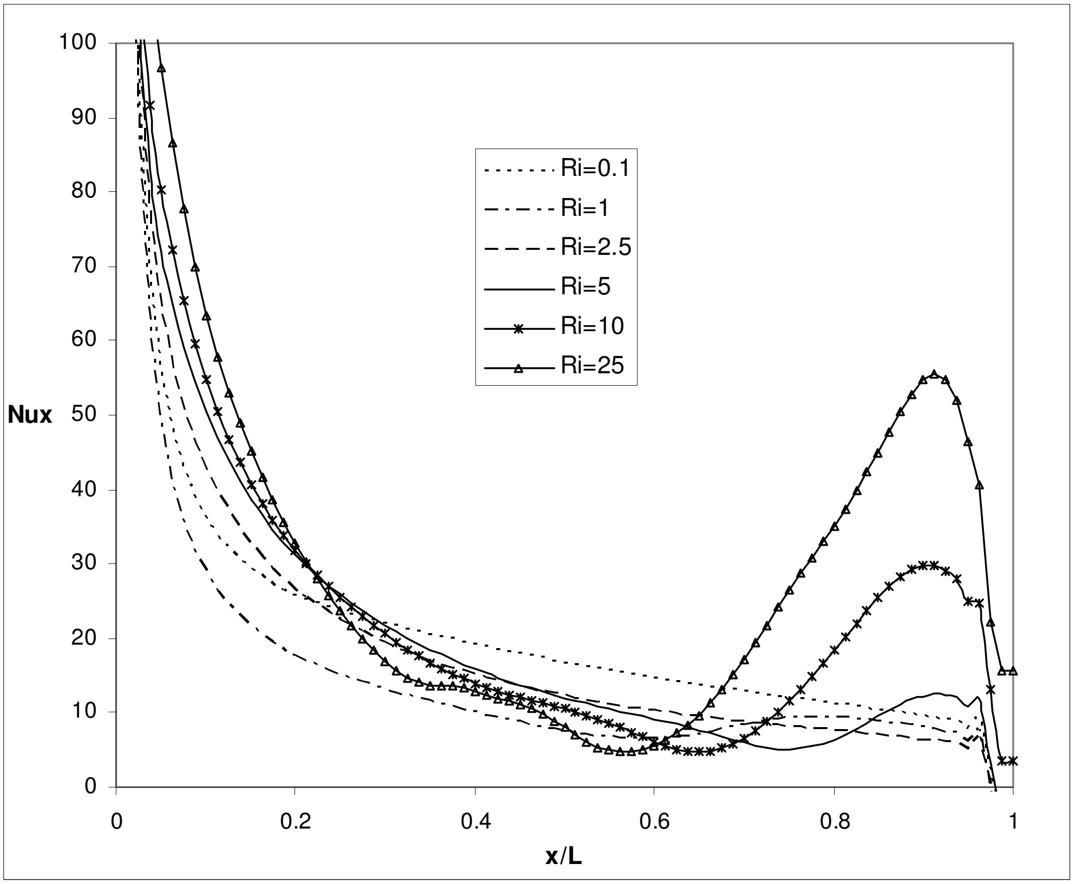


Figure 6.26. Local Nusselt number distribution along the moving lid at 2/3 aspect ratio cavity and Re = 1500

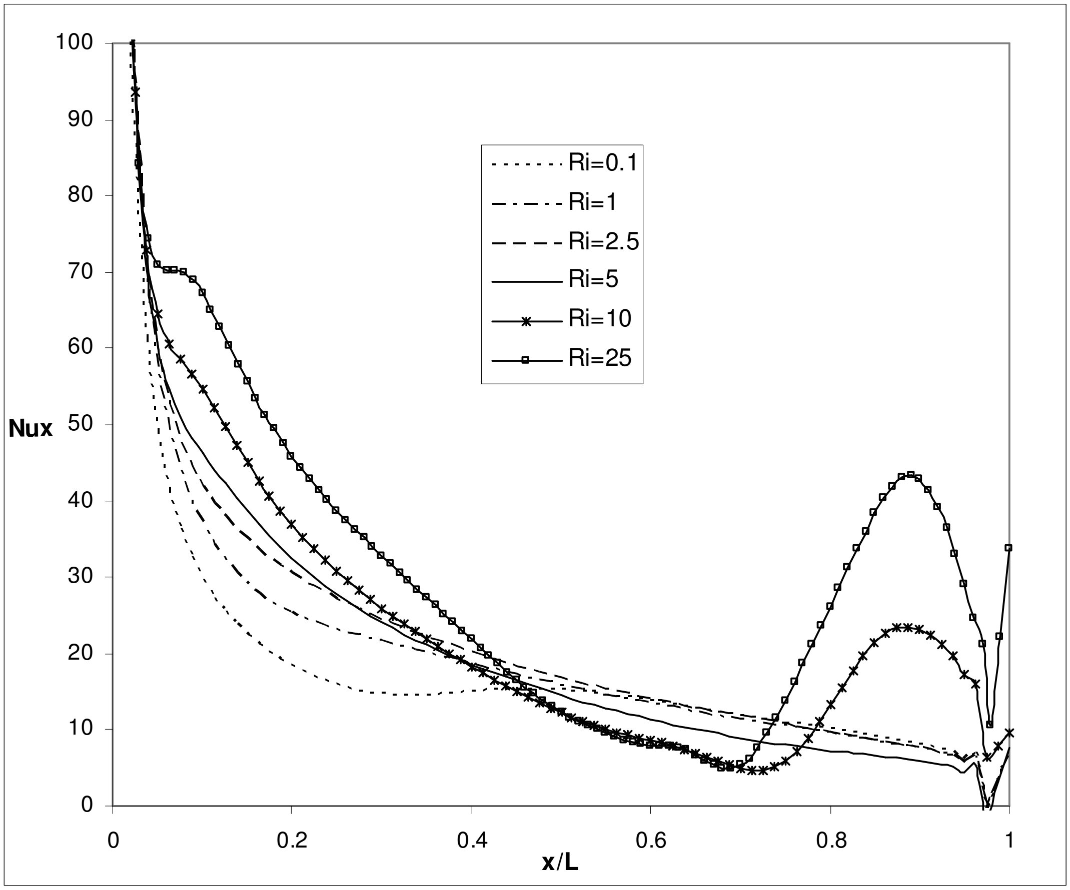


Figure 6.27. Local Nusselt number distribution along the moving lid at 1/2 aspect ratio cavity and Re = 1500

Table 6.3. Average Nusselt number values along the lid surface

| Average Nusselt Number Values | | | |
|---|---|---|---|
| **Re** | **Ri** | **AR=2/3** | **AR=1/2** |
| 200 | 0.01 | 8.91 | 8.96 |
| | 0.1 | 9 | 9.15 |
| | 1 | 9.58 | 9.42 |
| | 2.5 | 8.3 | 9.8 |
| | 5 | 8.63 | 10.2 |
| | 10 | 10.5 | 10.02 |
| | 25 | 13.38 | 13.44 |
| | | | |
| 400 | 0.01 | 11.71 | 11.3 |
| | 0.1 | 11.92 | 11.94 |
| | 1 | 12.89 | 12.62 |
| | 2.5 | 9.93 | 13.56 |
| | 5 | 11.39 | 13.3 |
| | 10 | 13.98 | 17.88 |
| | 25 | 18.07 | 24.19 |
| | 100 | 25.68 | 29.31 |
| | | | |
| 800 | 0.01 | 16.09 | 14.37 |
| | 0.1 | 15.71 | 14.56 |
| | 1 | 17.94 | 15.96 |
| | 2.5 | 12.87 | 17.08 |
| | 5 | 15.35 | 17.99 |
| | 10 | 18.6 | 15.75 |
| | 25 | 24 | 23.48 |
| | 100 | 34.18 | 33.05 |
| | | | |
| 1500 | 0.01 | 21.62 | 18.47 |
| | 0.1 | 22.2 | 18.83 |
| | 1 | 15.88 | 21.5 |
| | 2.5 | 20.44 | 23.2 |
| | 5 | 22.52 | 22.32 |
| | 10 | 25.18 | 25.49 |
| | 25 | 32.22 | 31.67 |

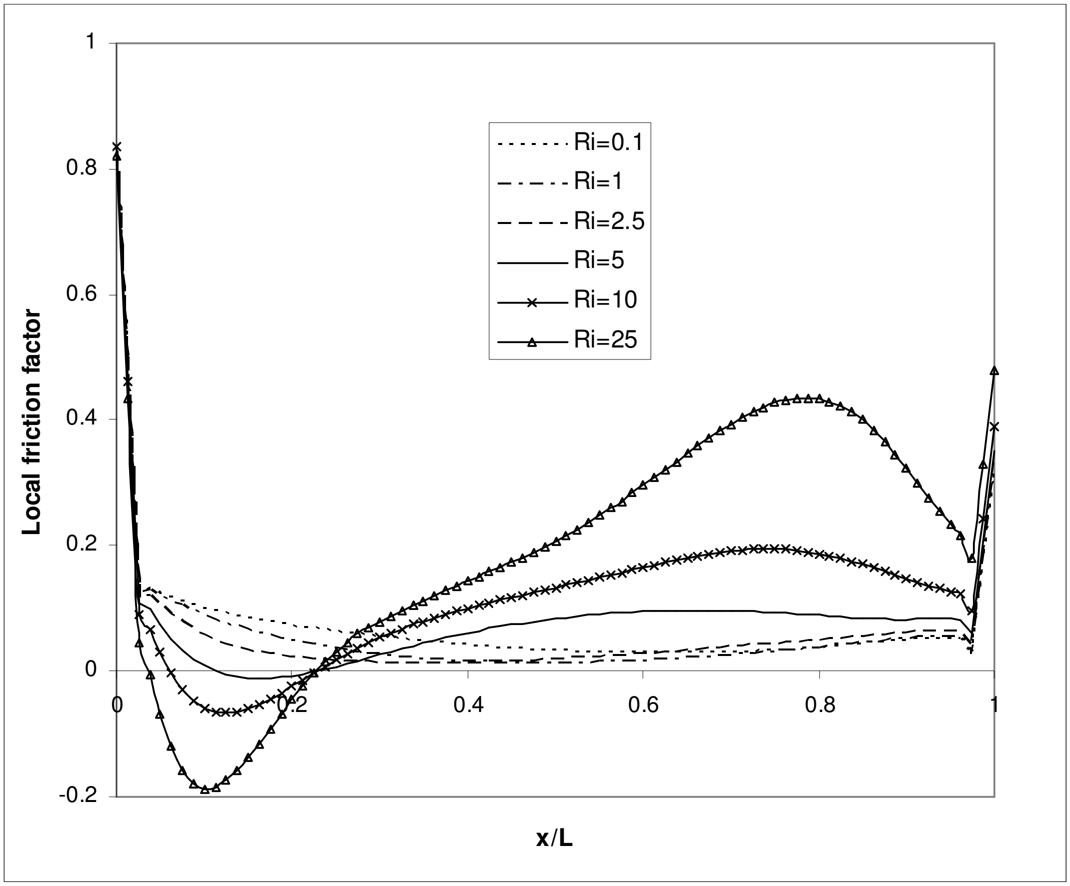


Figure 6.28. Local friction factor distribution along the moving lid at 2/3 aspect ratio cavity and Re = 200

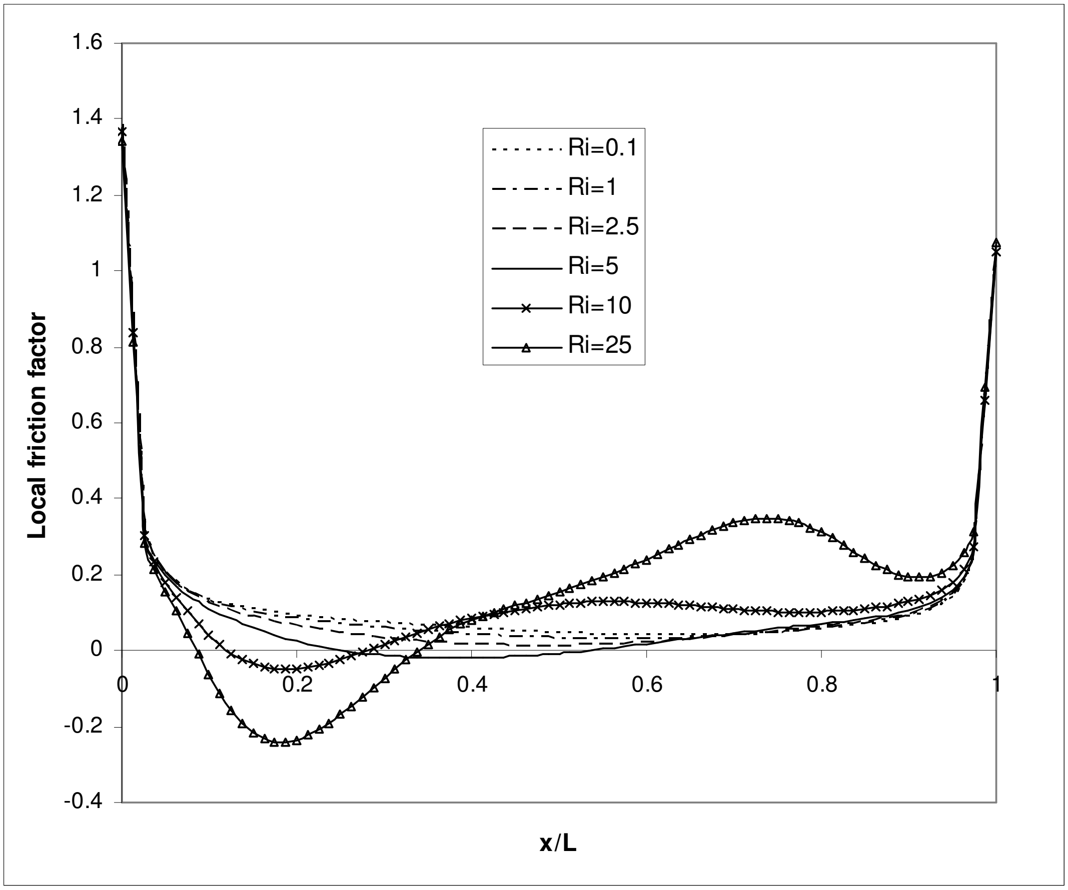


Figure 6.29. Local friction factor distribution along the moving lid at 1/2 aspect ratio cavity and Re = 200

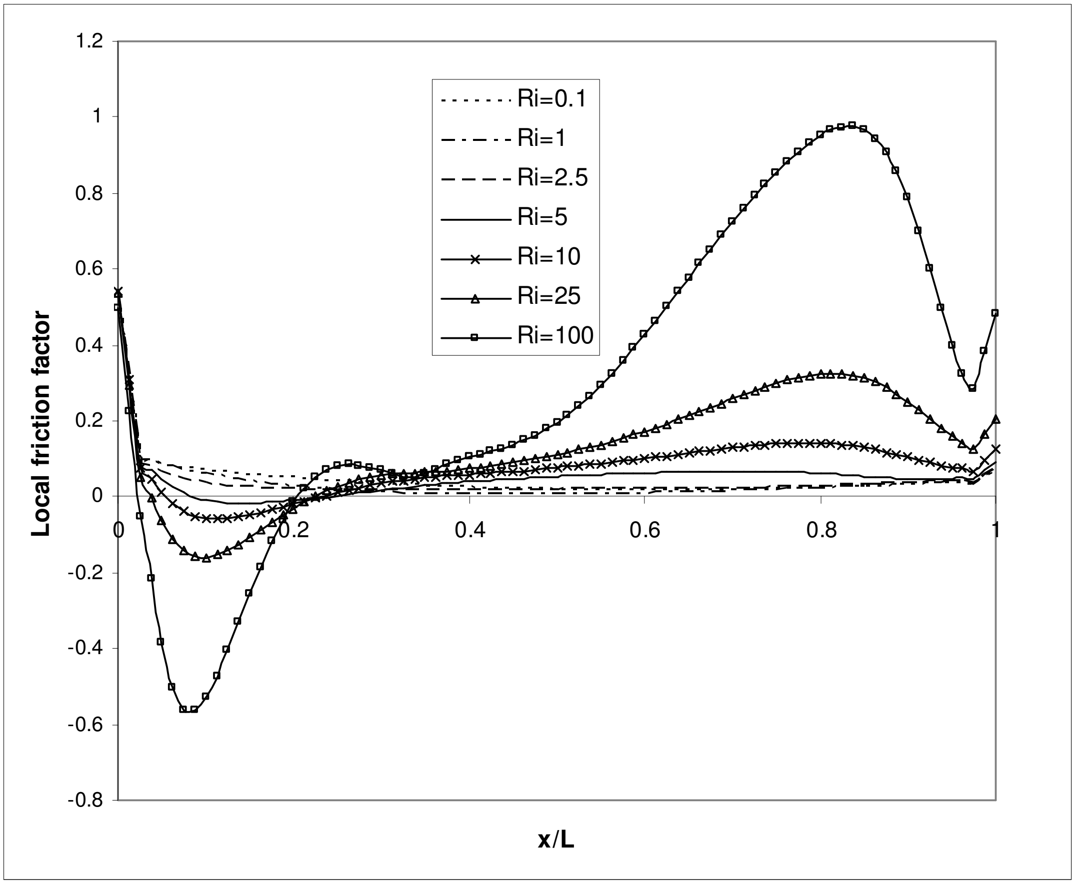


Figure 6.30. Local friction factor distribution along the moving lid at 2/3 aspect ratio cavity and Re = 400

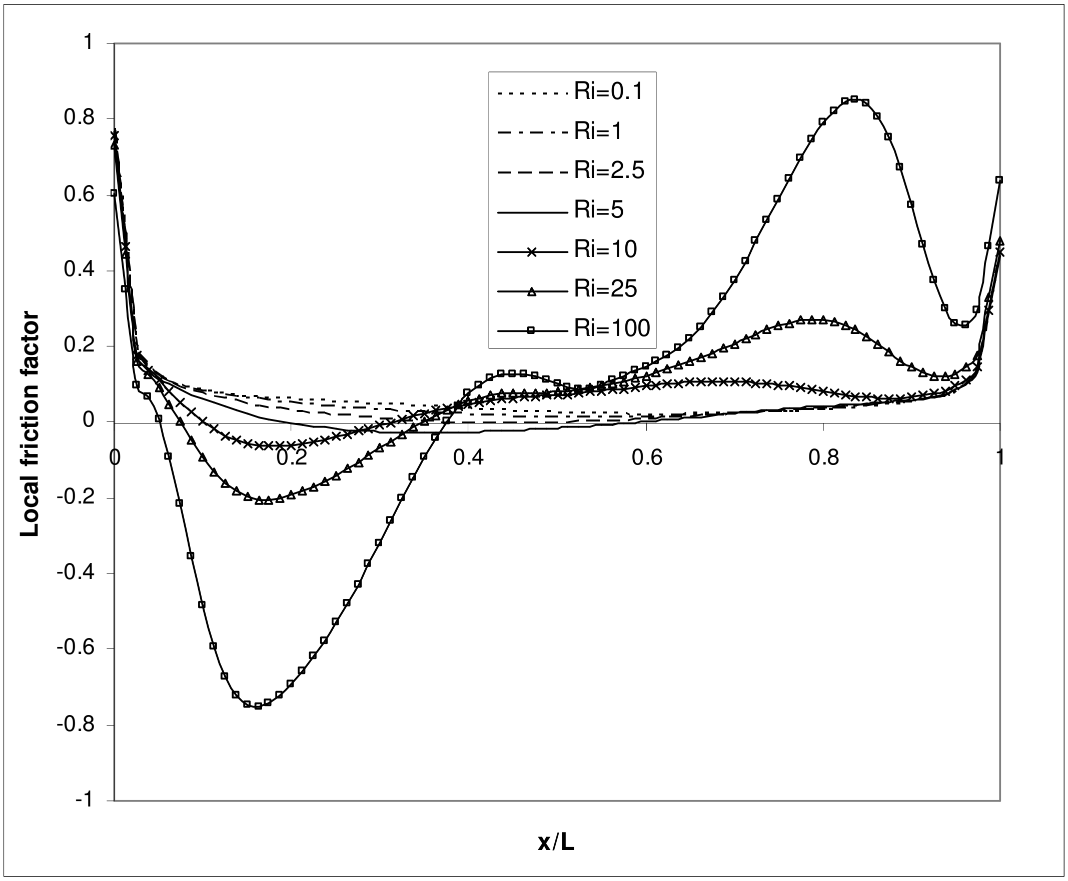


Figure 6.31. Local friction factor distribution along the moving lid at 1/2 aspect ratio cavity and Re = 400

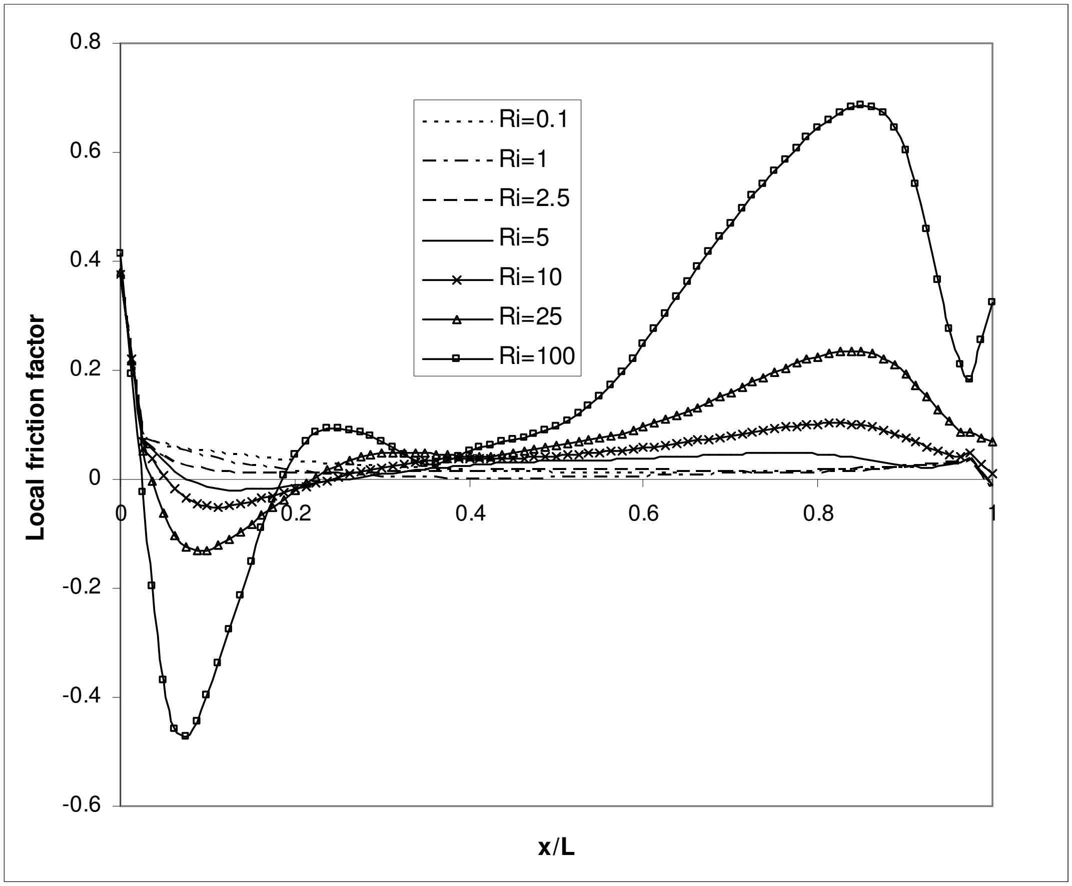


Figure 6.32. Local friction factor distribution along the moving lid at 2/3 aspect ratio cavity and Re = 800

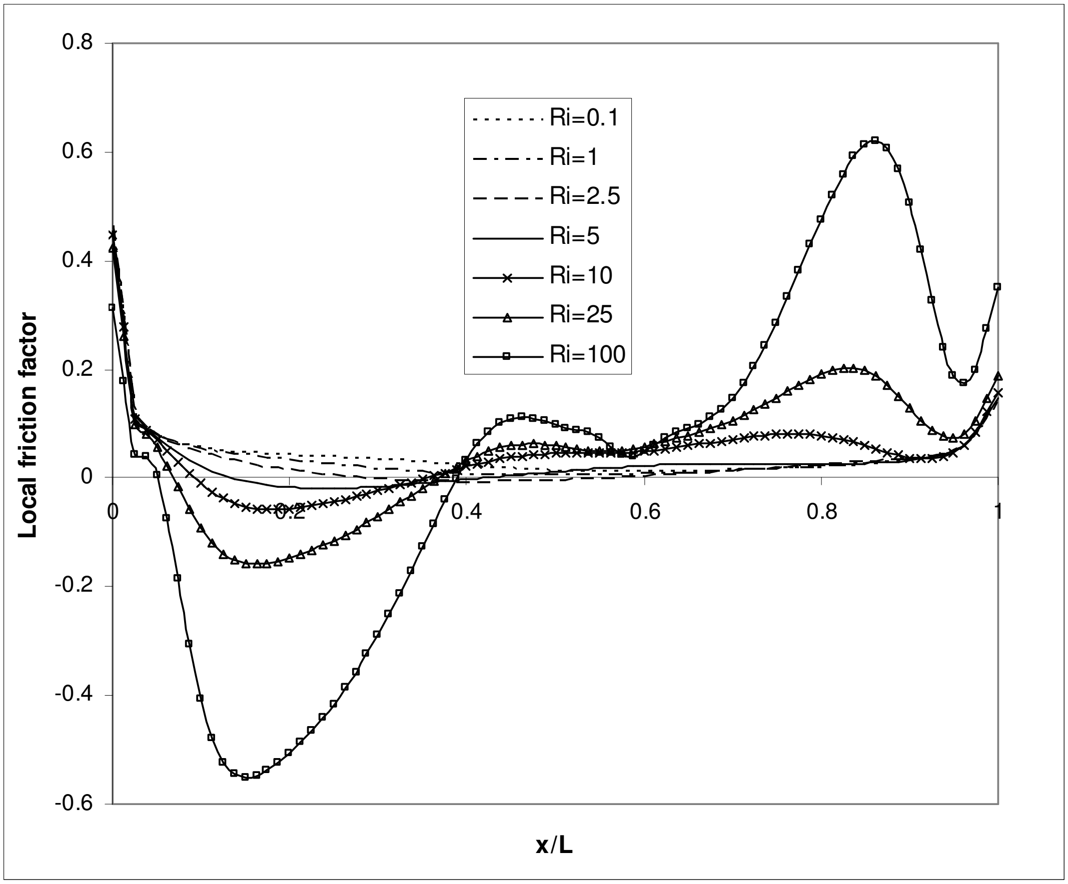


Figure 6.33. Local friction factor distribution along the moving lid at 1/2 aspect ratio cavity and Re = 800

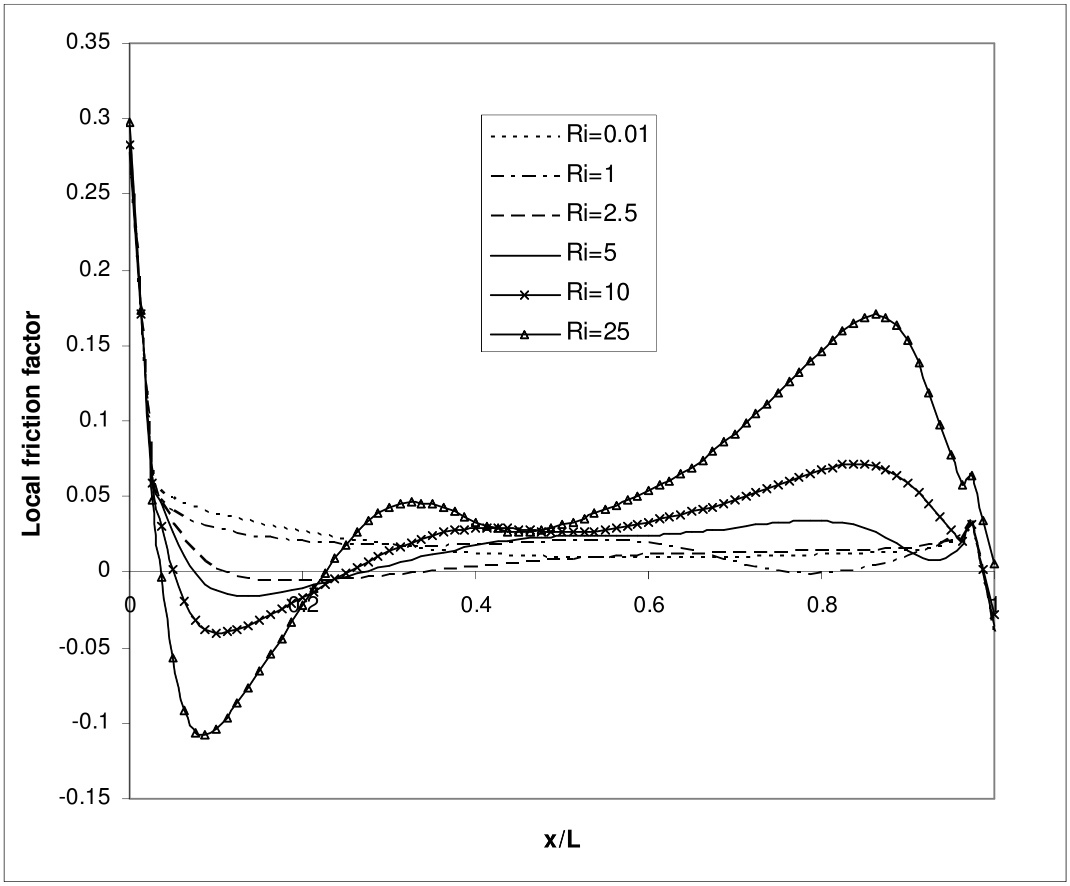


Figure 6.34. Local friction factor distribution along the moving lid at 2/3 aspect ratio cavity and Re = 1500

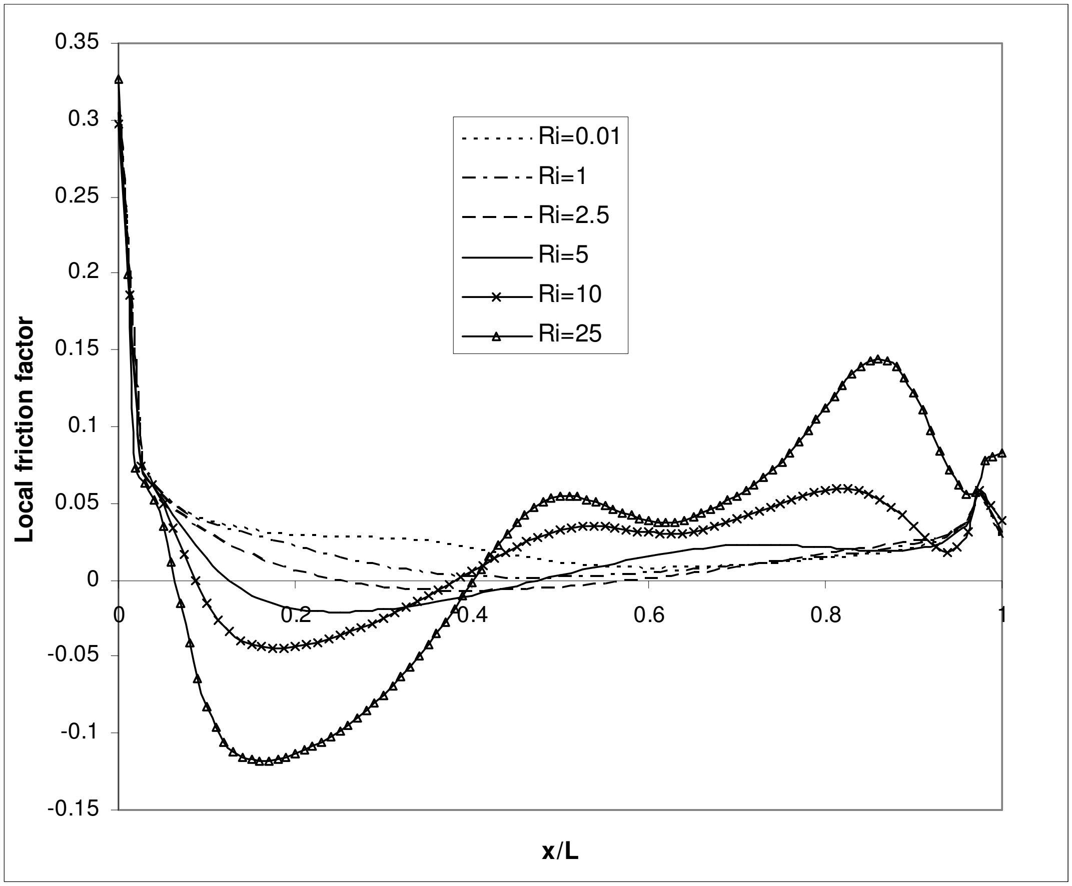


Figure 6.35. Local friction factor distribution along the moving lid at 1/2 aspect ratio cavity and Re = 1500

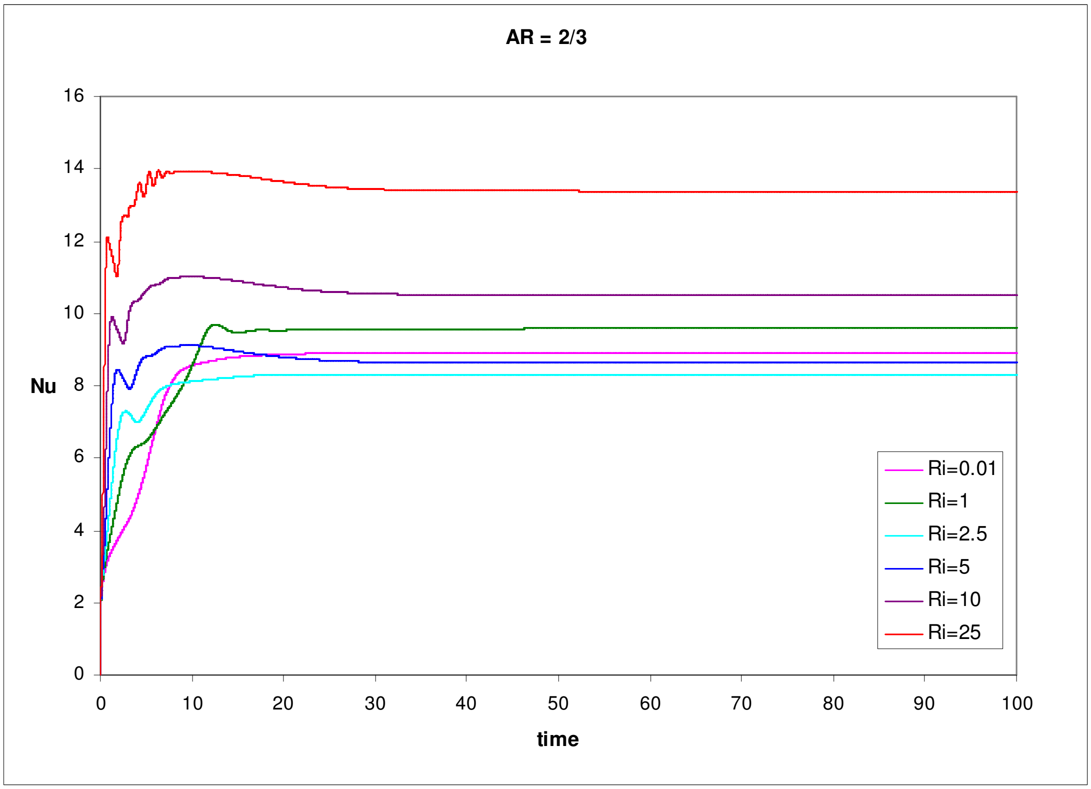


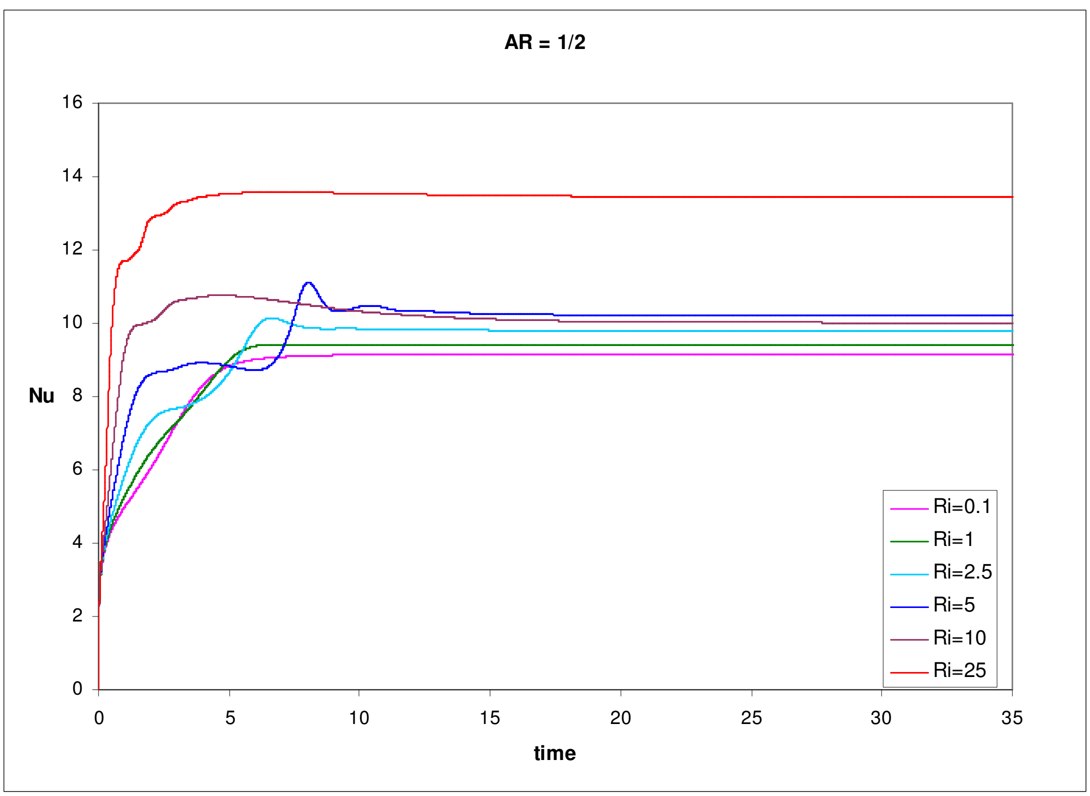


Figure 6.36. Transient variation in average Nusselt number values for various Ri numbers at a point which is located in (0.5,0.65) for Re =200

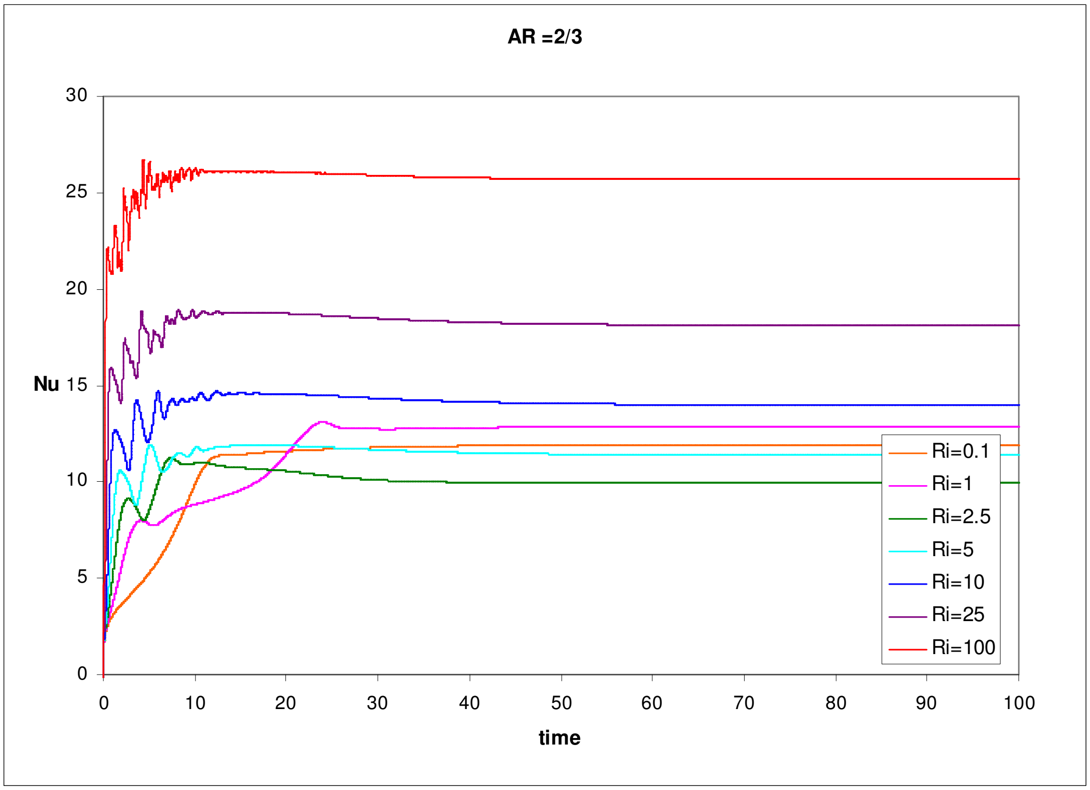


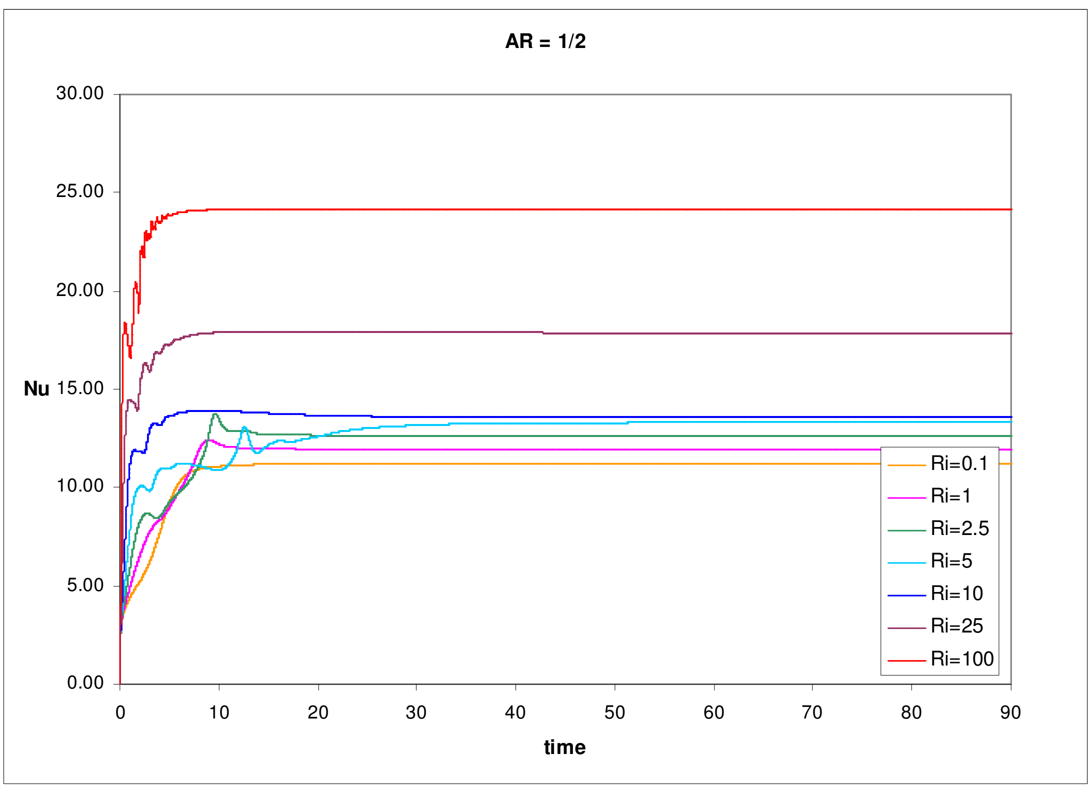


Figure 6.37. Transient variation in average Nusselt number values for various Ri numbers at a point which is located in (0.5,0.65) for Re =400

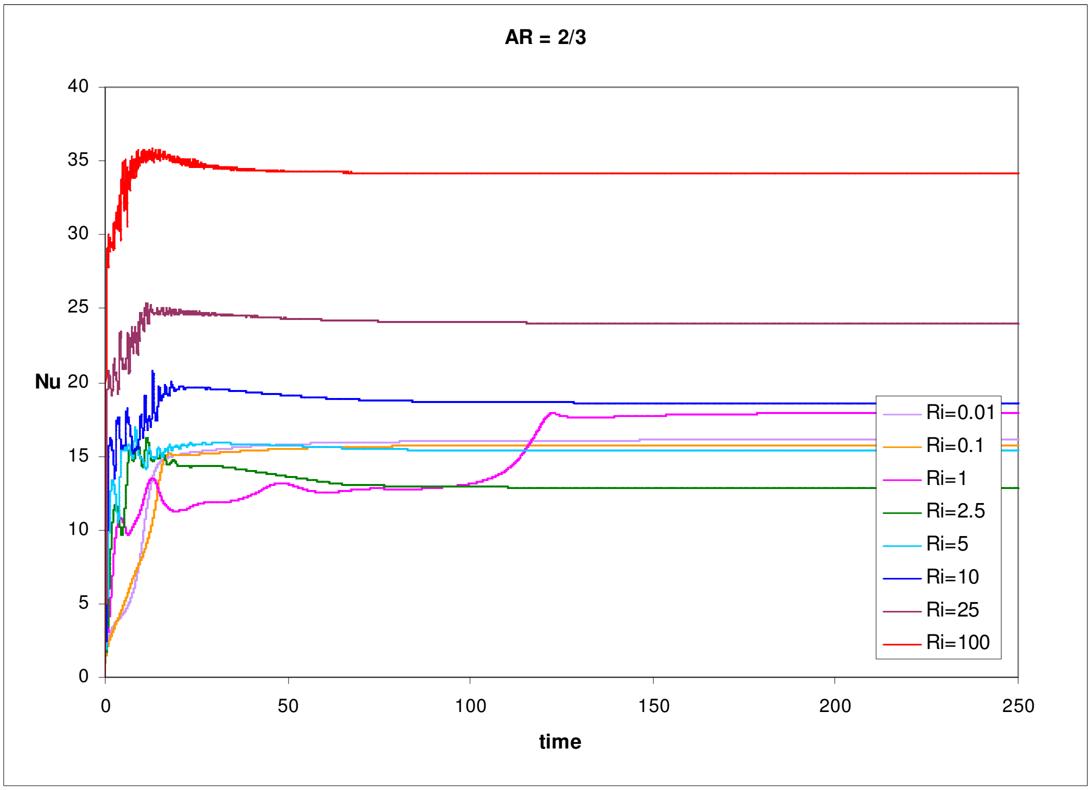


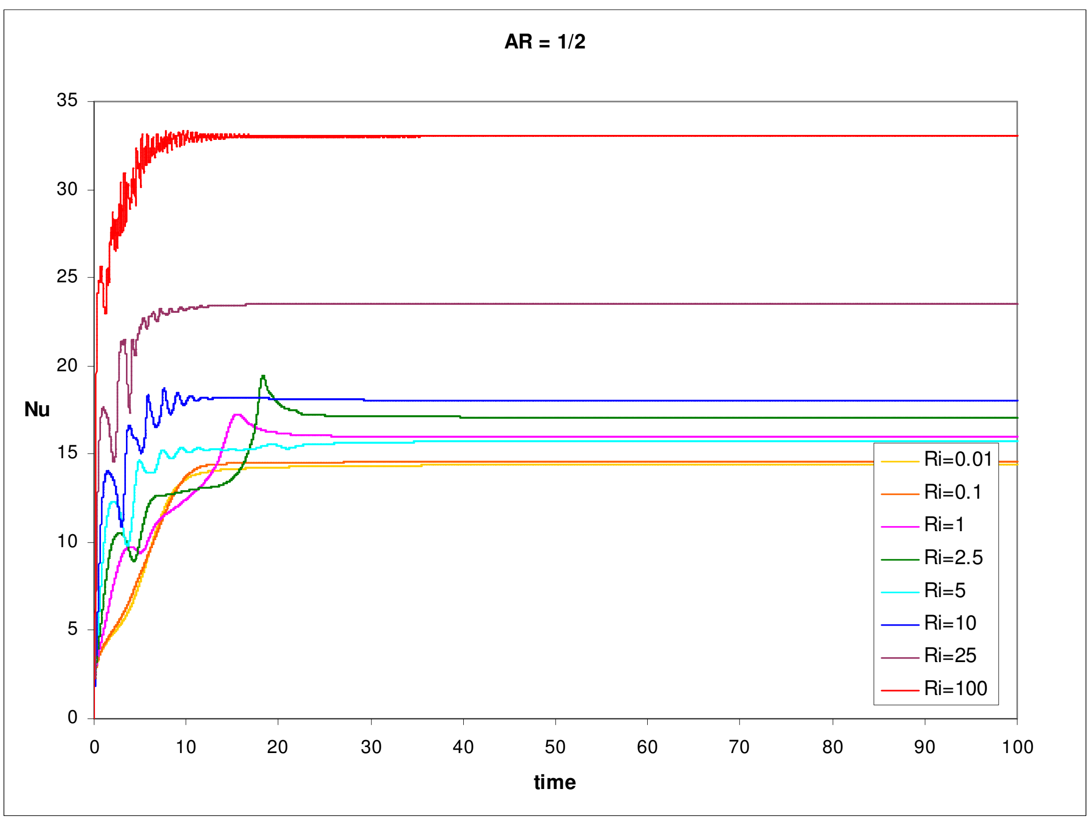


Figure 6.38. Transient variation in average Nusselt number values for various Ri numbers at a point which is located in (0.5,0.375) for Re =800

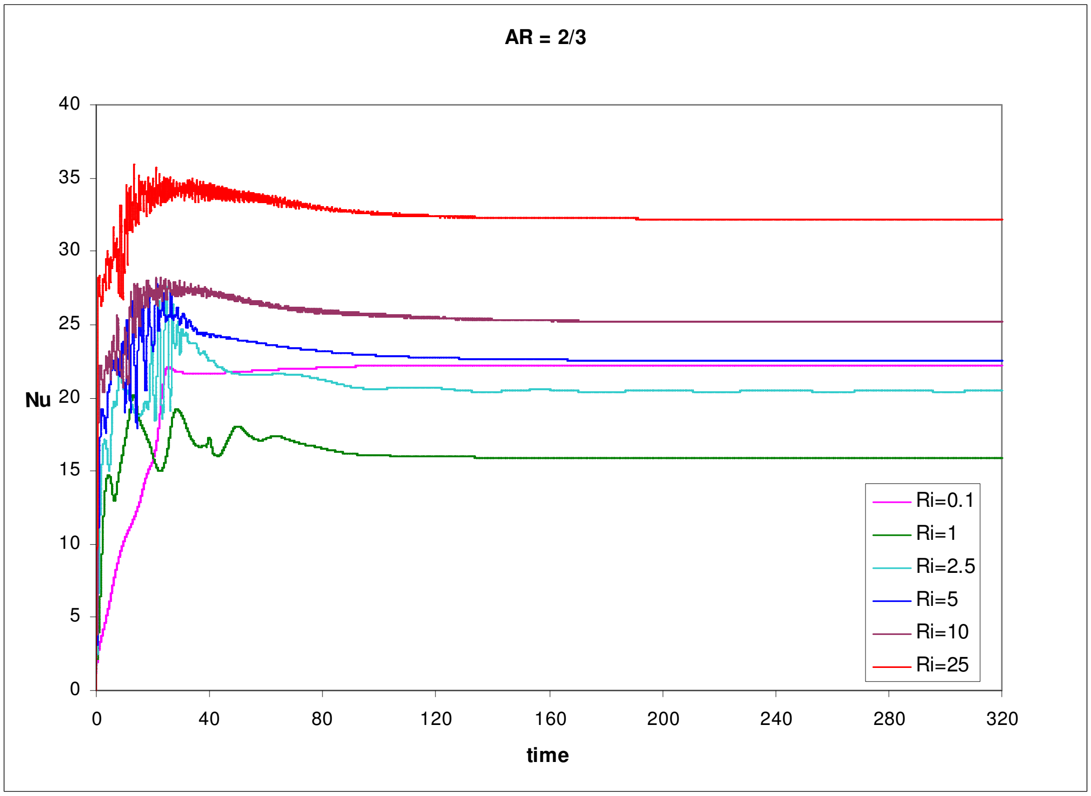


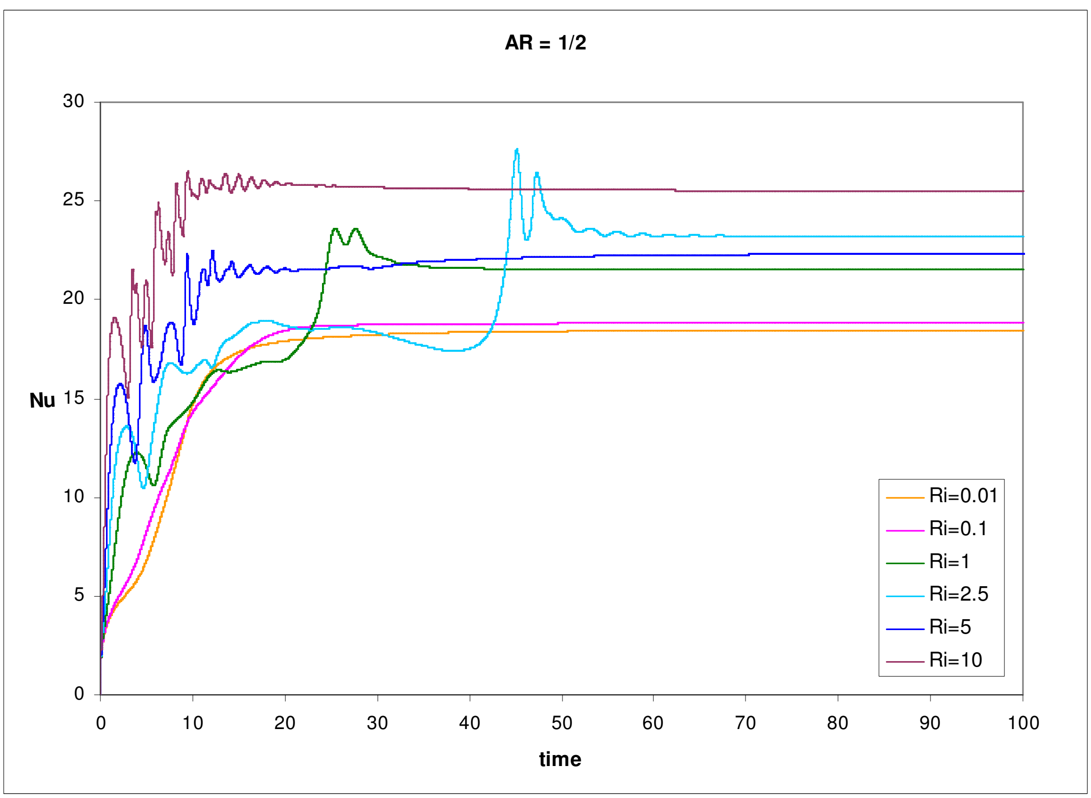


Figure 6.39. Transient variation in average Nusselt number values for various Ri numbers at a point which is located in (0.5,0.375) for Re =1500

# 7. CONCLUSION

Computational study of buoyancy and inertia inside a cavity with a driven lid is performed. In order to include the geometry effect on flow and thermal properties, different aspect ratios are investigated. Non-dimensional, parabolic vorticity-transport and elliptic stream function formulations are adopted along with parabolic energy equation. Body fitted coordinate transformation technique is conducted to generate computational grids. The governing equations are discretized by forward time-centered space finite difference scheme. Adams-Bashforth $3^{rd}$ order method is applied to iterate the unsteady vorticity-transport and energy equations, whereas the successive over relaxation method with Chebyshev acceleration is adopted to solve the Poisson type stream function equation.

The algorithm first is validated by comparing the stream function and temperature values with the results obtained from previous studies and then the new aspect ratios are given along with various control parameters. The test cases reveal that the results obtained by the code written for this study are in close agreement with the results found by Chen and Cheng in their related articles [19], [20].

Wide range of Richardson and Reynolds numbers are selected to investigate the buoyancy and inertia effects. According to the data obtained the shear driven clockwise vortex appears in all of the demonstrated flow conditions but buoyancy related counterclockwise vortex only appears when Richardson number reaches a certain value and this critical value primarily affected by aspect ratio. As aspect ratio gets larger the effect of buoyancy increases while the inertial impact on flow behavior decreases seriously.

Heat transfer performances are studied in terms of Nusselt number and the results are demonstrated in table (6.3). Based on the average and local Nusselt number data any obvious relation can not be stated between the aspect ratio and heat transfer performance. However, based on the average Nusselt number data Chen and Cheng [22] have claimed any reduction in aspect ratio results in an increase in Nusselt number values. Nonetheless, this statement is not applicable for the aspect ratios examined in this thesis.

In inertia dominated flows no buoyancy induced eddy is observed and the vortex core is nearly located at the center of the cavity. However in buoyancy dominated flow conditions primary inertial eddy is not disappeared completely. In 2/3 aspect ratio, inertia induced eddy is pushed to the left corner by the buoyancy formed eddy and occupies a small region there even in high Richardson numbers, yet in 1/2 aspect ratio cavity in buoyancy dominated flows the two eddies are placed symmetrically adjacent to each other in different flow directions but with almost equal strengths.

Second inertia induced eddy is observed in 1/2 aspect ratio cavity in inertia dominated flows at high Reynolds numbers. However in 2/3 aspect ratio no secondary eddy is observed. Furthermore, the size and strength of the secondary inertial eddy strongly depends on the value of Reynolds number.

Resulted shear stress along the moving lid is investigated in terms of friction factor. In cavities with 2/3 aspect ratio an increase in Richardson number results in a decrease in local friction factor in the left side of the lid but leads to a large and extensive increase in the right side. On the other hand, in cavities with 1/2 aspect ratio an increase in Richardson number results in almost anti-symmetric formation of local friction factor and this condition may be attributed to the symmetric feature of the 1/2 aspect ratio cavity flow at high Richardson number values.

# 8. REFERENCES

1. P. Payvar, “Laminar Heat Transfer in the Oil Groove of a Wet Clutch”, International Journal of Heat and Mass Transfer, vol. 34, (1991), p. 1791-1798

2. J. Berger, F. Sadeghi and C. M. Krousgrill, “Finite Element Modeling of Engagement of Rough and Grooved Wet Clutches”, Journal of Tribology , vol. 118, (1996), p. 137-146

3. J. Berger, F. Sadeghi and C. M. Krousgrill, Analytical and Numerical Modeling of Engagement of Rough, Permeable, Grooved Wet Clutches”, Journal of Tribology , vol. 119, (1997), p. 143-148

4. H. Zang, X. Y. Huang, H. S. Li, L. P. Chua, “Flow Patterns and Heat Transfer Enhancement in Low-Reynolds-Rayleigh-number”, Applied Thermal Engineering, vol. 22, (2002), p. 1277-1288

5. A. F. Kothidiwala, B. Norton, P. C. Eames, “the Effect of Variation of Angle of Inclination on the Performance of Low-Concentration-Ratio Compound Parabolic Concentrating Solar Collectors”, Solar Energy, vol. 55, (1995), p. 301-309

6. T. W. Park, S. K. Aggarwal, V. R. Katta, “a Numerical Study of Droplet-Vortex Interactions in an Evaporating Spray”, International Journal of Heat and Mass Transfer, vol. 39, (1996), p. 2205-2217

7. Theodossiou V. M. and A. C. M. Sousa, “an Efficient Algorithm for Solving the Incompressible Fluid Flow Equations”, International Journal for Numerical Methods in Fluids, Computers and Fluids, vol. 9, (1981), p. 163-180.

8. Ghia U., Ghia K. N.,Shin C. T. “High-Re Solutions for Incompressible Flow Using the Navier-Stokes Equations and a Multigrid Method”, Journal of Computational Physics, vol. 48, (1982), p. 387-411.

9. C. Migeon, A. Texier and G. Pineau, “Effects of Lid-Driven Cavity Shape on the Flow Establishment phase”, Journal of Fluids and Structures vol. 14, (2000), p. 469-488.

10. C. Migeon, A. Texier and G. Pineau, “Three-Dimensionality Development Inside Standard Parallelepipedic Lid-Driven Cavities at Re=1000”, Journal of Fluids and Structures (2003) 17, p. 717-738.

11. Khalil M. Khanafer, Abdalla M. Al-Amiri, Ioan Pop, “Numerical Simulation of Unsteady Mixed Convection in a Driven Cavity Using an Externally Excited Sliding Lid”, European Journal of Mechanics B/Fluids 26 (2007) p. 669-687

12. E. Eckert, W. G. Carlston, ”Natural Convection in an Air Layer Enclosed Between Two Vertical Planes with Different Temperatures”, International Journal of Heat and Mass Transfer, vol. 2, (1961), p. 106-120

13. J. W. Elder, “Laminar Free Convection in a Vertical Slot”, Journal of Fluid Mechanics, vol. 23, (1965), p. 77-98

14. A. K. Prasad, J. R. Koseff, “Combined Forced and Natural Convection Heat Transfer in a Deep lid-Driven Cavity Flow”, International Journal of Heat and Fluid Flow, vol. 17, (1996), p. 460-467

15. A. Mohammad, R. Viskanta, “Flow and Thermal Structures in a Lid-Driven Cavity Heated from Below”, Fluid Dynamics Research, vol. 12, (1993), p. 173-184

16. H. Mercan, “Numerical Analysis of Newtonian and Non-Newtonian Lid-Driven Cavity Flow in Plane and Curved Geometries”, 2006

17. Mei Hsia Chang, Chin Hsiang Cheng, ”Predictions of lid-Driven Flow and Heat Convection in an Arc-Shape Cavity”, International Communications in Heat and Mass Transfer, vol. 26, (1999), p. 829-838

18. Chin Lung Chen, chin Hsiang Cheng, “Buoyancy Induced Flow and Convective Heat Transfer in an Inclined Arc-Shape Enclosure”, International Journal of Heat and Fluid Flow, vol. 23, (2002), p. 823-830

19. Chin Lung Chen, chin Hsiang Cheng, “Numerical Prediction of Buoyancy-Induced Periodic Flow Pattern and Heat Transfer in a lid-Driven Arc-Shape Cavity”, Journal of Numerical Heat Transfer, vol. 44, Part A, (2003), p. 645-663

20. Chin Lung Chen, chin Hsiang Cheng, “Experimental and Numerical Study of Mixed Convection and Flow Pattern in a lid-Driven Arc-shape Cavity”, Journal of Heat Mass Transfer, vol. 41, (2004), p. 58-66

21. Chin Lung Chen, chin Hsiang Cheng, “Buoyancy Induced Periodic Flow and Heat Transfer in Lid-Driven Cavities with Different Cross-Sectional Shapes”, International Communications in Heat and Mass Transfer, vol. 32, (2005), p. 483-490

22. Chin Lung Chen, chin Hsiang Cheng, “Numerical Study of Flow and Thermal Behavior of Lid-Driven Flows in Cavities of Small Aspect Ratio”, International Journal for Numerical Methods in fluids, vol. 52, (2006), p. 785-799

23. G. Vahl Davis, G. D. Malinson “the Method of the False Transient for the Solution of Coupled Elliptic Equations”, Journal of Computational Physics, vol.12, (1973), p. 435-461

24. G. Vahl Davis, G. D. Malinson “an Evaluation of Upwind and Central Difference Approximations by a Steady Re-Circulating Flow”, Journal of Computers and Fluids, vol.4, (1976), p. 29-43

25. G. Vahl Davis, “Natural Convection of Air in a Square Cavity”, International Journal for Numerical Methods in Fluids, vol.3, (1983), p. 249-264

26. M. K. Moallemi, K. S. Jang, “Prandtl Number Effects on Laminar Mixed Convection Heat Transfer in a Lid-Driven Cavity”, International Journal of Heat and Mass Transfer, vol. 35, (1992), p. 1881-1892

27. W. J. Luo, R. J. Yang, "Multiple Fluid Flow and Heat Transfer Solutions in a Two-Sided Lid-Driven Cavity", International Journal of Heat and Mass Transfer, vol. 50, (2007), p. 2394-2405

28. W. H. Press, S. A. Teukolsky, W. T. Wetterling, B. P. Flannery, "Numerical Recipes in Fortran", Cambridge University Press, 2nd Edition

29. F. C. Thames, J. F. Thompson, C. W. Mastin, "Numerical Solutions for Viscous and Potential Flow about Arbitrary Two-Dimensional Bodies Using Body-Fitted Coordinate Systems", Journal of Computational Physics, vol. 24, (1977), p. 245-273

30. F. C. Thames, J. F. Thompson, C. W. Mastin, "Automatic Numerical Generation of Body-Fitted Curvilinear Coordinate System for Field Containing Any Number of Arbitrary Two-Dimensional Bodies", Journal of Computational Physics, vol. 15, (1974), p. 299-319

31. D. A. Anderson, J. C. Tannehill, R. H. Pletcher, "Computational Fluid Mechanics and Heat Transfer", Hemisphere Publishing Corporation, (1984)

32. X. Shi, J. M. Khodadadi, "Laminar Fluid Flow and Heat Transfer in a Lid-Driven Cavity Due to a Thin Fin", Journal of Heat Transfer, vol. 124, (2002), p. 1056-1063

33. M. M. Gupta, J. C. Kalita, "a New Paradigm for Solving Navier-Stokes Equations: Streamfunction-Velocity Formulation", Journal of Computational Physics, vol. 207, (2005), p. 52-68

34. E. Leriche, "Direct Numerical Simulation in a Lid-Driven Cubical Cavity at High Reynolds Number by a Chebyshev Spectral Method", Journal of Scientific Computing, vol. 27, (2006), p. 335-345

35. M. Sathiyamoorthy, T. Basak, S. Ror and I. Pop, "Steady Natural Convection Flows in a Square Cavity with Linearly Heated Side Wall(s)", International Journal of Heat and Mass Transfer, vol. 50, (2007), p. 766-775

36. M. A. R. Sharif, “Laminar Mixed Convection in Shallow Inclined Driven Cavities with Hot Moving lid on Top and Cooled from Bottom”, Applied Thermal Engineering, vol. 27, (2007), p. 1036-1042

37. H. Xu, C. Zang, R. Barron, “Numerical Simulation of Cavity Flows based on Transformed Equations”, Applied Mathematics and Computation, vol. 176, (2006), 506-515